8-1-2009

Structure-property relations in porcine brain tissue: strain rate and stress-state dependence

Mark Gregory Tejada Begonia

STRUCTURE-PROPERTY RELATIONS OF PORCINE BRAIN TISSUE:

STRAIN RATE AND STRESS-STATE DEPENDENCE

By

Mark Gregory Tejada Begonia

A Thesis
Submitted to the Faculty of
Mississippi State University
in Partial Fulfillment of the Requirements
for the Degree of Master of Science
in Biomedical Engineering
in the Department of Agricultural and Biological Engineering

Mississippi State, MS

August 2009

STRUCTURE-PROPERTY RELATIONS OF PORCINE BRAIN TISSUE:

STRAIN RATE AND STRESS-STATE DEPENDENCE

By

Mark Gregory Tejada Begonia

Approved:

Steven H. Elder Associate Professor of Agricultural and Biological Engineering (Director of Thesis)	Lakiesha N. Williams Assistant Professor of Agricultural and Biological Engineering (Major Professor)
Jun Liao Assistant Professor of Agricultural and Biological Engineering (Committee Member)	Mark F. Horstemeyer Computational Solid Mechanics Chair of the Center for Advanced Vehicular Systems and Professor of Mechanical Engineering (Committee Member)
Jim Cooley Associate Professor of Pathobiology and Population Medicine of the College of Veterinary Medicine (Committee Member)	Sarah A. Rajala Dean of the Bagley College of Engineering

Name: Mark Begonia

Date of Degree: August 8, 2009

Institution: Mississippi State University

Major Field: Biomedical Engineering

Thesis Director: Dr. Steven H. Elder

Major Professor: Dr. Lakiesha N. Williams

Title of Study: STRUCTURE-PROPERTY RELATIONS OF PORCINE BRAIN TISSUE: STRAIN RATE AND STRESS-STATE DEPENDENCE

Pages in Study: 127

Candidate for Degree of Master of Science

Due to traumatic brain injury (TBI), numerous studies have focused on comprehensively determining the mechanical properties of the brain. This study examined the strain rate dependence of porcine brain under compression, and the microstructural damage was quantified using a confocal microscope and graphical user interface (GUI). The selected strain rates were 0.10 s^{-1}, 0.025 s^{-1}, and 0.00625 s^{-1} while the strain levels targeted for confocal imaging were 15%, 30%, and 40%. This study also characterized the stress-state dependence at a strain rate and strain level of 0.10 s^{-1} and 40%, respectively, under compression, tension, and shear. Strain rate dependency data exhibited viscoelastic behavior, and the analysis parameters correlated with increasing strain rate and strain level. Stress-state dependency data demonstrated distinct nonlinear behavior, and disparities were observed in the analysis parameters between

different testing modes. Finite element procedures can implement this supplementary data for devising more realistic models.

DEDICATION

I want to express my sincere gratitude to all my friends for their endless support and encouragement. I especially want to dedicate this research to my family not only for their unconditional love but for instilling me with the drive and motivation to overcome any challenge. Without my parents and my brother playing such significant roles in my life, I would not have been molded into the individual I am today.

ACKNOWLEDGEMENTS

I want to express my sincere gratitude to all the individuals who have put forth the time and energy in helping me with the completion of this thesis. First, I want to thank my graduate advisor Dr. Lakiesha Williams for her guidance and support while conducting this research. Further appreciation also goes to the other members of the thesis committee, namely, Dr. Jun Liao, Dr. Mark Horstemeyer, Dr. Jim Cooley, and Dr. Steven Elder for their direction and assistance. A debt of gratitude is due to individuals at the Center for Advanced Vehicular Systems, which includes Raj Prabhu for assisting me with the initial stages of the research and Dr. Ricolindo Carino for continually modifying the microstructural analysis GUI. Members of the Electron Microscopy Center should also be recognized for their aid, which includes Amanda Lawrence for performing the required histology and Bill Monroe for assisting me with the confocal imaging. Finally, I want to thank Mr. Wallace Sansing and his associates at Sansing Meat Services for providing me with the tissue specimens necessary for completing my research.

TABLE OF CONTENTS

LIST OF TABLES

LIST OF FIGURES

CHAPTER I

INTRODUCTION

Traumatic Brain Injury

The brain is the control center for the central nervous system (CNS) and is responsible for mediating a vast assortment of structural, homeostatic, and cognitive functions (Widmaier, 2006). Due to an escalating health issue known as traumatic brain injury (TBI), this vital organ has also become the focal point in numerous studies designed to comprehensively determine its mechanical properties. TBI is defined as an acquired neural injury typically caused by an external physical force, resulting in total or partial functional disability or psychosocial impairment (National Dissemination Center for Children with Disabilities (NICHCY), 2006). In general, the leading causes of TBI involve impacts resulting from falls, vehicular accidents, or assaults (Langlois, 2006). For civilians and active military personnel in combat regions, blast damage from improvised explosive devices (IEDs), rocket-propelled grenades (RPGs), and landmines have become the primary source of TBI (Jones, 2007). According to annual statistics from the Centers for Disease Control and Prevention, there are an estimated 50,000 deaths in the United States that directly result from TBI incidents while another 5.3 million Americans must endure long-term disabilities after initially sustaining a TBI (Thurman, 1999). In addition,

at least 1.6 million individuals suffer milder forms of TBI in the form of concussions through sporting and recreational events (Langlois, 2006). Furthermore, this condition can be attributed to an estimated $60 billion in medical costs (Finkelstein, 2006) and could potentially be implicated with neurological deficits such as epilepsy, Alzheimer's, and Parkinson's (National Institute of Neurological Disorders and Stroke, 2006).

Although much of the existing TBI research primarily analyzes the mechanical data collected from various modes of experimentation, other studies have mainly emphasized the resulting chemical implications of this affliction. Investigations from a combination of both biological and engineering perspectives are crucial for understanding the overall extent of TBI and developing varying degrees of prevention. Primary prevention involves the mitigation or evasion of an impact situation altogether (Park, 2008) and is heavily considered in diverse simulations that typically employ finite element analysis (FEA) to achieve more accurate safety assessments. For instance, sled tests have been performed with the HIC Component Testing Device (HCTD) on Hybrid II Anthropomorphic Test Dummies (ATDs), where FEA was utilized for determining if aircraft seats were certified under Federal Aviation Administration (FAA) regulations (DeWeese, 2004). Furthermore, validated finite element human head models were utilized on Hybrid III ATDs fitted with exemplar helmets in order to assess the damage associated with simulated head-to-head field collisions commonly seen in professional football games (Zhang, 2004). While primary prevention aims to minimize the initial physical obstacles resulting TBI impacts, secondary prevention focuses on resolving the biological complications that can exacerbate the onset of injury (Park, 2008).

Organization of the Vertebrate Nervous System

During the development of the vertebrate CNS, the brain divides into four distinct regions known as the cerebrum, diencephalon, brainstem, and cerebellum, as shown in Figure 1.1. The cerebrum and diencephalon combine to form the forebrain while the brainstem is composed of the midbrain, pons, and medulla oblongata. Additionally, the brain contains multiple fluid-filled cavities known as cerebral ventricles.

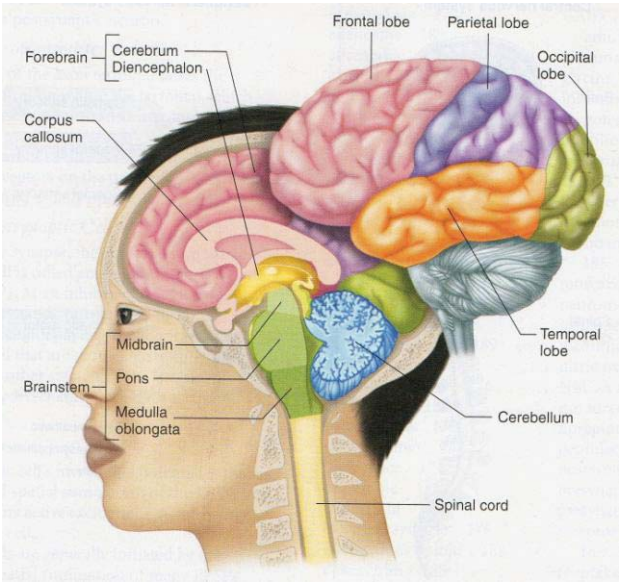

Figure 1.1 Diagram of major brain regions (adapted from Widmaier, 2006).

The cerebrum constitutes the larger, surrounding portion of the forebrain, and despite an estimated 3 mm thickness, its characteristic appearance includes sinuous ridges called gyri that are separated by grooves called sulci. In addition, the cerebrum is separated into cerebral hemispheres that are further divided into three distinct tissue layers. The intermediate layer of tissue usually consists of white matter tracts that are responsible for integrating various regions throughout the cerebrum. Meanwhile, the

innermost and outermost layers of tissue mainly contain gray matter and are known as the subcortical nuclei and cerebral cortex, respectively. Although the cerebral hemispheres are separated by a commissure to an extent, they are still connected by a collection of nerve fibers called the corpus callosum. The cerebral cortex is a crucial integrating component of the CNS and is comprised of four distinct regions: the frontal, parietal, occipital, and temporal lobes. This outer portion of the cerebrum is typically involved in reasoning, learning, memory, perception, and skilled movement generation.

The central portion of the forebrain is the diencephalon, which consists of the thalamus and hypothalamus, and provides nerve fiber connections for other components throughout the CNS. The thalamus serves as a synaptic relay station that processes sensory information transmitted to the cerebral cortex. Its roles include skeletal muscle coordination, focused attention, and general arousal. The hypothalamus is responsible for maintaining internal homeostasis by regulating body temperature, water balance, circadian rhythms, reproductive functions, anterior pituitary functions, and emotional behavior.

The brainstem is the relay center for all neural signals transmitted between the forebrain, spinal cord, and cerebellum. It is composed of a combination of axon bundles and neuron cell bodies that are collectively known as the reticular formation, which is involved in integrating a substantial proportion of neural information in the CNS. Respiratory activity, cardiovascular activity, vomiting, and swallowing are examples of life-sustaining functions that are regulated by the neurons within the brainstem. Other mental responsibilities include reflex orientation and controlled eye movement.

The cerebellum is located behind the brainstem and is involved in coordinating movements associated with balance and posture. For instance, in order to precisely execute the different phases of a certain motor skill, the cerebellum transmits timing signals to the cerebral cortex and spinal cord. This particular region of the brain is also responsible for processing spatial information to allow more appropriate, coordinated motor functions (Widmaier, 2006).

Cellular Organization of the CNS

The vertebrate nervous system is divided into the central nervous system (CNS) and the peripheral nervous system (PNS), which are composed of three distinct variations of neurons. The CNS is composed of the brain and spinal cord and consists of interneurons (association neurons), which are involved in higher neurological functions such as memory and learning. Meanwhile, the PNS consists of two types of neurons: sensory (afferent) neurons and motor (efferent) neurons. Sensory neurons are responsible for transmitting sensory information from receptors to the CNS while motor neurons transfer neural impulses from the CNS to muscles and glands. Motor neurons that initiate skeletal muscle contractions are known as somatic motor neurons while those that regulate cardiac and smooth muscle activity are known as autonomic motor neurons. Autonomic motor neurons can be further categorized as either parasympathetic or sympathetic, which are both responsible for monitoring involuntary functions. Figure 1.2 illustrates the breakdown of the vertebrate nervous system while Figure 1.3 shows the previously mentioned neuron variations.

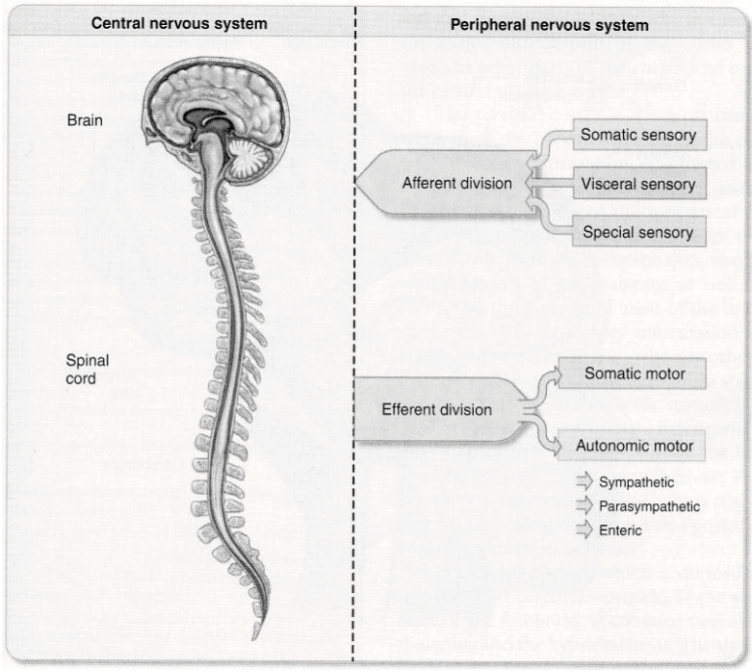

Figure 1.2 Diagram of vertebrate nervous system (adapted from Widmaier, 2006).

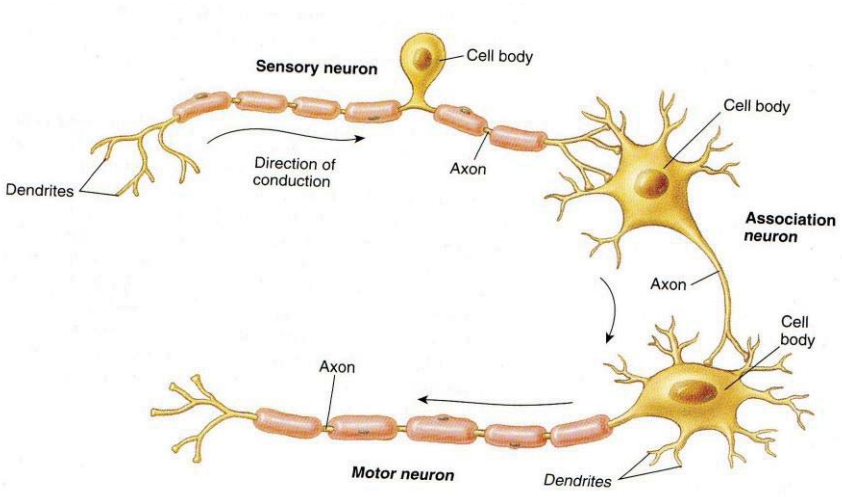

Figure 1.3 Diagram showing different types of neurons (adapted from Raven, 2002).

Despite the relative abundance and variations located throughout the vertebrate nervous system, all neurons possess the structural features shown in Figure 1.4. The cell body is a specific region of the neuron that encases the nucleus. Dendrites are cytoplasmic extensions that branch out from the cell body and increase the surface area available for the receptions of stimuli. Axons are responsible for conducting neural impulses away from the cell body of one neuron to the dendrites of neighboring neurons. Furthermore, most axons are surrounded by a membrane layer known as the myelin sheath, which is divided into 1-2 µm segments separated by gaps called nodes of Ranvier. The role of the myelin sheath is to facilitate quicker conductions of neural impulses. Within the CNS, myelinated axons are referred to as white matter while cell bodies and unmyelinated dendrites are known as gray matter. As for the PNS, myelinated and unmyelinated axons form bundles known as nerves.

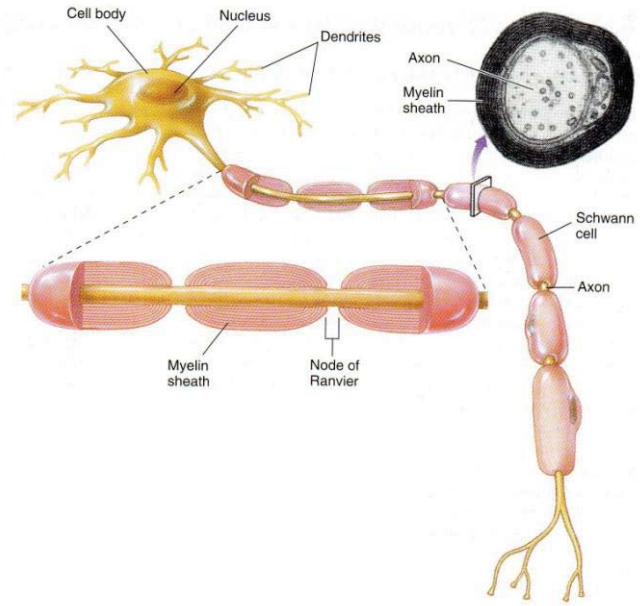

Figure 1.4 Diagram showing common neuron features (adapted from Raven, 2002).

In addition to neurons, the vertebrate nervous system also consists of supportive cells called neuroglia. These types of cells are ten times more abundant than neurons and are responsible for multiple structural and functional roles such as supplying nutrients, removing wastes, directing axon migration, and maintaining immunity. Numerous types of neuroglia are present within the CNS such as astrocytes and oligodendrocytes, which produce myelin within the CNS (Raven, 2002).

Structural Features of the Neuron

In-depth assessment of neuron structural features reveals that both axons and dendrites are comprised of microtubule bundles. In the basic configuration of axons, microtubules are collectively oriented along the same direction with the positively charged end located near the axon terminal and the negatively charged end situated near the cell body. Rather than extending entirely from the cell body to the axon terminal, a vast number of microtubules are aligned parallel to one another in a staggered arrangement. This overlapping structure facilitates the transport of certain proteins to axon terminals, where synapses are formed and maintained. In addition to microtubules, the structural integrity of an axon relies on other cytoskeletal components such as actin filaments and intermediate filaments. Actin filaments reinforce the surrounding membrane while intermediate filaments provide substantial support. Despite the intricate organization of an axon, however, extensive damage to any of its constituents could disrupt the entire structure and eventually lead to axonal degeneration. Additionally, dendrites also consist of microtubules, but their polarities

are mixed. Some might be positively charged at the axon terminal while others might be negatively charged (Alberts, 2008).

CHAPTER II

LITERATURE REVIEW

Preliminary Head Injury Research

Numerous controlled head injury experiments have incorporated an assortment of testing protocols to anesthetized animals, human cadavers, and surrogate materials. These subsequent test models have been exposed to direct impacts caused by free-falling or projectile motions as well as indirect impacts created from torsional forces transmitted through the neck into the head. Earlier investigations on the biomechanics of head injury detailed various concepts including the changes in volume and intracranial pressure, the deformations within corresponding cerebral constituents, and the mechanical implications resulting from cranial trauma. Although the research scope and experimental conditions vary considerably within the current literature, much of the work offers valuable insight regarding cranial injury biomechanics.

Direct Impact Studies on Primates

In contrast to other experimental approaches, animal models provide sufficient means for analyzing the biomechanical behavior from cranial impacts. Although multiple species have been selected for corresponding investigations, the ideal surrogates for human applications are primates due to the comparative geometry of

their neural structures, as seen in Table 2.1 (Gurdjian, 1965; Ommaya, 1966). Moreover, rhesus monkeys are prime candidates for experimentation due to their brain-mass ratios of 1:5, which are similar to humans (Ommaya, 1971). Despite the physiological similarities, however, the use of primates for head injury research gradually declined into the late 1980s due to ethical concerns from the general public, leading to the utilization of alternative test specimens.

Table 2.1 Primates used in head injury research (adapted from McElhaney, 1971).

Genus	Species	Common name	Brain mass (g)	Body mass (kg)
Saimiri	sciureus	squirrel	20–27*	0.8–1.0**
Macaca	arctoides	bear, stumptail		
	fascicularis	cynomolgus, crab-eating, long-tailed		3.1–4.9**
	fuscata	Japanese		
	mulatta	rhesus	70–100*	3.0–5.0*
	nemestrina	pig-tailed		6.4–10.2**
Papio	cynocephalus	Savannah baboon		12.4–22.8**
Pan		chimpanzee	350–500*	47–60**

*Ommaya and Hirsch[19]
**Jungers[206]

In the 1960s, numerous studies were conducted on varying species of primates as shown in Figure 2.1. The descriptions of these experiments can be categorized according to testing parameters where forces were either directly transmitted to the cranium by using a customized striker device or indirectly applied to another region of the body using a sled. Studies involving direct impact can be further broken down into experiments that either permitted free motion immediately following contact or delivered a predetermined cranial impulse.

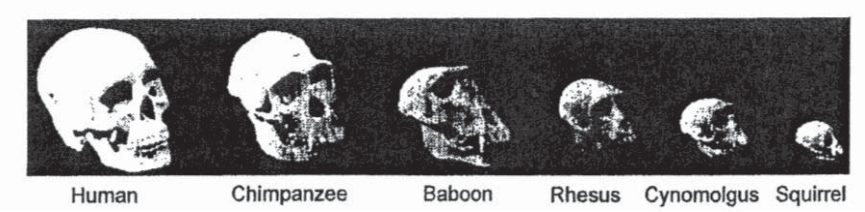

Figure 2.1 Skull geometries for primates used in head injury research (adapted from McElhaney, 1971).

Preliminary studies focusing primarily on direct, unconstrained impact were performed by Ommaya and fellow researchers (Goldsmith, 2001) and incorporated the findings of Holbourn, who emphasized shear strain as a significant mechanism leading to cerebral trauma (Holbourn, 1945). Initial research from Ommaya and colleagues involved occipital and temporal impact tests in which multiple rhesus monkeys were stabilized with a swing and subjected to a piston with loading velocities ranging between 4.1 and 15.9 m/s. To obtain a higher threshold of cerebral trauma, researchers also fitted test subjects with cervical collars. While linear accelerations of 700-800 G consistently produced concussions in rhesus monkeys without collars, accelerations ranging up to 1000 G were seen in test subjects provided with collars and occasionally resulted in concussions (Ommaya, 1964). Furthermore, it was determined that in comparable impact scenarios, the animals fitted with cervical collars experienced higher translational accelerations than those without collars, suggesting that rotational motion provided a key role in basic head injury mechanisms (Hirsch, 1970).

In a subsequent investigation that primarily focused on assessing visible brain injuries, an explosive powder gun was utilized to propel a 0.5 kg piston for occipital and

frontal impact tests on nearly 70 adult rhesus monkeys. Test subjects chosen for frontal impact experiments, however, were fitted with protective cranial plates to minimize potential skull fractures, and although their torsos were secured, their heads were still free to rotate. The results indicated that the occurrence and distribution of coup and contrecoup injuries highly correlated with both loading direction and onset of skull fracture. On the other hand, the results also revealed that subdural hematoma (SDH) had relatively similar incidence in both frontal and occipital loading directions and was typically seen in the anterior regions of the brain regardless of the precise impact location. Furthermore, there was no correlation between the skull fracture and SDH in the frontal impact testing data, but the occipital impact testing results showed that a higher percentage of rhesus monkeys experienced a combination of SDH and skull fracture. It was also evident from the study that in addition to rotational motion, skull deformation provided a considerable contribution to the production of brain injury (Ommaya, 1971).

Ommaya and colleagues extended their research regarding direct cranial impact by performing similar experiments on chimpanzees and squirrel monkeys. Based on these studies, it was determined that the smaller test subjects required more severe loading conditions to elicit concussions, and the injury threshold was characterized by angular velocities ranging from 60 to 200 rad/s and accelerations ranging from 5 to 50 krad/s^2. In addition, impact levels necessary for producing concussions in chimpanzees was higher than anticipated presumably due to the considerable neck musculature and thicker occipital skull. These findings were later confirmed when load-distributing caps

were applied to test specimens. In a related investigation, this research team analyzed the skull-brain relative motion in rhesus monkeys fitted with plastic calvarium components by utilizing a high-speed camera with 3000-9000 fps to measure brain displacement in relation to an embedded screw. It was determined that the observed frequencies exhibited a potential connection between the bulk motion of the brain and surface disturbances from the impact site as well as a translational wave (Hirsch, 1970).

While Ommaya's group performed studies for assessing head injury biomechanics in primates, Wayne State University researchers initiated similar experimentation after shifting from canine test subjects to primates instead (Gurdjian, 1965). In one study involving 12 stump-tail monkeys with their heads unrestricted but their torsos intact, a 1 kg piston was utilized for occipital impact testing with corresponding velocities from 10.7 to 15.9 m/s. Furthermore, each animal was sacrificed one week following the experiments to facilitate extraction of both the brain and cervical portion of the spinal cord for histological analysis. The subsequent data exhibited minimal to severe concussive damage in addition to skull fracture in 8 cases, but no correlation could be derived between concussion and fracture as well as between maximum impulse and either concussion or fracture. Histological results also confirmed neuronal damage in varying brain regions but revealed that damaged cells primarily resided in the brainstem instead of the cortex. Based on these findings, Wayne State University researchers suggested that the principal mechanism in concussive injuries involved shear strain in the brainstem caused by translational acceleration. This conclusion differed from the proposition made by Ommaya and

colleagues that the primary injury mechanism was the result of deformations within the cortex created from rotational motions (Hodgson, 1969).

In a less extensive investigation focusing on concussions in primates, electroencephalogram (EEG) recordings were utilized on 15 unrestricted pig-tailed monkeys for occipital impact experiments in which a padded striker of 1.25 or 6.35 kg maintained loading velocities between 7.5 and 37 m/s. Although the severity of observed concussions varied, a correlation was still generated between the measured accelerations and the injury level. The researchers also distinguished two separate concussion phases: initial stiffening leading to a convulsive state characterized by intermittent twitching followed by an extended motionless paralytic state (Douglass, 1968).

In spite of numerous experiments specifically focusing on occipital impact experiments, other studies shifted the emphasis to lateral cranial impacts. In studies involving squirrel monkeys, macaques, and chimpanzees, McElhaney and associates applied cranial forces utilizing a flat, pneumatically-propelled 10 kg impactor that was either padded or unpadded depending on the specified testing parameters. The average accelerations were between 200 and 1500 G, but due to the impactor geometry and surface area, the resulting injuries varied from 1 to 5 according to the predetermined scaling system (McElhaney, 1971). As a result, additional experiments were performed with reinforced padding to determine the effects of longer impulse duration, and it was established that contrecoup hemorrhages were subsequently less prevalent in these tests in comparison to the experiments with a shorter duration.

However, other injuries were seen in the longer sustained tests, which included internal cerebral hemorrhaging within the basal ganglia, hemorrhaging near the medullary region and brain stem, and subdural bleeding. McElhaney's group eventually used dimensional analysis to establish level 3 cranial injuries in humans for conditions with a duration, linear acceleration, impact force, and velocity of 7.5 ms, 56 G, 3.6 kN, and 6.7 m/s, respectively (Stalnaker, 1973).

In another study primarily focusing on cranial loads applied in alternative directions, Shatsky's group conducted temporoparietal impact tests on rhesus monkeys that were perfused with a biological fluid, restrained in a sled, and subsequently propelled into a stationary impact at velocities between 3 and 8 m/s. The resulting cinematography showed that during lateral cranial impacts, the middle cerebral artery shifted away from the point of contact while the anterior cerebral artery shifted toward the point of contact, suggesting that brain shear occurred due to skull deformations. Furthermore, when compared to previous occipital impact data, the temporoparietal data indicated that loading from the lateral direction resulted in lower accelerations, longer acceleration rise times, and longer durations potentially affected by a combination of the temporalis muscle as well as flexibility within the temporoparietal section of the skull (Shatsky, 1974).

Although Ono and associates initially concentrated on head injury biomechanics stemming from both frontal and occipital loading conditions, they eventually expanded their work by including similar investigations along the temporal region. Utilizing a stroke-limited, 13 kg impactor, researchers applied temporal impact tests on 23

macaques at velocities between 10 and 27 m/s. The resulting data showed varying degrees of neuronal injury in 18 of the 23 macaques, and nearly 25 percent suffered skull fractures. In addition, the experimental data was compared to the results of prior studies, and it was determined that the concussion threshold from lateral impacts was higher than impacts through the sagittal plane (Ono, 1982).

To further expand on prior head injury analysis limited to occipital and frontal impact forces, Hodgson and colleagues subsequently performed a series of experiments aimed at evaluating the relative effects of varying loading directions. Using a pneumatically-propelled, rubber-tipped 1.1 kg striker, researchers applied frontal, temporoparietal, occipital, and cranial vertex impacts at a velocity of 20 m/s on multiple stump-tail monkeys fitted with protective fiberglass caps to minimize skull fractures. All 4 loading conditions were randomly employed on test subjects over a span of 2 months, and there were no perceived cumulative neurological complications. Furthermore, it was determined that in cases involving lateral impact forces, the primates experienced phases of unconsciousness lasting up to 5 times longer than those measured in remaining 3 loading directions (Hodgson, 1983).

Indirect Impact Studies on Primates

Despite numerous studies primarily involving direct impact situations, other investigations such as the collaborative work by Ommaya, Gennarelli, and Thibault provided further examinations into the biomechanics of indirect cranial injuries. Their joint research utilized a customized flywheel linkage device to produce either pure

translation or 45° rotation in squirrel monkeys to evaluate the relative influence of the rotational and translational motions associated with indirect loads through the sagittal plane. In the translational cases, the observed accelerations ranged from 665 to 1230 G, but none of the 12 primates could be concussed. On the other hand, the rotational cases exhibited lower accelerations between 348 and 1025 G, and all 13 primates suffered concussions. In addition, the results from the rotational experiments generally exhibited more frequent and more severe visible brain lesions (Gennarelli, 1972).

Gennarelli and Thibault consequently performed more comprehensive impact tests on 40 rhesus monkeys by using a modified version of their linkage system, which was enhanced with a pneumatic cylinder attached to a helmet. The newly designed device was capable of generating an accelerative sequence in the posterior-anterior direction over a 60° arc through the sagittal plane and also possessed a capacity for varying loading parameters such as the amplitude, duration, and distance between the centers of mass and rotation, respectively. In contrast to previous studies in which angular accelerations were perceived to be the dominant factor in cranial injuries, the resulting experimental data confirmed that both the concussion threshold and onset of acute SDH were strongly associated with tangential accelerations, especially between 500 and 700 G. Contrary to Holbourn's findings, which isolated rotational motion as the primary head injury mechanism, this research instead suggested that injury severity correlated with maximum translational as well as rotational acceleration (Abel, 1978). By focusing on the deceleration phase from previous experimental results obtained with the identical testing device, Gennarelli and Thibault were able to specifically examine

the emergence of acute SDH in rhesus monkeys subjected to head injury assessments. The results indicated that SDH could not be generated for scenarios in which the peak acceleration of nearly 100 krad/s^2 was held constant while the impulse duration was extended. Moreover, it was determined that sufficient increases in impulse duration also contributed to the incidence of diffuse axonal injury (DAI) (Thibault, 1990).

In additional studies involving 45 baboons and rhesus monkeys, Thibault, Gennarelli, and colleagues completed impact tests using the previously mentioned second generation linkage system in order to provide supplementary evaluations on biomechanics relevant to both concussion and DAI. The testing device was capable of producing controlled impulses ranging from 100 to 200 krad/s^2 in the sagittal, coronal, and oblique planes. According to the data, it was confirmed that the extent of neural impairments, DAI, and comas were directly proportional to the loading applied in the coronal direction. Furthermore, the coronal configuration generated the highest degree of cranial trauma while the sagittal configuration produced the least severe (Gennarelli, 1982). These results eventually prompted the authors to conduct further research on 39 baboons and rhesus monkeys using a third generation linkage system, which was designed to produce rotational accelerations between 70 and 180 krad/s^2 in relation to the sagittal, axial, and coronal planes. Aside from expected analysis relating injury severity to higher maximum accelerations, other notable aspects of this study revealed a substantial variation in axonal damage with regard to loading direction. Sagittal impulses produced axonal damage limited to the white matter regions within the cerebral hemispheres or failed to generate any damage at all. Meanwhile,

horizontal impulses resulted in axonal trauma that propagated through the central brain divisions including the corpus callosum while coronal impulses led to severe axonal injury that ultimately extended into the brainstem. It was eventually determined that the distinct variations in the results were attributed to the combined geometries of both the brain and skull (Gennarelli, 1987).

Ono's team further expanded on their prior lateral impact testing on primates by performing additional sagittal impact experiments to produce either pure translation or 45 - 60° rotation about the C6 - C7 neck vertebrae in primates, which had their heads restricted and fitted with shock-absorbing helmets. The experiments focusing primarily on translational motion were conducted on 26 primates that were thrust down a track into a barrier, generating helmet velocities from 22 to 28 m/s and average resultant head accelerations from 240 to 1100 G. In addition, the entire experimental group sustained concussions and experienced negative intracranial pressures near 101 kPa. For the 18 tests emphasizing rotational motion, the cranial impacts occurred in the parietal section, producing tangential velocities from 12 to 28 m/s and resultant average rotational head accelerations from 52 to 290 krad/s^2. The resulting data revealed a potential correlation between average linear acceleration and the onset of contusions as well as skull fractures. A comparison of the designated testing modes demonstrated that coup and contrecoup were more evident in the rotational experiments rather than the translational, and it was also determined that concussions were more severe in the pure translational cases. Combing their comprehensive head trauma data with dimensional parameters from prior work by both McElhaney and Stalnaker, Ono's team

eventually proposed a revised concussion threshold for humans. As shown in Figure 2.2, this hyperbolic curve was called the JARI Human Head Impact Tolerance Curve and was graphically similar to the Wayne State Tolerance Curve (Ono, 1980).

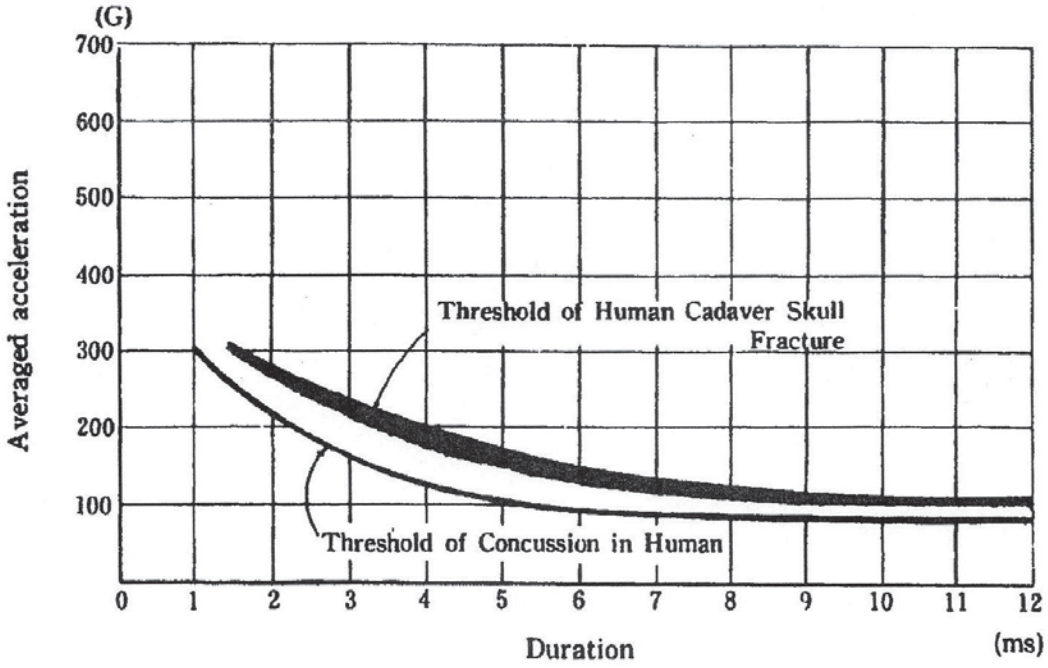

Figure 2.2 JARI human head impact tolerance curve (adapted from Ono, 1980).

In an extensive series of impact studies utilizing not only primates, but also human volunteers and anthropomorphic dummies, numerous sled tests were performed on 3 different tracks located at the Muroc Air Force base in the Mojave Desert; the Holloman Air Force base in Almagordo, New Mexico; and the Naval Biodynamics Laboratory in Michoud Station, New Orleans. One series of sled tests involved 88 chimpanzees that were restricted to a headfirst supine position while being accelerated at 123 G, but autopsy results attributed their deaths to their sustained

internal injuries rather than brain damage. On the other hand, the chimps tested at the Almagordo track consistently suffered neurological deficits after experiencing maximum sled accelerations between 67 and 89 G. Despite its contribution to head injury biomechanics research, however, this work also signified the eventual shift from utilizing primates (Stapp, 1983).

Impact Studies on Human Cadavers

In 1939, studies focusing on the head injury biomechanics in human cadavers were initiated, subsequently leading to the generation of the Wayne State Tolerance Curve (WSTC), a fundamental component of the eventual Head Injury Criterion (HIC). These initial experiments utilized embalmed cadavers that were fitted with accelerometers and pressure transducers before being systematically dropped onto steel blocks in order to recreate frontal impacts. The heights of release were steadily increased until linear skull fractures were detected, which were perceived to be concussion indicators. Based on the resulting data, 80% of tests yielded concussive injuries with maximum accelerations occurring at 456 G, 370 G, and 237 G for impact durations lasting 1, 2, and 6 ms, respectively. In supplementary impact experiments involving isolated cadaver heads, contributions from the additional body mass expectedly resulted in lower accelerations and longer pulse durations (Hodgson, 1972).

Earlier biomechanical research performed at Wayne State University eventually shifted towards using intact human cadaver heads for frontal, occipital, and parietal impact testing. In one series of experiments in which cadaver heads were released from

varying heights onto steel slabs, the resulting energy levels and impact velocities were from 45 to 102 J and from 4.1 to 7.0 m/s, respectively. Investigators eventually discovered that the difference in loads applied to produce cranial fractures was not substantial in comparison to the existing overall variation in loading. The results also revealed that the minimum energies required to generate single fractures was only slightly lower than energies necessary for stellate fractures (Gurdjian, 1949).

A more extensive series of cadaver impact tests were performed by Hodgson and Thomas to fully evaluate the different head injury criteria already proposed in literature. In addition to level surfaces, hemispherical and cylindrical surfaces were employed for this set of experiments in which strain gauges were attached to the impact surfaces while the resultant accelerations were measured by biaxial accelerometers mounted on the sides of each head. The impact test data corresponding to flat surfaces demonstrated that linear fractures were attributed to maximum accelerations from 190 to 370 G, which were similar to predictions from the WSTC. The overall data set also revealed that the average maximum loads required to induce fracture was proportional to the impact surface curvature but inversely proportional to the contact area (Hodgson, 1971).

Instead of using embalmed cadavers, McElhaney's team performed frontal and temporal impact experiments on fresh, human cadavers using both padded and unpadded metal disks. Although both impact devices were 10 kg and 100 mm in diameter, the padded striker achieved velocities from 10.7 to 11.6 m/s while the unpadded striker only maintained velocities between 3 and 4 m/s. The heads of the

cadavers were also supported upright by surgical threading, which was designed for quick tearing after initial contact, and tests were postponed until any visible rigor mortis had subsided. While temporal impact data produced peak loading and acceleration ranges from 4.5 to 8.9 kN and 130 to 200 G, respectively, the frontal impact data yielded higher peak loading and acceleration ranges from 8.0 to 10.7 kN and 180 to 250 G, respectively. However, temporal cases illustrated higher impulse durations from 4.0 to 5.5 ms when compared to frontal cases with impulse durations only from 3 to 4 ms. Furthermore, supplementary quasi-static experiments on cadaver heads exhibited a higher stiffness in the anterior-posterior direction than in the lateral direction, which corresponded to respective values from 1.4 to 3.5 kN/mm and 0.7 to 1.8 kN/mm (McElhaney, 1973).

Similar head injury analysis was performed by Advani and colleagues in which seated human cadavers were exposed to multiple frontal, occipital, and temporal impacts. Flat strikers with masses ranging from 9.1 to 22.6 kg were utilized for initiating contact at velocities between 1.3 and 7.5 m/s. Since higher applied loads did not always correlate with higher impact velocities, it was determined that undetected cranial fractures from prior tests were possible factors that contributed to the observed trend. The resulting data also revealed that the lowest applied loads for generating skull fractures were 6.2, 12.5, and 4.5 kN for frontal, occipital, and temporal experiments, respectively, which were all substantially lower than cranial fracture values reported by McElhaney (Advani, 1975).

In an attempt to scale cranial impact tolerances from prior testing with primates, Ono and associates utilized human cadaver skulls that were filled with gelatin, coated with plaster along the outer surface, and fitted with Hybrid II anthropomorphic skin. The reconstructed skulls were systematically dropped from different heights onto rubber blocks until fractures were generated in the frontal and occipital regions. Upon analysis of the graphical data for both frontal and occipital impacts, skull fractures were deemed to occur at average accelerations of nearly 300 G for pulse durations of 1.5 ms. In addition, the tolerance scaling towards human applications resulted in a fracture limit that was higher than the original estimates based on previous concussion thresholds (Ono, 1980).

Brain Injury Investigations in Human Cadavers

Stalnaker's team initiated impact studies that primarily focused on brain injury in human cadavers and consequently eliminated the incidence of skull fractures from experimental considerations. These preliminary temporal impact tests utilized padded strikers composed of varying materials to reach velocities ranging between 5.8 and 13.4 m/s. To facilitate the pathological analysis following contact, researchers pressurized the vascular system of each cadaver with a histological stain in an attempt to identify potential sites of hemorrhaging. As seen in Figure 2.3, the resulting data exhibited linear accelerations from 48 to 206 G with maximum applied forces from 1.4 to 10.0 kN and were accompanied by angular velocities and accelerations from 43 to 71 rad/s and from 4.1 to 21.0 krad/s^2, respectively. Although the staining procedure was mainly

sensitive to injury cases involving loads and accelerations higher than 6.7 kN and 140 G, one cadaver evidently sustained contrecoup vascular damage while another suffered from cerebral hemorrhaging. In addition, none of the human cadavers selected for the temporal impact testing had encountered skull fractures (McElhaney, 1973).

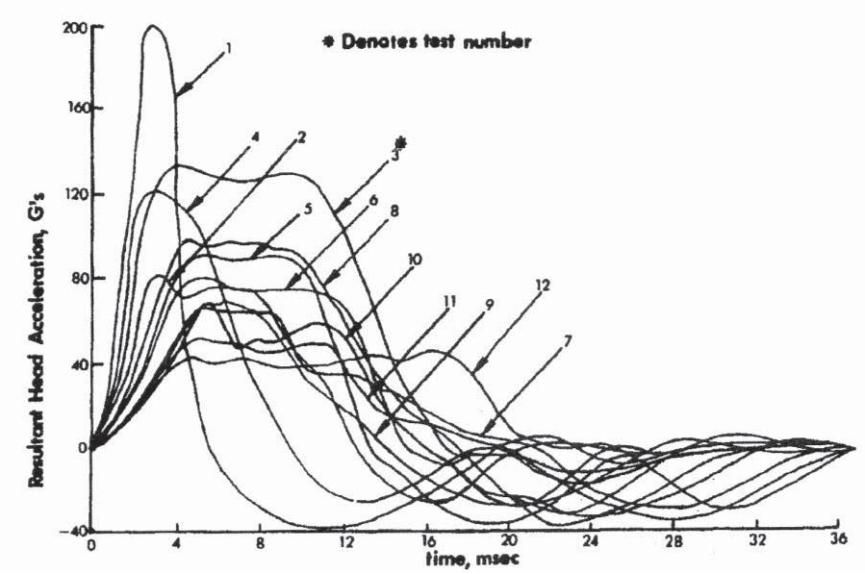

Figure 2.3 Plots of resultant head acceleration (G) versus time (ms) generated from preliminary cadaver studies for assessing brain injury (adapted from McElhaney, 1973).

Nahum and Smith conducted a similar impact analysis on seated human cadavers in which india-ink-formalin-saline solution was used to pressurize the cerebral vasculature, thereby filling the cerebrospinal fluid (CSF) space with a comparable fluid. The physiological solution was intended for simulating normal biological conditions and for detecting any leakage following each experiment. The frontal impact tests involved 5.3 kg, padded impactors that were propelled at velocities between 3.6 and 9.6 m/s into stationary cadaver heads that were initially inclined 45° forward into the sagittal plane.

According to the data, the minimum conditions required for generating damage were distinguished by a peak impact force of 7.7 kN and peak head acceleration of 195 G, and it was also determined that the observed injuries were representative of damage seen in clinical scenarios. Despite initial associations identified between injury severity and both the Gadd Severity Index (GSI) and HIC, additional data points were still required to properly establish a clearer correlation between the parameters (Nahum, 1976).

Nahum and colleagues initiated further investigations comparable to their prior work involving frontal impacts but performed 2 series of temporal impact experiments instead. While the first series utilized a single cadaver that was exposed to 4 separate insults, the second series involved 5 cadavers that were each subjected to a single insult. The second series also employed a 4.17 kg striker that generated contact velocities from 8.1 to 10.2 m/s, which resulted in peak head accelerations from 326 to 703 G. As with previous results from frontal impact experiments, the temporal impact data exhibited a proportional relation between the measured head accelerations and pressure gradients. In addition, subarachnoid hemorrhage was observed and both coup and contrecoup sites (Nahum, 1980).

In order to recreate frontal, temporoparietal, and front-facial impacts, Got's team subjected non-embalmed human cadavers to free-fall tests at heights between 1.8 and 3 m. Cadaver heads were connected to accelerometers and perfused with a dye solution that was intended to facilitate the detection of any ruptures within the vasculature. Based on the experimental data pertaining to tests performed at a height of 3 m, most of the damage was localized in the brainstem. It was also determined that

the probability of minimal injury occurred when the HIC level was lower than 1500, which contrasted with Nahum's findings stating that severe injuries occurred at an HIC level slightly under 660 (Got, 1978).

In conjunction with prior work at the University of Michigan Transportation Research Institute, Nusholtz and associates performed frontal impact experiments on repressurized human cadavers at velocities between 3.6 and 5.7 m/s. 150 mm diameter impactors of either 25 or 65 kg were applied three times to five test subjects and two times to the remaining four test subjects. Epidural pressures reached maximum levels of 180 kPa within the frontal regions of cadaver skulls and minimum levels down to -62 kPa at the occipital regions. According to autopsy results, subarachnoid hemorrhage was the most prevalent injury sustained and typically found in the parietal and frontal skull sections. While the resultant linear and angular accelerations proved to be the most predictable measures, other experimental parameters did not fully correlate with injury extent. Injuries were only produced at impacts higher than either 161 G or 7.2 krad/s^2, and the only test subject that suffered contrecoup damage had also experienced the highest linear acceleration, angular acceleration, and rotational velocity. Correlation analysis on the results also revealed that post-mortem time and repressurization generated variations comparable to deviations attributed to biological variability. The experimental data was also deemed insufficient for redefining human tolerance thresholds since multiple impacts were applied, thereby enhancing the potential for cumulative brain damage (Nusholtz, 1984).

Impact Studies on Human Volunteers

Renowned for his pioneering impact studies involving human volunteers, Colonel John Stapp comprehensively investigated the associated tolerance levels for long duration impulses. Stapp utilized over 70 human volunteers to initiate a series of sled deceleration tests in a Daisy Track while meticulously collecting the physiological and kinematic data. Experimental results revealed that peak sled accelerations of 39 G and onset rates of 315 G/s endured for 280 ms could be reasonably tolerated, but for a higher onset rate of 1.37 kG/s at an identical peak acceleration and lower duration, temporary loss of consciousness was evident. The most severe loading conditions involved maximum sled accelerations up to 45.4 G for durations from 160 to 360 s, and it was determined that the most significant experimental parameter affecting tolerance levels was the onset rate. Cranial accelerations were neither measured nor correlated with trauma, Stapp's protocols were still duplicated in numerous impact experiments devised for an assortment of test subjects including primates, cadavers, and volunteers (Stapp, 1971)

Ewing and colleagues collected similar data from sled tests conducted primarily in the Naval BioDynamics Laboratory at Michaud Station in New Orleans. Volunteers were subjected to progressively severe impacts at 1 G increments from 3 to 8 G for an onset rate of 500 G/s or 3 to 10 G for an onset rate of 250 G/s. High-speed cameras were also mounted to frontal and lateral sled positions, and biaxial accelerations were measured at the T1 vertebra, mouth, and top of the head while angular velocities were measured only at the T1 vertebra and mouth. The peak acceleration and angular

velocity observed for all cases was 47.8 G and 30 rad/s, respectively, and the acceleration translated from the sled to the mouth intensified considerably. Although testing data exhibited remarkably consistent behavior in all volunteers, no correlation was evident between sitting height and angular velocity (Ewing, 1968). As predicted earlier, increases in maximum sled acceleration and duration were linked to more severe angular accelerations, angular velocities, and linear accelerations in the head along with linear accelerations in the T1 vertebra (Ewing, 1976).

Research teams led by Clarke and Gragg performed comparable sled tests from 7.7 to 10.3 G on human volunteers restricted by a combination of safety devices that included lap-belts, Air Force shoulder harnesses, and air bags. Cases involving only lap-belts led to peak average angular accelerations, average angular velocities, and linear accelerations of 1.6 krad/s^2, 35 rad/s, and 22 G, respectively. In addition, the resulting head-sled acceleration ratio was nearly 2.5 and similar to the ratio observed in prior cadaver studies. For cases with both lap-belts and air bags, volunteers experienced mild or moderate headaches lasting up to 24 hours, which were attributed to hyperextension since the symptoms were not seen in other testing scenarios (Clarke, 1971).

Recent Porcine and Human Brain Research

With stricter protocols for procuring brains from both humans and primates in recent years, alternate species have proven to be viable surrogates for investigating neural mechanical properties.

Rationale for Porcine Brain as a Suitable Surrogate

Despite the extensive data collected from various impact experiments on primates and cadavers, human volunteers remain the ideal candidates for realistic head trauma simulations due to inherent physiological similarities. However, the loading threshold required for human test subjects would inevitably be restricted in order to limit the injury extent. In order to circumvent ethical dilemmas with utilizing both primates and humans, researchers have recently shifted towards using porcine specimens as seen in Figure 2.4.

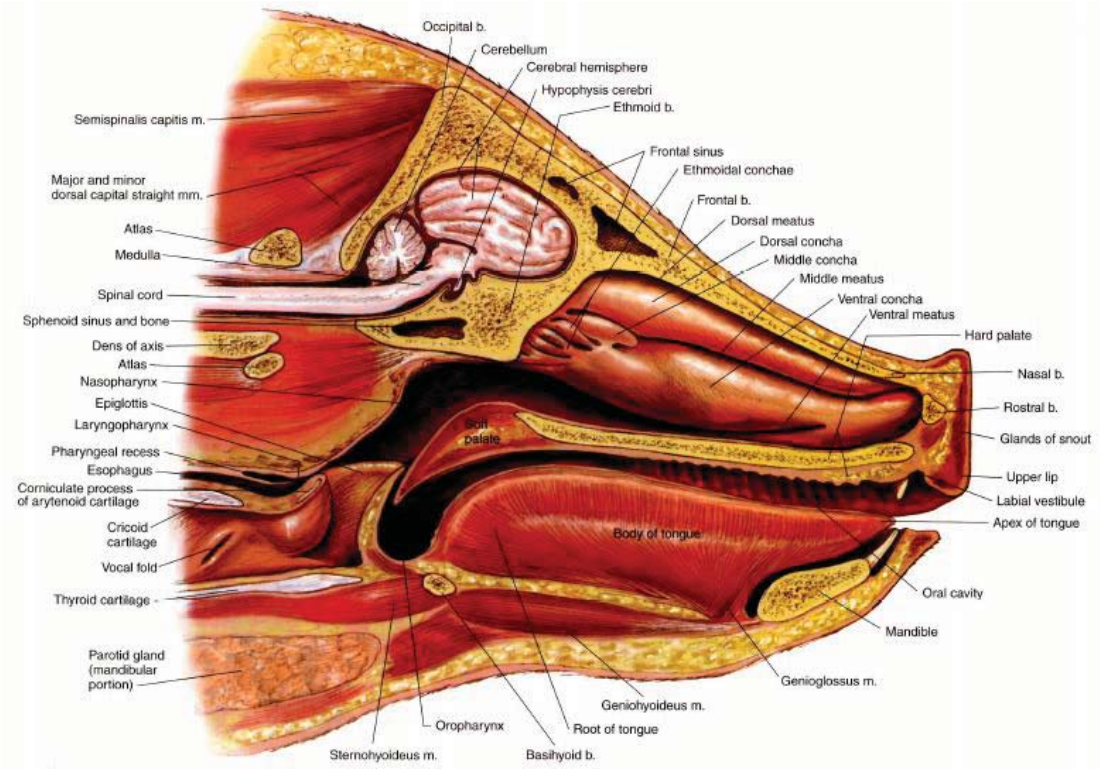

Figure 2.4 Medial view of the porcine head (adapted from McCracken, 1999).

With an emphasis on comparing human and porcine neural maturity, Dickerson and Dobbing conducted preliminary studies for determining the general similarities in CNS development between various mammalian species. Assuming that the interspecies differences were minimal in basic biological components such as myelin, they investigated the times corresponding to the pre-natal growth and post-natal component growth for various species. Based on their analysis of the growth rate for brain mass in pigs and humans, Dickerson and Dobbing determined that both mammalian species possessed comparable initial life-spans, suggesting that porcine neural tissue was a suitable surrogate for human neural tissue (Dickerson, 1966).

In their 1998 study, Thibault and Margulies further substantiated these interspecies similarities in neural development by graphically comparing the human and porcine data for DNA-P, cholesterol, and water content, which can be seen in Figure 2.5.

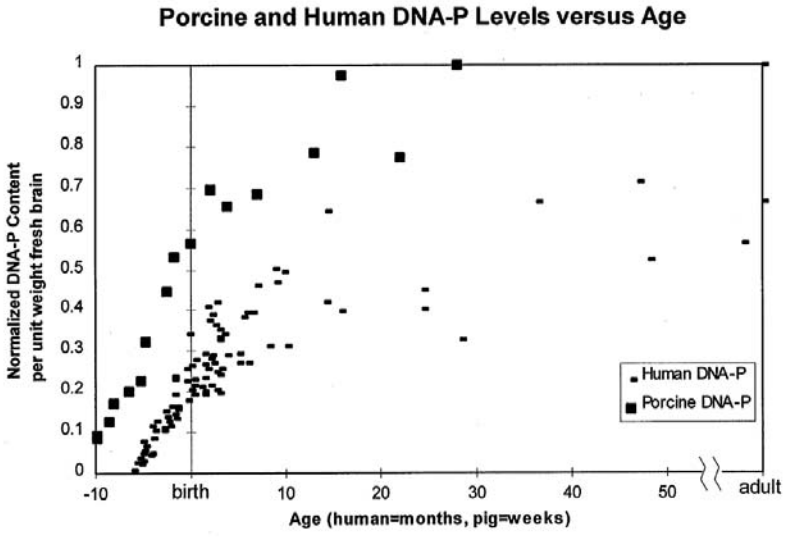

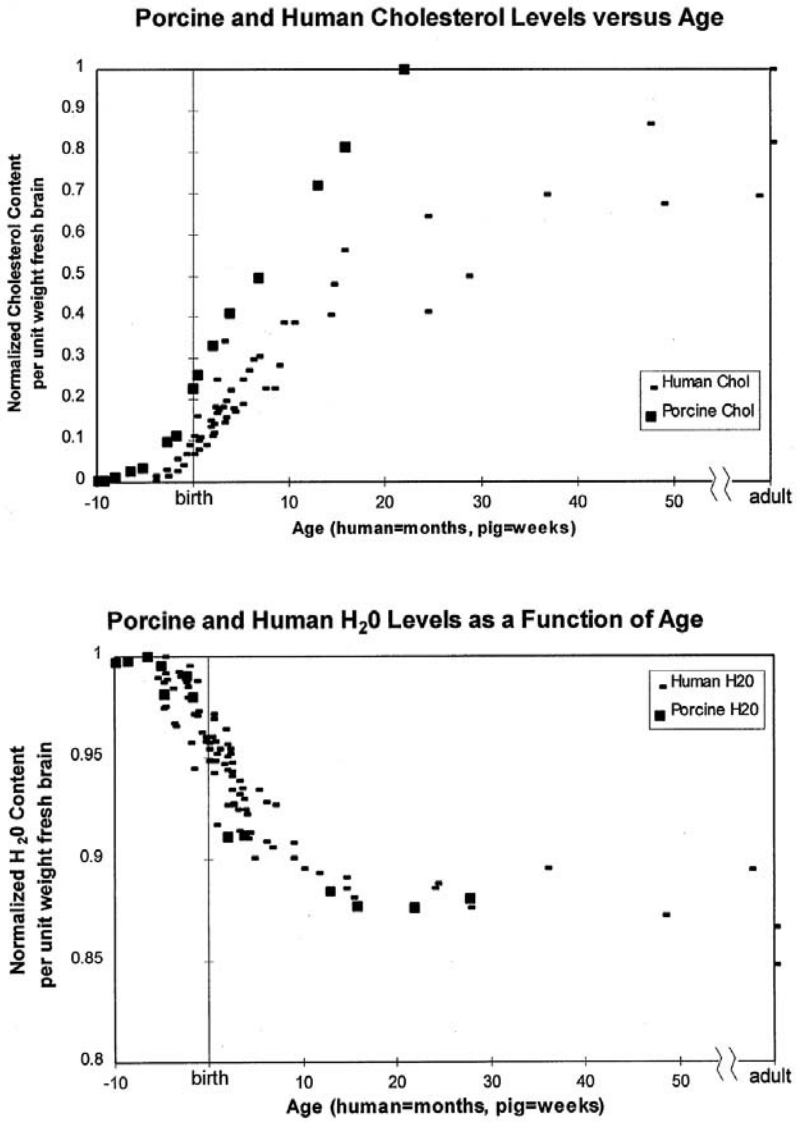

Figure 2.5 Comparison of normalized biological constituents in the early developmental stages of porcine and human specimens (adapted from Thibault, 1998).

Thibault and Margulies also promoted the utilization of pigs over human cadavers by highlighting the easier control of experimental parameters such as post-mortem time, age, and cause of death, which can significantly alter the inherent mechanical properties of brain tissue. As a result, healthy adult pigs were justified as

being viable replacements for adult humans of comparable age in testing scenarios. Furthermore, attention was specifically given to the brainstem for being a primitive section of the CNS in all quadrupeds that is both continuous with the forebrain and responsible for mediating vital physiological functions. Due to the biological similarity, the brainstem of higher level mammalian species such as pigs were considered to be suitable surrogates for the human brainstem (Thibault, 1998).

Lind and colleagues supported the use of pigs for neurological research by discussing porcine physiological aspects such as maturity and neuroanatomy. Based on comparisons in the overall development between porcine and primate specimens, pigs attain puberty within 5 to 6 months, have longer life-spans from 12 to 15 years, and maintain shorter gestation periods from 113 to 115 days. In contrast to alternate mammalian species such as rats, the porcine cerebral cortex is similar to humans with a gyrencephalic (wrinkled) surface while the rat cerebral cortex possesses a lissencephalic (smooth) surface. Depending on factors such as breed and duration of domestication, porcine brains can also reach weights from 80 to 180 g, which is 50 times higher than that of rat brains and similar in neural mass to multiple primate species previously utilized for neurological research. In addition, a coefficient for depicting brain geometry called the dimensionless isomorphy factor was used for assessing the physical features of the human, rat, and porcine brain. While formalin fixed human brains and porcine brains had reasonably comparable isomorphic values of 65 and 50, respectively, the rat brain had an isomorphic value of only 10 (Lind, 2007).

Compression Experimentation

Aside from human (HB) and primate (MB) specimens, researchers have subjected porcine (PB), bovine (BB), rabbit (RB), rodent (RMB), and feline (CB) specimens to different loading conditions such as compression (C), shear (S), and tension (T). Numerous test types have also been employed and include the following: dynamic experimentation (DE) with a strain/frequency sweep, stress relaxation (SR), constant strain rate (CSR), probe indentation (PI), creep (Cr), and elastic cylinder expansion (ECE). In addition, various brain regions comprised of gray matter, white matter, or a combination of both have been selected for testing and include the cerebrum (Cb), corpus callosum (CC), corona radiata (CR), thalamus (T), midbrain (Mb), brainstem (Bs), and cortical gray matter (CGM). Table 2.2 provides an overview of previous research attempts to comprehensively determine brain mechanical behavior. Parameters indicated by the Table 2.2 include the tissue donors, the experimental state of test specimens, the specific regions of extraction, the loads applied, and the testing mode utilized.

Table 2.2 Summary of prior research on the mechanical properties of brain tissue (adapted from Hrapko, 2008).

	Donor	State	Region	Load	Test
Arbogast et al. [21,22,27,50]	PB	vtr	Bs,Cb,T,CR	S	DE,SR,CSR
Bilston et al. [28,29]	BB	vtr	CC	S	DE,SR,CSR
Brands et al. [30–32]	PB	vtr	T	S	DE,SR
Cheng and Bilston [51]	BB	vtr	CR	C	SR,CSR
Darvish and Crandall [24]	BB	vtr	CR	S	DE
Dodgson [52]	RMB	vtr	—	C	Cr
Donnelly and Medige [25]	HB	vtr	CC,Mb	S	CSR
Estes and McElhaney [53]	HB,MB	vtr	CR	C	CSR
Fallenstein et al. [48]	HB,MB	vv,vtr	Cb	S,C	DE,PI
Franceschini et al. [54]	HB	vtr	Cb,CC,T	T,C	CSR,Cr
Galford and McElhaney [55]	HB,MB	vtr	Cb	C	DE,SR,Cr
Garo et al. [34]	PB	vtr	T	S	DE,CSR
Gefen et al. [56,57]	PB,RMB	vv,vtr	CGM	C	PI
Hrapko et al. [33]	PB	vtr	CC	S	DE,SR,CSR
Koeneman [58]	RB,RMB,PB	vtr	Cb	C	DE,Cr
McElhaney et al. [43]	HB,MB	vv,vtr	Cb,CGM	S,C	DE,CSR,PI
Metz et al. [42]	MB	vv,vtr	CGM	C	ECE
Miller [59–61]	PB	vv,vtr	Cb,CGM	C,T	CSR,PI
Nicolle et al. [19,20]	PB,HB	vtr	CR,T	S	DE,SR
Ning et al. [62]	PB	vtr	Bs	S	CSR,SR
Ommaya [3]	MB,CB	vtr	CGM	C	PI
Peters et al. [41]	BB	vtr	CR,Mb	S	DE,SR
Prange et al. [17,23,35,36]	PB,HB	vtr	CR,CC,T	S,C	SR
Shen et al. [39]	PB	vtr	Cb	S,C	DE,SR,CSR
Shuck and Advani [40]	HB	vtr	CR,T	S	DE
Velardi et al. [63]	PB	vtr	CR,CC,CGM	T	CSR
Takhounts et al. [18,26]	BB,HB	vtr	Cb	S	SR
Thibault and Margulies [37,38]	PB	vtr	Cb	S	DE
Wang and Wineman [49]	MB	vv,vtr	CGM	C	DE,PI

Several studies investigating neural mechanical properties have placed an emphasis on unconfined compression testing. In a 1997 study, Miller and Chinzei performed unconfined compression experiments at quasi-static strain rates of 0.64, 0.64 x 10^{-2}, and 0.64 x 10^{-5} s^{-1}. Porcine test specimens possessed a cylindrical geometry with average heights of 13 mm and average diameters of 30 mm while the upper and lower surfaces of each test specimen were distinguished by the sulci of the ventricle surface and the arachnoid membrane, respectively. As shown in Figure 2.6, the testing device was a UTM-10T (Orientec) tensile stress machine with a load cell capable of measuring compressive forces from 0.5 to 9.0 N for loading velocities from 0.005 to 500 mm/min.

In addition, the vertical displacement was measured by a micrometer with an electronic analog output while the radial displacement was measured by a laser distance meter LB-02/LB-62 (Keyence). Polytetrafluoroethylene (PTFE) sheets were also attached to both the movable platen and supporting base to minimize friction forces, and CCD camera images were utilized to record the entire testing procedure, which was conducted at room temperature (22°C).

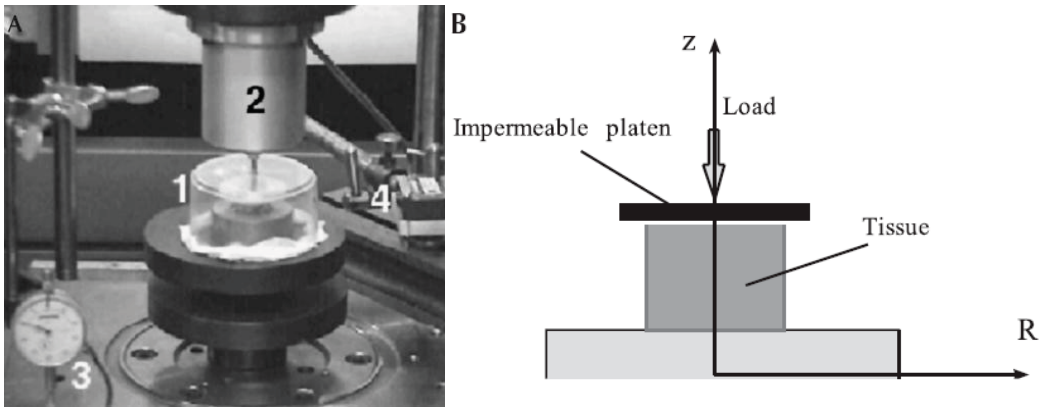

Figure 2.6 (A) General view of experimental setup including (1) the test specimen and movable platen, (2) the load cell for determining axial force, (3) the micrometer for determining axial displacement, and (4) the laser device for determining radial displacement. (B) Schematic representation of experimental layout with coordinate axes (adapted from Miller, 2000).

Based on the stress-strain relationships derived from the experimental data, both nonlinear behavior and strain rate dependency were evident. Furthermore, the compressive testing results revealed that the stiffness was evidently higher when compared to the stiffness in previous tensile testing of porcine brain tissue. Experimental data also indicated that the stresses recorded at the highest strain rate of

0.64 s^{-1} were 10 times higher than the stress obtained at the lowest strain rate of 0.64 x 10^{-5} s^{-1} (Miller, 2006).

In a 2007 study on porcine white matter, Cheng and Bilston correlated a poroviscoelastic (PVE) model with the stress relaxation response obtained from previous unconfined compression experiments. Cylindrical test specimens were an estimated thickness and diameter of 4 mm and 20.5 mm, respectively, and were extracted from the corpus callosum using a biopsy punch and surgical knife. Artificial cerebrospinal fluid (ACSF) was also utilized for hydrating test specimens prior to testing, and a stepwise preloading procedure was employed at a strain rate of 0.04 s^{-1} for 1800 seconds to allow the interstitial fluid to dissipate until the monitored relaxation curve fell below 0.0004 g/s. The compression experiments were performed at a ramp displacement of 5% for the strain rates of 0.01, 0.001, and 0.0001 s^{-1}, and an additional series of compression tests was conducted at 0.001 s^{-1} using platens modified with fine sandpaper to assess the no-slip boundary condition. The resulting peak reaction forces exhibited strain rate dependency for porcine white matter, but the equilibrium reaction force showed otherwise. In the compression phase of the experiments, the coefficients of variation were 0.35, 0.27, and 0.24 for the strain rates of 0.01, 0.001, and 0.0001 s^{-1}, respectively. For the stress relaxation phase, the coefficient of variation for the intermediate and highest strain rate was 0.4 while the coefficient of variation for the lowest strain rate was 0.67. A comparison of statistical parameters revealed the coefficients to be lower than those reported in a 1970 study by Estes and McElhaney in which preloading of test specimens was not employed (Cheng, 2007).

In a 2007 study, Tamura and colleagues utilized the test apparatus shown in Figures 2.7 and 2.8 to conduct a series of high-rate unconfined compression experiments on porcine brain tissue at loading velocities of 12, 120, and 600 mm/s, which corresponded to respective strain rates of 1, 10, and 50 s^{-1}. The cylindrical test specimens were cored out from the cerebral cortex and corona radiata and were an estimated height of 14.2 ± 0.2 mm and diameter of 22.1 ± 0.1 mm. Test specimens were also frozen for approximately one hour to facilitate the removal of the thin surface layer on the cerebral cortex known as the pia mater. Physiological saline (37°C) was also applied to the upper and lower surfaces of test specimens to maintain hydration and to employ a pure-slip condition while mechanical testing was performed at room temperature (20°C).

Cylindrical test specimens were compressed by a platen attached to the tester crosshead, which was driven by a programmable linear actuator (F20-20BK-11, Kyowa) capable of reaching maximum velocities up to 1200 mm/s. The load cell (LUR-A-50NSA1, Kyowa) was located underneath the specimen stage and possessed a load measurement range from -50 to +50 N. Whenever the crosshead hit the stoppers and produced a tensile force reading exceeding 40 N, it magnetically detached from the actuator to prevent overload damage to the load cell. High-speed cameras (Memrecam Ci-3-J, NAC) were also used for visually confirming contact between the platen and specimen. In addition, a laser displacement meter (LK-G85, Keyence) was used for detecting the axial position of the tester crosshead while a laser-sheet radial displacement meter (LS-7070, Keyence) was used for measuring the specimen diameter.

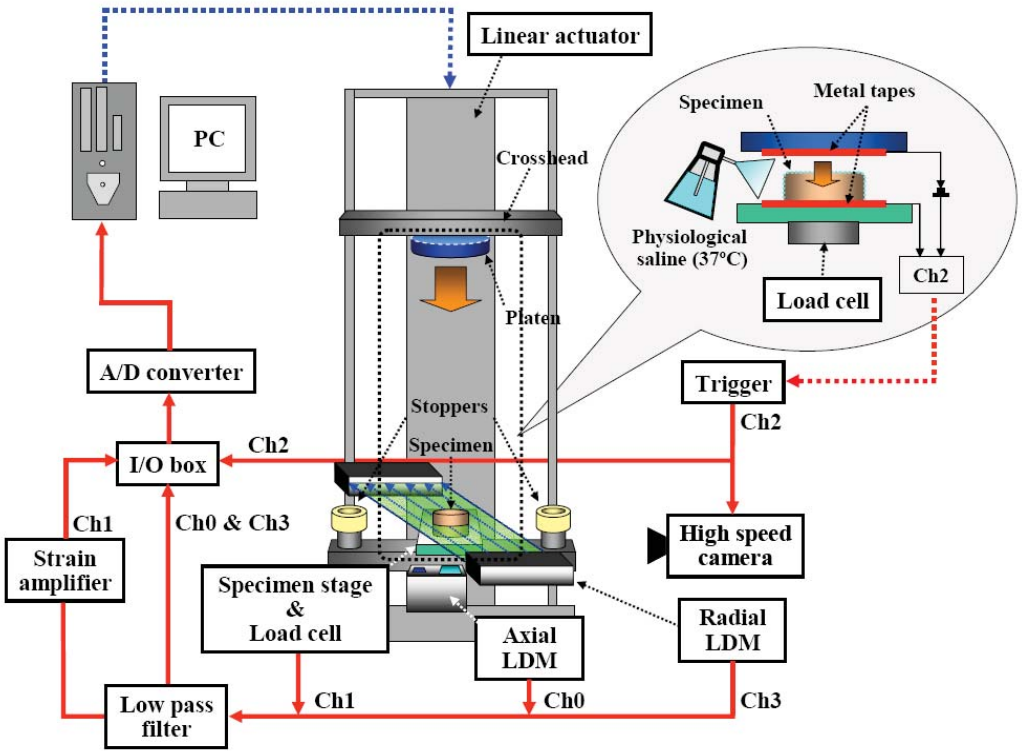

Figure 2.7 Overall schematic representation of the testing device used for high-rate unconfined compression experiments (adapted from Tamura, 2007).

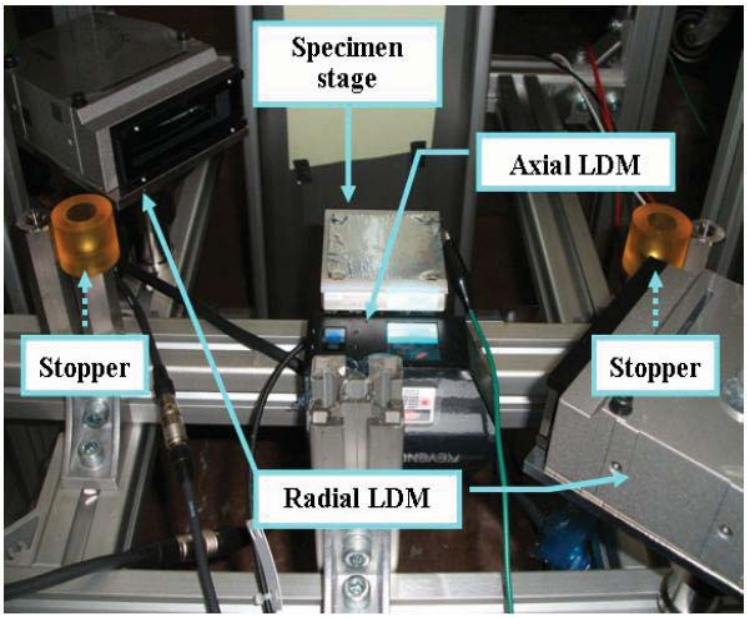

Figure 2.8 Images of the components for measurement (adapted from Tamura, 2007).

Aside from strain rate dependency, the effects of anatomical origin, orientation, and freezing on test specimens were also investigated. Stress-strain relationships and unpaired *t*-tests on the experimental data suggested that from a macroscopic perspective, test specimens obtained at different orientations and from varying brain regions did not significantly affect mechanical properties for the strain rate of 1 s^{-1}. Furthermore, similar data and statistical analysis also suggested that from a macroscopic perspective, there was no significant difference between the elastic moduli of fresh and frozen porcine brain tissue for the strain rate of 1 s^{-1} (Tamura, 2007).

Tension Experimentation

In addition to compression testing, investigations into neural mechanical properties have resulted in numerous experiments with an emphasis on tensile testing of brain tissue. In a 2002 follow-up study of their previous work with unconfined compression testing, Miller and Chinzei performed another series of tensile experiments to confirm that tissue constitutive models depicting compressive mechanical behavior were considerably different from models characterizing tensile behavior. Although the protocols for sample procurement and preparation were identical to those from prior compression testing, other experimental parameters had to be modified. As seen in Figure 2.9, the testing device was a Tensilon Universal Testing Instrument (TMI model TM-1T, Toyo Baldwin, Japan) and was capable of measuring vertical forces from 0.5 to 9.0 N and loading velocities from 0.005 to 500 mm/min. Cyanoacrylate (Cemedine, Japan) was utilized to attach the specimen to a glass plate, which was then screwed into

the test apparatus itself. Before tension experiments were initiated, the upper platen was lowered 1 mm for 20 s to provide reasonable time for proper adhesion. The upper platen was then reversed 1 mm to its original contact position and remained stationary for 1 min before the actual test was conducted. Eleven tests were performed at the fast loading velocity while 10 were performed at the medium velocity, which corresponded to strain rates of 0.64 s^{-1} and 0.64 x 10^{-2} s^{-1}, respectively. The lowest strain rate of 0.64 x 10^{-5} s^{-1} could not be employed because it required the upper platen to be operational for over 11 hours, thereby leading to insufficient adhesion at the tissue interface.

Plots of the average Lagrange stress versus time were derived using the initial cross-sectional area of test specimens in order to assess the reliability of the measured forces. The coefficient of variation for the medium strain rate of 0.64 x 10^{-2} s^{-1} was 0.2, which was comparable to the coefficient reported by Miller and Chinzei (1997) and significantly lower than the value of 0.5 given by Estes and McElhaney (1970). On the other hand, the coefficient of variation for the highest strain rate of 0.64 s^{-1} was 0.5, which was higher than the coefficient obtained from prior compression testing by Miller and Chinzei (1997) but similar to the value reported by Estes and McElhaney (1970).

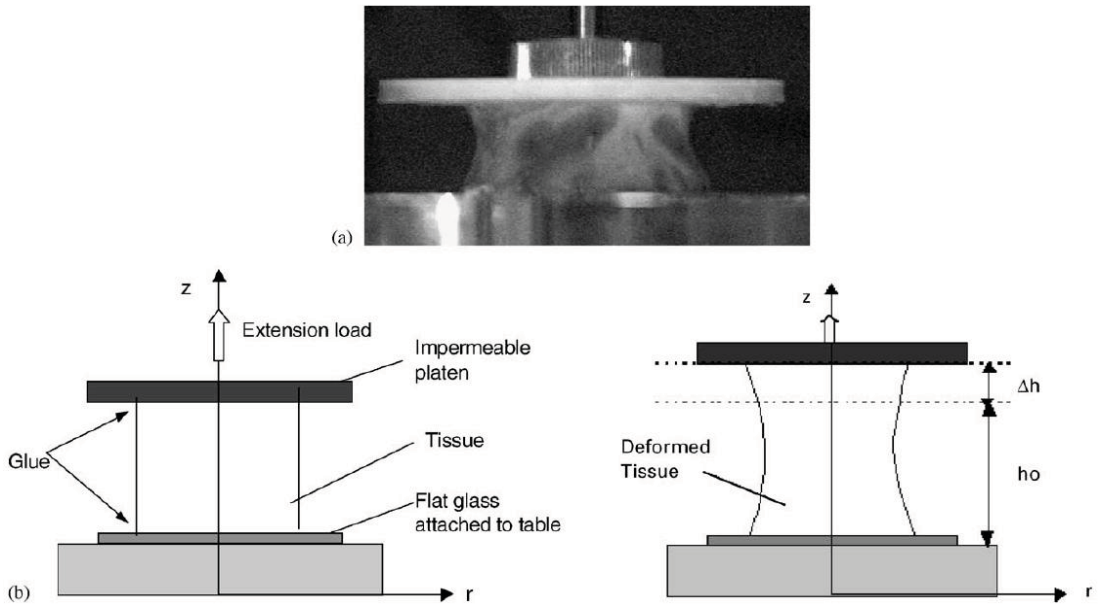

Figure 2.9 (a) Porcine test specimen subjected to tensile forces. (b) Schematic representation of the experimental setup (adapted from Miller, 2002).

The inherent biological variability of test specimens procured from eight different pigs led to deviations from the ideal cylindrical configuration of up to 4%, but necking of test specimens throughout testing remained consistent. Despite these experimental limitations, however, the resulting stress-strain plots were convex downward for all tensile rates, and strain rate dependency was confirmed since the tissue response stiffened as the loading velocity increased (Miller, 2002).

In a 2006 study, Franceschini and associates applied cyclic testing using the computer driven tensile device (μ-Strain Instrument ME 30-1, Messphysik, Austria) shown in Figure 2.10 at a loading velocity of 5 mm/min, which corresponded to initial quasi-static strain rates from 5.5 to 9.3 x 10^{-3} s^{-1}. 86 prismatic and cylindrical test specimens were extracted from multiple locations at two different directions along the

sagittal and frontal planes, as seen in Figure 2.11, and characterized by aspect ratios from 0.9 to 2.5. Test specimens were also temporarily preserved in 0.9% physiological saline solution at a steady temperature of 37°C before being attached to Plexiglas platens using commercial adhesive.

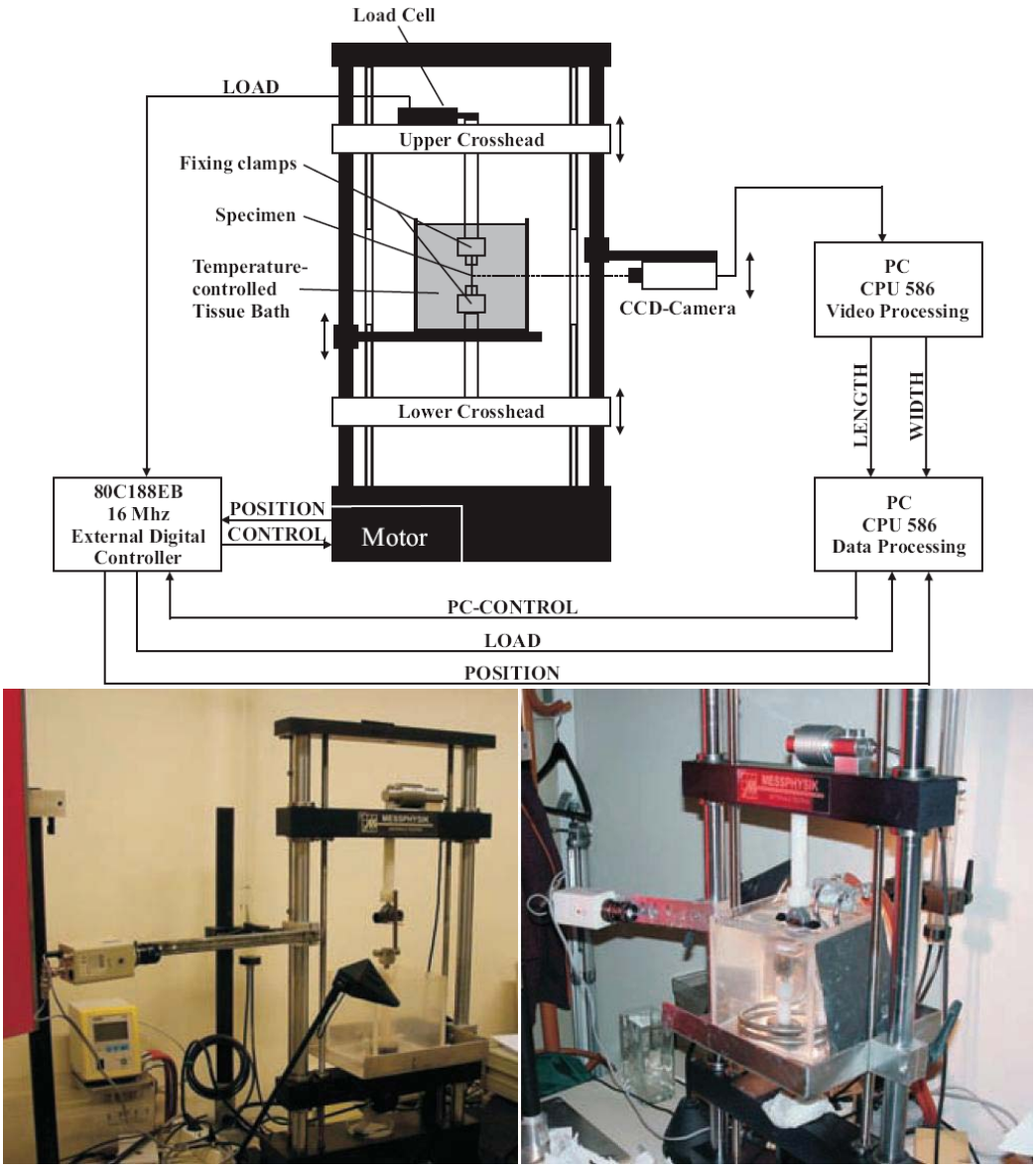

Figure 2.10 (TOP) Schematic diagram of the cyclic experimental setup. (BOTTOM) Photos of different components in the cyclic experimental setup (adapted from Franceschini, 2006).

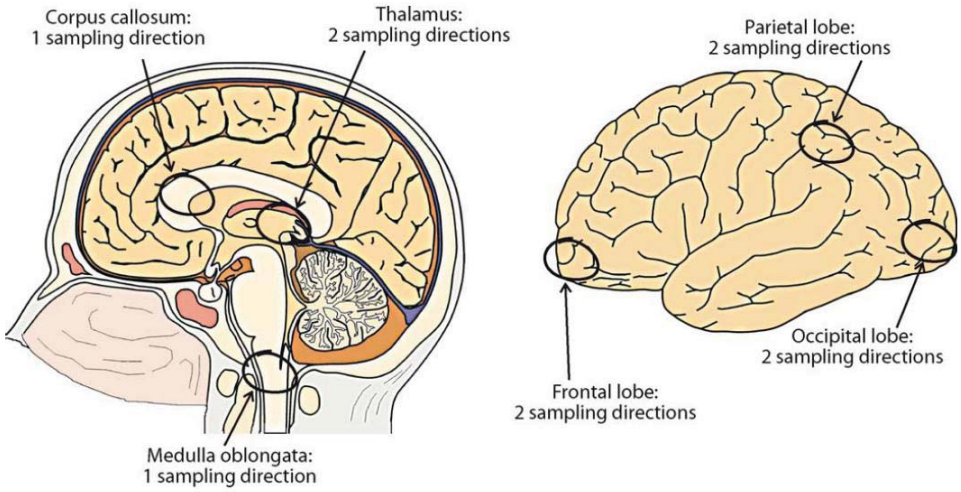

Figure 2.11 Extraction locations and directions of test specimens (adapted from Franceschini, 2006).

Preliminary loading cycles were continually applied until sufficient strain, damage, and failure was observed. Maximum loads of 0.03 N were initially applied but eventually calibrated according to the resulting tissue response. Afterwards, loading cycles were adjusted by increments of 0.02 N up to 0.12 N, the level at which test specimens were monotonically loaded until failure. Based on experimental results, it was determined that permanent deformations propagated throughout the tissue during cyclic tensile testing. Furthermore, most test specimens failed in the contact region by the Plexiglas platens while 13 failed within the gage region of the test setup, providing more insight to the damage evolution.

Shear Experimentation

Although compression and tension experiments were initially applied for determining neural mechanical properties, numerous shear experiments have also been

utilized to assess the biomechanical behavior of brain tissue. Aside from differences in experimental protocols involving dynamic, stress relaxation, and constant strain rate testing, researchers have studied the variations in donor age, which include specimens that were pediatric (P), nfg (not full grown), and full grown (fg). Researchers have also accounted for temperature (T) as well as varying methods for specimen attachment, which involve the absence of glue (no), use of glue (g), use of sandpaper (sp), or use of a roughened surface (rs). Table 2.3 displays an overview of previous research attempts to comprehensively determine the mechanical behavior of the brain undergoing shear deformations. The dynamic testing parameters indicated by Table 2.3 include the age for each donor, the post-mortem time, the method of attaching test specimens, the temperature, the applied frequencies, and the percentage strain level attained. In addition, the relaxation time is specified under the stress relaxation testing parameters while the strain rate is shown under the constant strain rate testing parameters.

Table 2.3 Summary of prior research on the mechanical properties of brain tissue in shear (adapted from Hrapko, 2008).

	Donor age	Postmortem time (h)	Attach. method	T (°C)	Frequency (Hz)	Strain (%)
Dynamic tests						
Arbogast et al. [21,22,27]	p,fg	4	no,g,rs	5–25	20–200	2.5,5,7.5
Bilston et al. [28,29]	—	8	sp	37	0.01–20	0.015–2
Brands et al. [30,31]	nfg	4	sp,no,g	4–38	0.1–16	0.1–10
Darvish and Crandall [24]	nfg	72–288	g	37	0.5–200	1–20
Fallenstein et al. [48]	fg	2.5–62	g,rs	37	9–10	7–24.5
Garo et al. [34]	nfg	2–10	sp	37	1–10	1
Hrapko et al. [33]	nfg	5	sp	37	0.04–16	1
McElhaney et al. [43]	fg	2.5–15	no	37	9–10	–
Nicolle et al. [19,20]	nfg	24–48	g	37	0.1–9000	0.01–10
Peters et al. [41]	nfg	27–51	—	7–37	0.016–16	0.2–5
Shen et al. [39]	fg	48–120	sp	10–37	0.016–16	0.04–400
Shuck and Advani [40]	fg	—	–	37	5–350	1.23
Thibault and Margulies [37,38]	p,fg	3	no	~25	20–200	2.5,5
	Donor age	**Postmortem time (h)**	**Attach. method**	**T (°C)**	**Strain (%)**	**Relax. time (s)**
Stress relaxation tests						
Arbogast et al. [21]	p	4	no	~25	2.5,5,7.5	1.8
Bilston et al. [28,29]	—	8	sp	37	0.001–15	3000
Brands et al. [31]	nfg	4	sp	38	5–20	100
Hrapko et al. [33]	nfg	5	sp	37	1–20	10
Nicolle et al. [19,20]	nfg	24–48	g	37	0.1–50	300
Ning et al. [62]	p	5	no	—	2.5–50	60
Peters et al. [41]	nfg	27–51	—	7–37	1	300
Prange et al. [17,23,35,36]	p,nfg,fg	3—5	no	~25	2.5–50	60
Shen et al. [39]	fg	48–120	sp	10–37	0.5,5,10,20	2
Takhounts et al. [18,26]	fg	48	g	~25	12.5–50	0.5
	Donor age	**Postmortem time (h)**	**Attach. method**	**T (°C)**	**Strain rate (s^{-1})**	**Strain (%)**
Constant strain rate tests						
Arbogast et al. [21]	p	4	no	~25	—	8
Bilston et al. [29]	—	8	sp	37	0.055,0.2335,0.947	2000
Donnelly and Medige [25]	fg	72–96	g	~25	30,60,90,120,180	0.28–12.5
Garo et al. [34]	nfg	2–10	sp	37	1	5
Hrapko et al. [33]	nfg	5	sp	37	1,1.5	1–50
Ning et al. [62]	p	5	no	—	20–25	50

In a 1997 study, Donnelly and Medige designed and fabricated the parallel-plate shear testing system shown in Figure 2.12 for experiments at strain rates of 0, 30, 60, and 90 s^{-1}. Shear displacements were generated at a constant velocity between the stationary upper plate and mobile lower plate. A linear motor was utilized for driving an impact cart into the lower plate to produce shear deformations without inertial stresses created due to acceleration. The reaction forces along the stationary plate were

measured with a piezoresistive crystal force transducer (Kistler Instrument Corp., 9251A) while the velocity of the mobile plate with respect to the stationary plate was measured with a velocity transducer (Trans-tek 100-001).

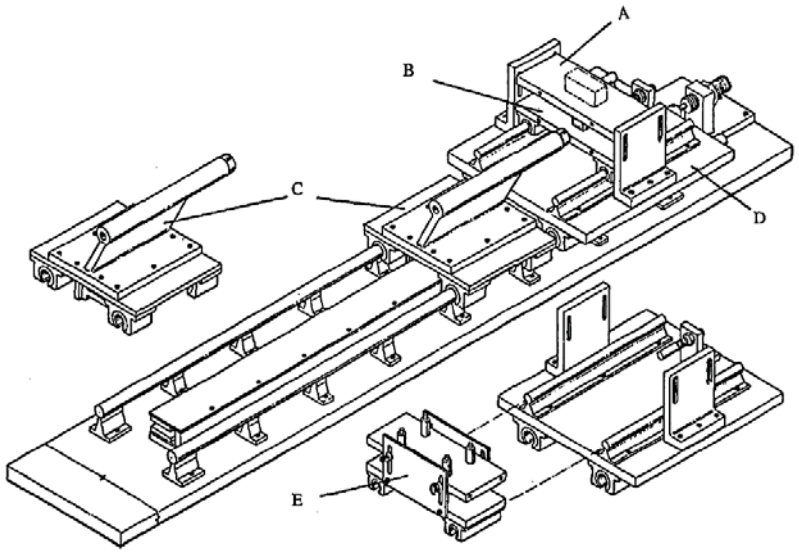

Figure 2.12 Schematic layout of the high rate shear testing device exhibiting the (A) upper fixed shear plate, (B) lower mobile shear plate, (C) impact cart, (D) test cart, and (E) sample cart with removable side plates (adapted from Donnelly, 1997).

Over a 9-month span, human brain specimens were gathered from 5 male and 7 female cadavers with an average age of 77 years. Cadavers were typically obtained within 3 days while testing commenced usually within 2 days after brain specimens were acquired. Moreover, there were no attempts to assess the influences of both gender and age. Viable results were collected from 125 test specimens, which had a mean length and cross-sectional area of 1.20 ± 0.15 cm and 2.32 ± 0.10 cm^2, respectively. A 12% reduction in diameter was also observed when test specimens were

cored from the corona radiata and the midbrain, which constituted a mixture of both white and gray matter. Other extraction locations, however, predominantly contained white matter with negligible amounts of gray matter from the cerebral cortex. Despite the consistency in maintaining a cylindrical geometry for all test specimens, researchers made no attempts to determine the relative influences from the varying contributions of white and gray matter.

Plots of shear force versus time generally exhibited an increasing monotonic behavior, where the minimum shear force recorded at maximum displacement was 0.07 N for a strain rate of 0.34 s^{-1} while the maximum shear force recorded at maximum displacement was 2.16 N for a strain rate of 59.5 s^{-1}. In addition, the amplitudes for the quasi-static and dynamic experiments were 1070 Pa and 33.5 kPa, respectively. Although there were no trends in the experimental data due to the sample location and quality, strain rate effects were evident between 0 s^{-1} and the higher strain rates and also between 30 s^{-1} and 90 s^{-1}. A statistical procedure involving the proportion of variance in the dependent variables also revealed that 47% of the variance was attributed to the strain rate, 30% was attributed to the brain specimen, and the remaining 23% was attributed to experimental error.

Since the human brain is comprised of white matter, gray matter, fissures, membranes, blood vessels, and voids surrounded by cerebrospinal fluid (CSF), an exhaustive description of its diverse mechanical properties is required. In order to accurately correlate brain deformations with impact and injury, Donnelly and Medige applied assumptions that characterized the brain as a viscoelastic material with

continuous, homogenous, and isotropic properties. The brain was also considered to be incompressible according to prior work from both Stalnaker (1969) and McElhaney (1976), which revealed that the bulk modulus of K = 2100 MPa was 10^5 times larger than the shear modulus. In general, the high rate shear testing by Donnelly and Medige exhibited a dependence on strain rate but no correlation to either the extraction location or specimen condition. Stress-strain plots also illustrated nonlinear behavior with rising slopes as both strain rate and percentage strain increased, and the corresponding data were eventually fit to a single nonlinear viscoelastic solid model (Donnelly, 1997).

Researchers at the University of Pennsylvania also utilized shear experiments to gain a more complete understanding of the mechanical behavior of brain tissue. In a 1997 study, Arbogast and Margulies investigated the differences in material response for two porcine CNS regions, the brainstem and the cerebral cortex. In order to perform experiments at loading rates comparable to tissue deformations in traumatic brain injury, Arbogast and Margulies built the custom-designed oscillatory shear device shown in Figure 2.13. Test specimens were positioned between two parallel plates with coarse glass coverslips attached. The lower plate was secured to a linear bearing for support, and its displacement was monitored by a LVDT-Model 232 (Trans-Tek, Ellington, CT) connected to the linear bearing. The fixed upper plate was fitted with an isometric force transducer-Model BG (Kulite Semiconductor Products, Leonia, NJ) to measure the forces transmitted through test specimens. After contact was confirmed between the upper plate and the test specimen, a combination of a function generator and a power

operational amplifier was utilized for producing sinusoidal motions in the bottom plate according to the designated frequency and amplitude.

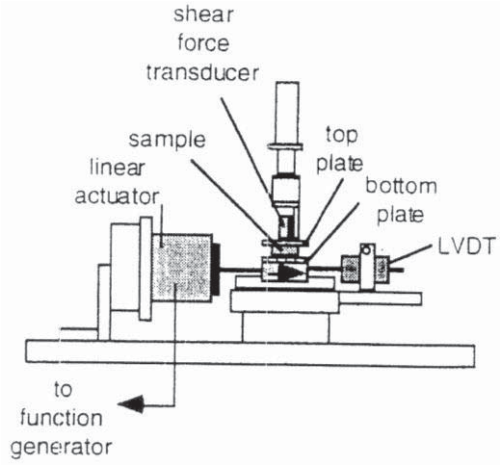

Figure 2.13 Schematic of the custom-designed shear testing apparatus (adapted from Arbogast, 1997).

In order to minimize potential dehydration, saline was heated to 100°C and fed into a Plexiglas chamber surrounding the parallel plates, thereby creating a high humidity environment. Cyclic simple shear experiments were performed over a frequency range from 20 to 200 Hz at 10 Hz increments to strain levels of either 2.5% or 5.0%. 42 brainstem specimens and 12 cerebral specimens were selected for oscillatory shear experiments, which were completed within 4 hours after sacrifice to minimize various factors such as age, cause of death, and post-mortem time. At 2.5% strain, the storage modulus of brainstem was nearly 20% higher than the cerebral cortex, and at 5.0% strain, both the storage and loss moduli for the brainstem were almost 80% higher than the cerebral cortex (Arbogast, 1997).

In a 1998 follow-up study, Arbogast and Margulies further analyzed the material response of porcine brainstem using an experimental protocol similar to that used for the 1997 study comparing porcine CNS regions. Brains from 1-year old pigs were retrieved from a local slaughterhouse and temporarily stored in artificial cerebrospinal fluid immediately after sacrifice. Cylindrical test specimens were procured from the brainstem in two directions with the aid of a right circular cylindrical trephine with a diameter of 11 mm. As seen in Figure 2.14, Core A specimens were extracted in the superior-inferior direction while Core B specimens were extracted in the ventral-dorsal direction.

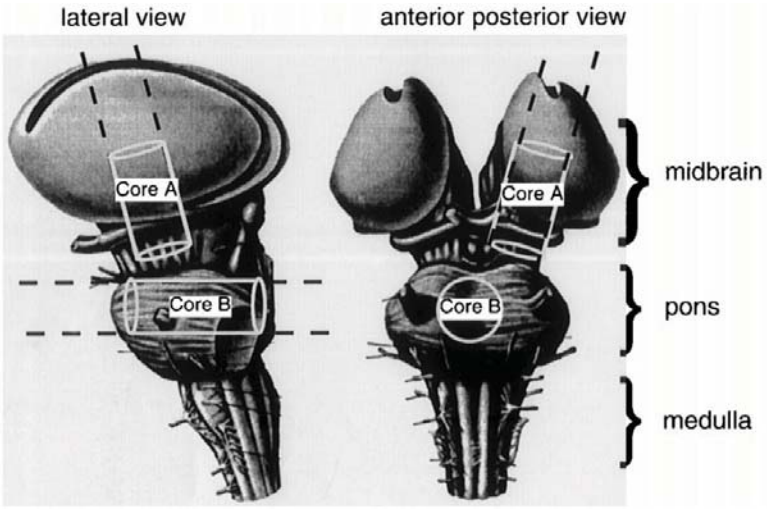

Figure 2.14 Anatomical locations and extraction orientations of test specimens (adapted from Arbogast, 1998).

Core A specimens also primarily consisted of axonal fibers that were coincident with the long axis of the cylinder while Core B specimens were mainly comprised of axonal fibers that were transverse to the long axis of the cylinder. In addition, Core A

specimens were eventually sliced into 1 mm disks and were assumed to contain the plane of isotropy, implying that the mechanical properties were independent of shear direction. As shown in Figure 2.15, the corresponding specimen configuration for Core A was orientation “TT,” distinguished by axonal fibers oriented transverse to both the shear plane and direction. The other two specimen configurations derived from Core B specimens were orientation “PP” and orientation “PT.” Orientation “PP” characterized the axonal fibers as being oriented parallel to both the shear plane and direction while orientation “PT” referred to the axonal fibers being oriented parallel to the shear plane but transverse to the shear direction.

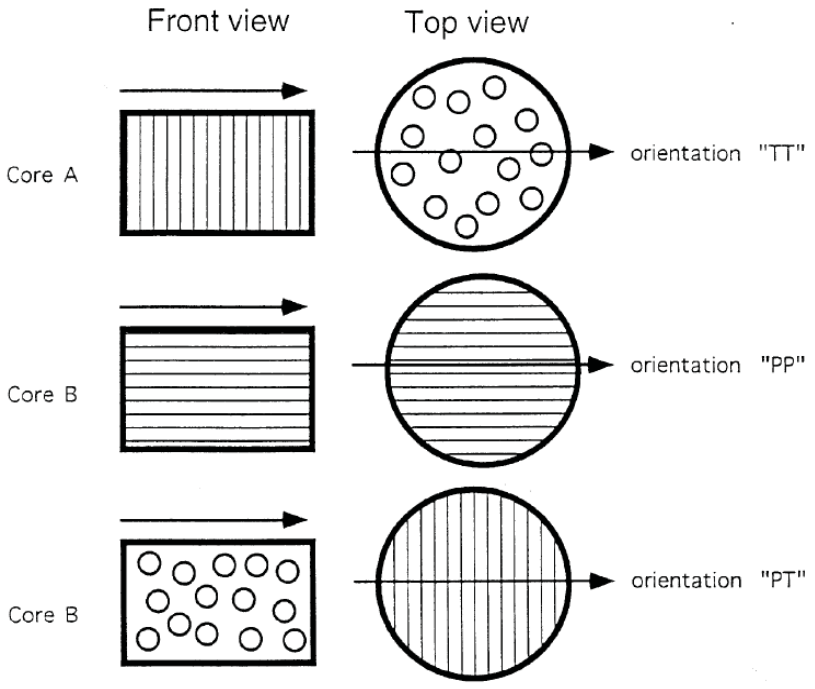

Figure 2.15 Schematic displaying the axonal fiber arrangement for different specimen configurations (adapted from Arbogast, 1998).

Shear tests were performed for each tissue orientation over a frequency range from 20 to 200 Hz at 10 Hz increments to strain levels of 2.5%, 5.0%, and 7.5%. In order to reduce the potential influences of post-mortem time, Arbogast and Margulies acquired test specimens from separate animals and completed experiments within 4 hours. Based on comparisons with prior research on cerebral tissue, the brainstem proved to be considerably stiffer than the cerebrum by at least 80%. The results also confirmed that the brainstem exhibited anisotropic behavior when exposed to shear deformations. In addition, the shear modulus was 10 to 20% higher in the transverse direction than in the plane of isotropy (Arbogast, 1998).

In another 1998 study at the University of Pennsylvania, Margulies and Thibault utilized oscillatory simple shear strain experiments to measure the degree of age-dependence in porcine cerebrum. Porcine brains were collected from pigs that were either 1 year old or 2 to 3 days old, and the extracted sections from the cerebrum and thalami were temporarily stored in artificial cerebrospinal fluid. As seen in Figure 2.16, cylindrical pieces of neural tissue were initially excised from the frontal cerebrum and eventually sliced into disk-shaped test specimens with a thickness of 1 mm and diameter from 10 to 12 mm. While test specimens were immersed in artificial cerebrospinal fluid, dial calipers were used to determine the thickness and diameter of within ± 0.1 mm.

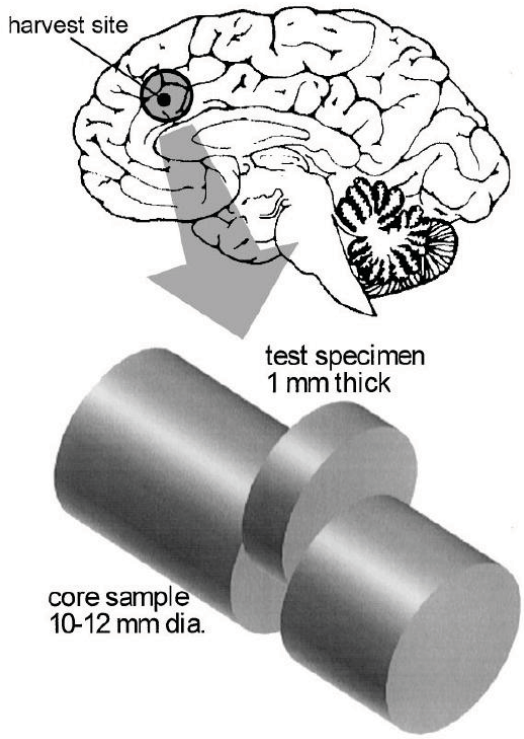

Figure 2.16 Extraction location of porcine cerebral tissue with the dimensions for test specimens also shown (adapted from Thibault, 1998).

As with previous experimental protocols, shear tests were conducted over a frequency range from 20 to 200 Hz at 10 Hz increments to percentage strain levels of 2.5% and 5.0%. Although shear strain was consistently applied to an identical plane for each test specimen, the fiber orientation was still random. According to the experimental data, both the loss and storage moduli were frequency-dependent, but not age-dependent. In addition, the complex shear moduli components demonstrated age-dependence with the exception of the storage modulus at a strain level of 5.0% (Thibault, 1998).

In a 2002 study, Margulies and Prange conducted supplementary shear experiments in order to assess regional differences in porcine neural tissue undergoing

higher levels of deformation intended to simulate traumatic brain injuries. Adult subjects were sacrificed by rapid exsanguination while pediatric subjects were sacrificed by a lethal dosage of KCl and pentobarbital. Brain specimens were temporarily stored in 4°C artificial cerebrospinal fluid, and shear testing was completed within 5 hours post-mortem.

Using a similar humidified, parallel-plate shear testing device, Margulies and Prange performed rapid stress relaxation experiments in simple shear with the tissue secured between the glass plates without adhesive and with negligible preloading. Test specimens were rectangular with the dimensions 10 x 5 x 1 mm, and they were procured from white matter regions such as the corpus callosum and corona radiata as well as gray matter regions including the thalamus. In addition, two different testing directions were designated by either D1 or D2, as shown in Figure 2.17.

For each shear test, the bottom plate was displaced with a ramp time of 60 ms and hold time of 60 s for progressive strain levels of 2.5%, 5.0%, 10%, 20%, 30%, 40%, and 50%. Furthermore, the procedure repeated for the strain level of 5.0% to confirm data consistency, and the applied strain rates ranged between 0.42 and 8.33 s^{-1}. Test specimens were also allowed to relax for 60 s before additional tests could be performed, and steady-state was confirmed for all tissue classifications at 60 s, where the last 5 seconds of testing were distinguished by stress variations of less than 0.5%.

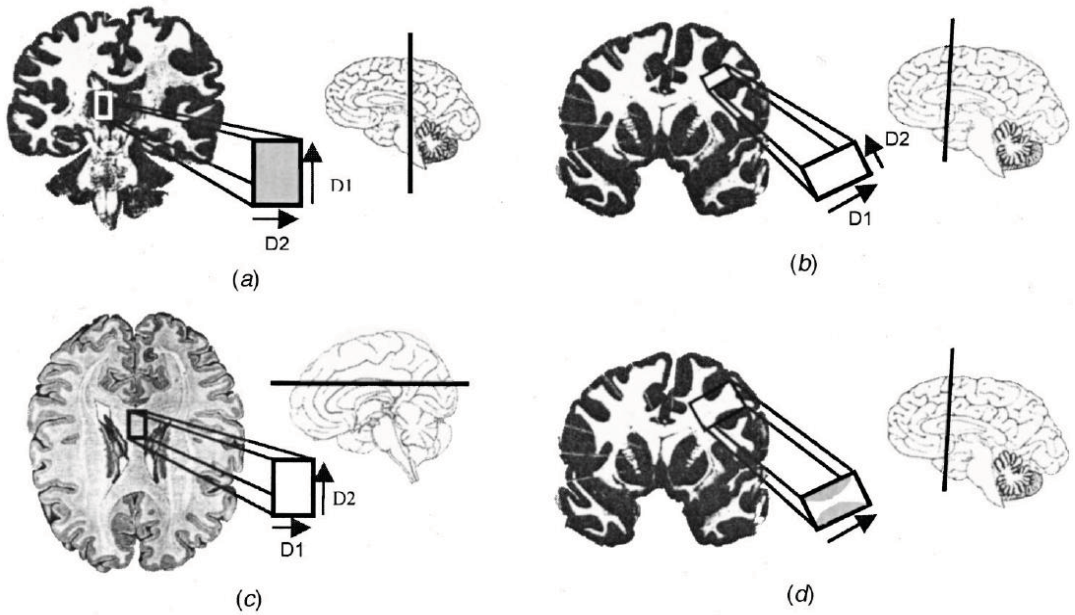

Figure 2.17 Overview of anatomical locations: (a) adult gray matter, (b) adult corona radiata, (c) adult corpus callosum, and (d) 4-week old mixture of gray and white matter (adapted from Prange, 2002).

At larger strains of up to 50%, the mechanical properties of gray matter as well as two white matter regions (corpus callosum and corona radiata) were determined to be considerably inhomogenous. The corpus callosum was considered to be the most compliant region since it was 1.3 times less stiff than gray matter. Overall, gray matter was deemed isotropic while white matter was considered to be anisotropic (Prange, 2002).

CHAPTER III

METHODS

Sample Preparation

Intact porcine heads from healthy males with weights and ages ranging from 240 to 270 lbs and 22 to 26 weeks, respectively, were collected from a local abattoir (Sansing Meat Services, Maben, MS) and transported to a nearby necropsy laboratory (College of Veterinary Medicine, Mississippi State University). Porcine brains were surgically extracted from each skull and temporarily stored in 0.01 M phosphate buffered saline (Sigma-Aldrich, St. Louis, MO) to minimize dehydration and tissue degradation. Procurement of test specimens required the use of a scalpel for slicing through the corpus callosum of each brain, thereby separating the left and right hemispheres. For unconfined compression and uniaxial tension testing, a fabricated 30 mm stainless steel die (Center for Advanced Vehicular Systems, Mississippi State University) was utilized for resecting brain material through the sagittal plane of each hemisphere, yielding cylindrical test specimens with the sulci and gyri characterizing the upper surface. For fixed-end shear testing, rectangular test specimens with dimensions 40 x 10 x 10 mm were manually excised through the sagittal plane of each hemisphere. Figure 3.1 exhibits the extraction orientations of test specimens for different testing modes.

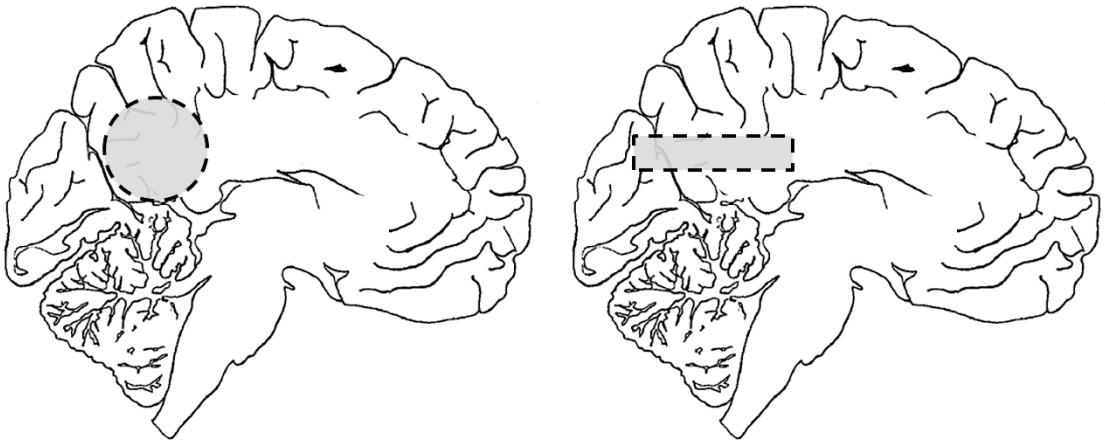

Figure 3.1 (LEFT) Sagittal view of extraction locations for cylindrical test specimens procured for unconfined compression and uniaxial tension experiments. (RIGHT) Sagittal view of extraction locations for rectangular test specimens procured for fixed-end shear experiments (adapted and modified from Donnelly, 1997).

Mach-1^{TM} Micromechanical Testing System

The Mach-1^{TM} Micromechanical Testing System (BIOSYNTECH Micromechanical Systems, Canada) was comprised of the different components seen in Figure 3.2. Although the testing system included a 10 kg load cell, the 1 kg load cell was selected to accommodate the yielding structural integrity of porcine neural tissue, thereby reducing the likelihood of encountering overload errors. Calibration of the 1 kg load cell was also necessary for producing consistent readings, and the procedure was repeated until the resulting calibration factors were within 0.1 of previous values, which can be seen in Figure 3.3.

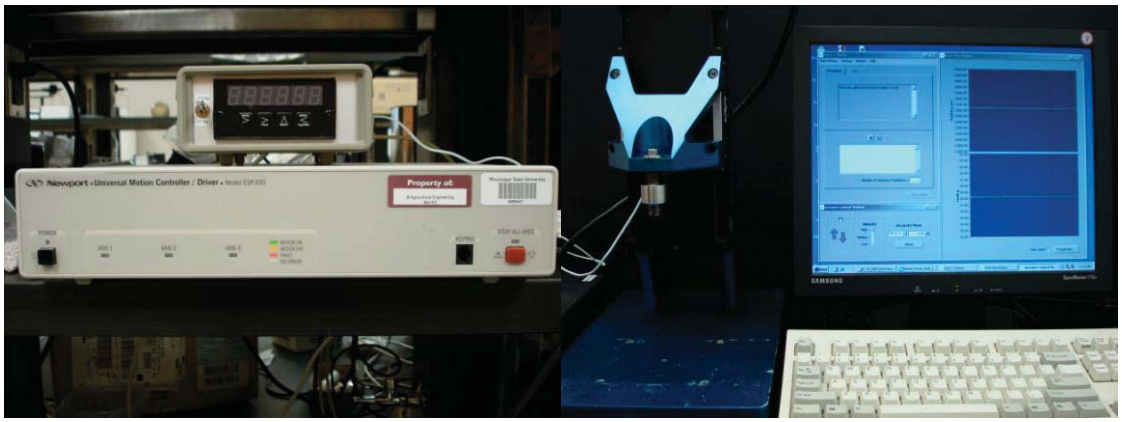

Figure 3.2 (LEFT) Load cell amplifier situated on top of the Universal Motion Controller/Driver – Model ESP300. (RIGHT) Mach-1™ testing apparatus with 1 kg load cell attached and monitor showing the sequence managing window, actuator control window, and real-time display window.

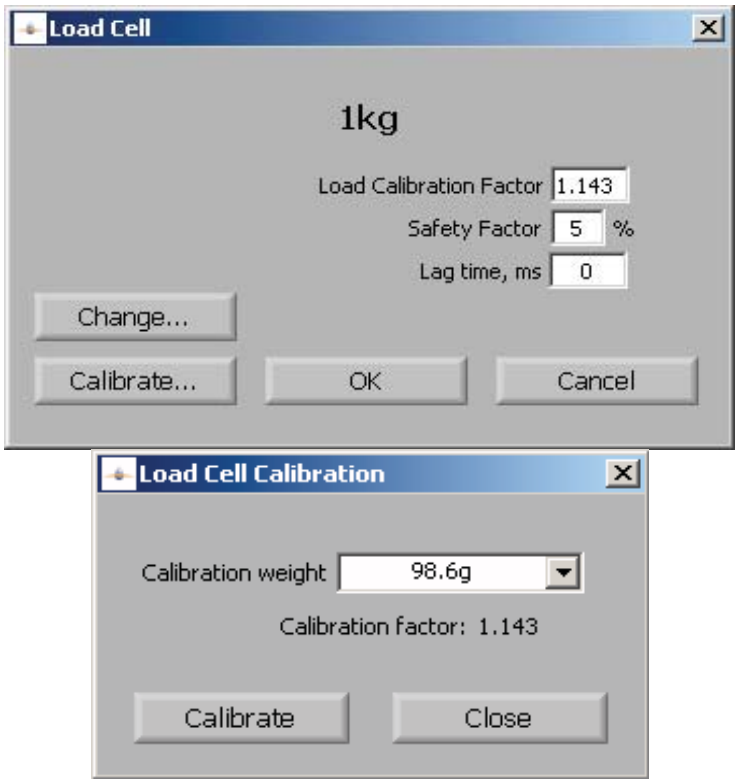

Figure 3.3 Mach-1™ Program windows required for selecting and calibrating the 1 kg load cell to adjust the load calibration factor.

Before experiments could be performed, preliminary Mach-1™ programs were built with the Find Contact command for precisely measuring the initial height of test specimens. As shown in Figure 3.4, the sequence managing window was then utilized for configuring experimental parameters such as the strain distance (µm) and loading velocity (µm/s) and for designating the saved file locations.

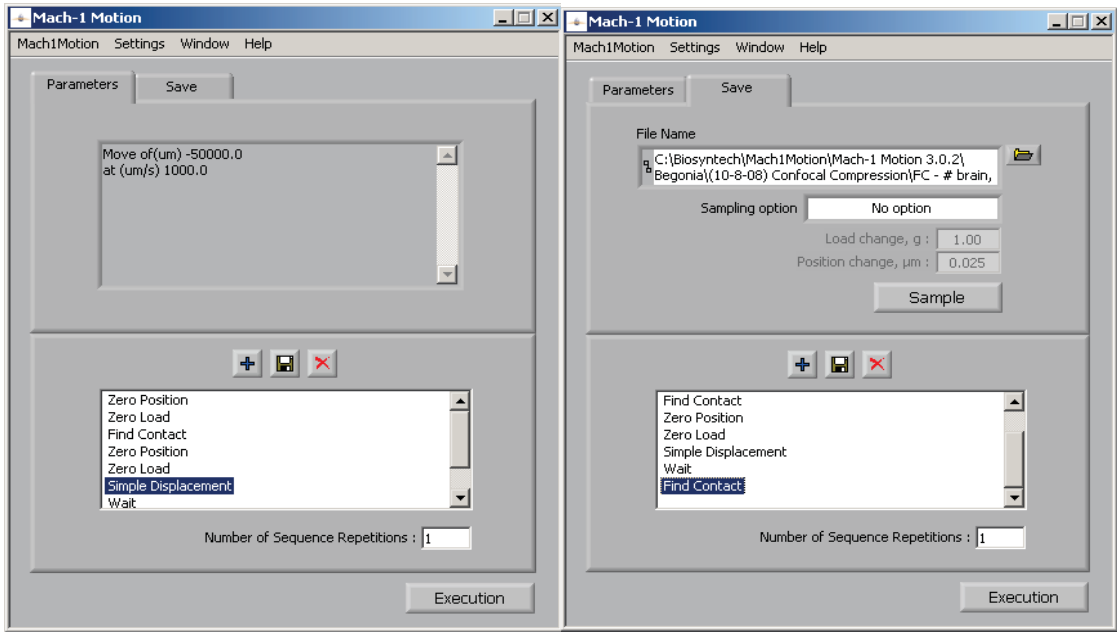

Figure 3.4 (LEFT) Mach-1™ sequence managing window with the parameters tab open for editing program steps. (RIGHT) Mach-1™ sequence managing window with the save tab open for specifying text files to store.

Figure 3.5 exhibits the real-time display and actuator control windows that were utilized for running experiments. The real-time display window monitored the fluctuations in both the vertical position and load while the actuator control window enables manually positioning of the 1 kg load cell prior to testing.

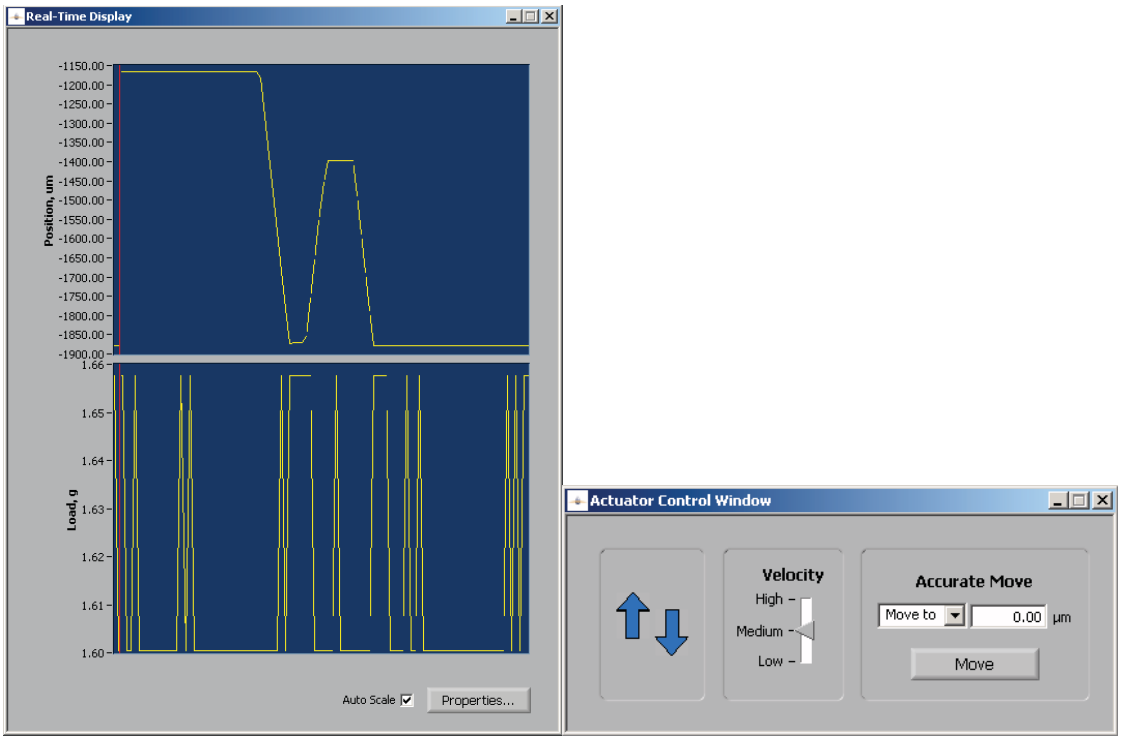

Figure 3.5 (LEFT) Mach-1™ real-time display for monitoring the vertical position and loading capacity. (RIGHT) Mach-1™ actuator control window for allowing manual positioning of the 1 kg load cell.

Attachable stainless steel components were available for the Mach-1™ experimental setup, which included a circular platen with a diameter of 48 mm for unconfined compression and uniaxial tension experiments as well as a base for housing test specimens, which can be seen in Figure 3.6. The inner and outer diameters of the base were 105 mm and 158 mm, respectively, and the height for its fluid capacity was 32 mm.

Figure 3.6 (LEFT) Overhead view of the stainless steel base utilized for housing test specimens for the duration of experiments. (RIGHT) Side view of stainless steel circular platen used in both unconfined compression and uniaxial tension experiments.

Strain Rate Dependency Protocol

Before each unconfined compression test was initiated, two experimental parameters were specified: strain rate and percentage strain level. The strain rates available for selection were 0.10 s^{-1}, 0.025 s^{-1}, and 0.00625 s^{-1}, and the percentage strain levels available for selection were 15%, 30%, and 40%. 0.01 M phosphate buffered saline (PBS) was also prepared to prevent tissue dehydration while 10% neutral buffered formalin (NBF) was prepared to facilitate the eventual confocal imaging of the fixed tissue. To determine the original sample height of each test specimen, the circular platen was programmed to descend until it initiated contact with the upper surface of the tissue. The sensitivity of the actuator was then employed for measuring the original height of the test specimen within µm, which was then used for calculating the

corresponding loading velocity (µm/s) and the strain distance (µm). While the circular platen remained in its stationary vertical position, samples were submerged in 0.01 M PBS at 25°C to simulate the fluid environment that brain tissue is typically surrounded, which can be seen in Figure 3.7.

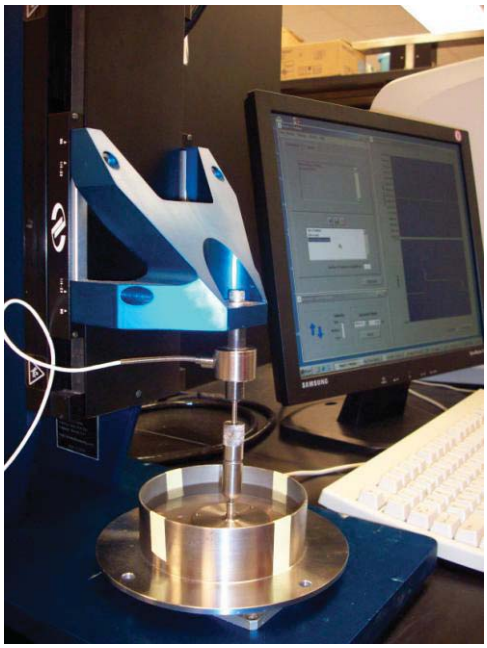

Figure 3.7 Experiment with the test specimen submerged in 0.01 M PBS immediately after the determination of its initial height within µm.

As shown in Figure 3.8, an automated pipette (IBS Integra Biosciences PIPETBOY, acu) was utilized for siphoning the 0.01 M PBS and replacing it with a preliminary batch of 10% NBF to fix the test specimen in its compressed state once an individual experiment was completed. Figure 3.8 also illustrates the custom designed polycarbonate (McMaster-Carr, Atlanta, GA) cover pieces that were positioned over the stainless steel base component to limit exposure of 10% NBF to the atmosphere. Before

proceeding to the next experiment, the fixed specimen from the preceding experiment was transferred to a separate storage container filled with a fresh batch of 10% NBF.

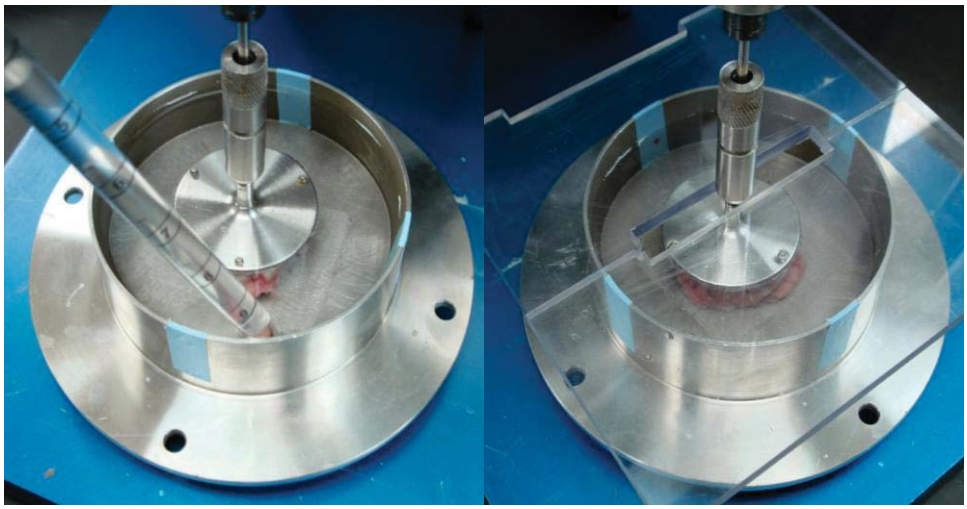

Figure 3.8 (LEFT) Replacement of 0.01 M PBS following the completion of an individual unconfined compression experiment. (RIGHT) Covering of Mach-1^{TM} experimental setup with customized polycarbonate pieces to reduce exposure of 10% NBF to the atmosphere.

Stress-State Dependency Protocol

All unconfined compression experiments were performed identically to the procedure outlined in the strain rate dependency protocol with the exception that the strain rate and percentage strain level were held constant for all tests at 0.10 s^{-1} and 40%, respectively. In addition, 10% NBF was utilized upon completion of each experiment under all 3 testing modes to facilitate confocal imaging and microstructural analysis.

Before uniaxial tension experiments could be performed, Permabond 240 high viscosity adhesive (Ellsworth Adhesives, Germantown, WI) was applied to the upper and

lower surface of cylindrical test specimens. The original height of each test specimen was determined when the circular platen initiated contact with the upper surface of the tissue, and the corresponding loading velocity (µm/s) and the strain distance (µm) were then calculated. Once proper adhesion was confirmed between the tissue surfaces and both the circular platen and the stainless steel base, uniaxial tension experiments were completed to 40% strain at a strain rate of 0.10 s^{-1}.

For the fixed-end shear experiments, custom components were designed using 3-D CAD software (SolidWorks Corporation, Concord, MA) and fabricated according to the specifications shown in Figure 3.9.

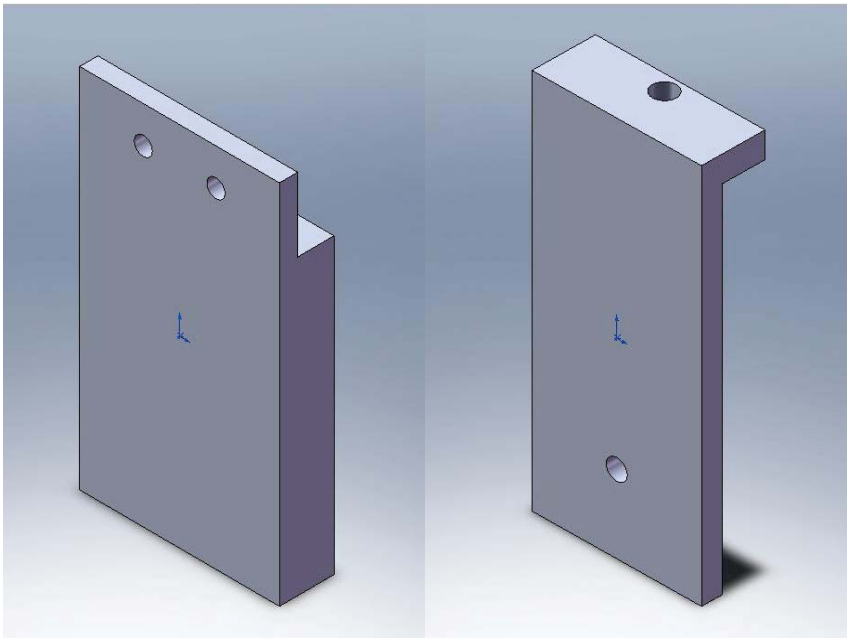

Figure 3.9 (LEFT) Customized aluminum shear platen designed to be attached to the 1 kg load cell on the Mach-1™ testing system with two #6 - 32 x 1/2 USS socket head cap screws and secured with two #6 - 32 hex nuts. (RIGHT) Customized aluminum L-shaped component designed to be bolted into a test stand with one M6 x 1.0 x 10 Phillips Pan Head machine screw.

Prior to the execution of fixed-end shear experiments, Permabond 240 high viscosity adhesive was utilized for stabilizing each test specimen onto the L-shaped component, which was eventually mounted onto the mobile test stand once the adhesive had dried sufficiently. With the rectangular test specimen stabilized, adhesive was applied to both the exposed tissue surface and the shear platen, and the adjustable knob on the mobile test stand was used to manually align the test specimen with the corresponding shear platen attached to the 1 kg load cell, as seen in Figure 3.10. When the interface between the tissue surfaces and the shear components was confirmed, fixed-end shear experiments were conducted to 40% strain at a strain rate of 0.10 s^{-1}.

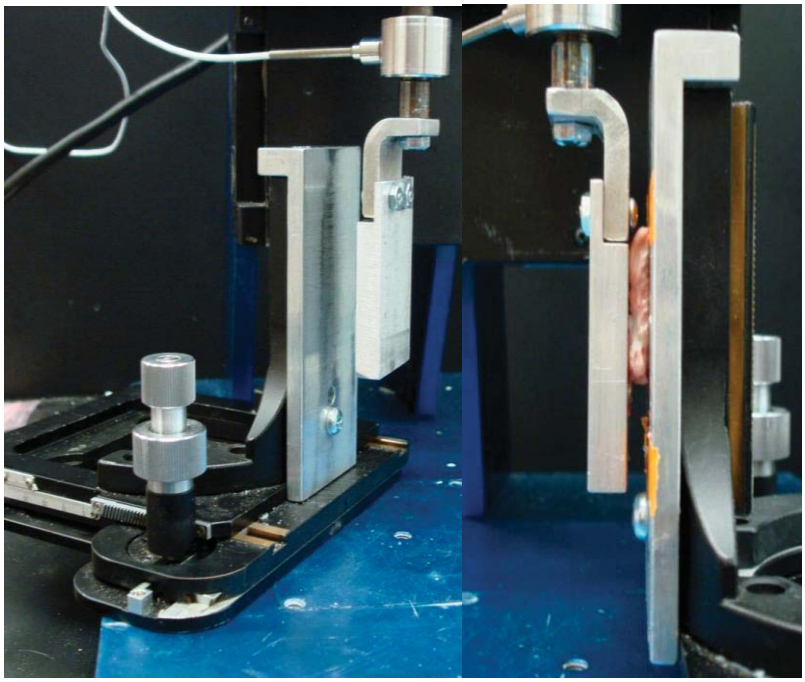

Figure 3.10 (LEFT) Customized aluminum shear platen designed to be attached to the 1 kg load cell on the Mach-1™ testing system. (RIGHT) Customized aluminum piece designed to be bolted into a mobile test stand.

Histology

Test specimens were removed from the 10% NBF within seven to ten days following their initial immersion. In general, test specimens from unconfined compression experiments maintained their cylindrical geometry regardless of the specified strain rate and percentage strain level. As seen in Figures 3.11, coronal sections of brain material were continually excised from the central region of the compressed tissue surface, which was assumed to experience the highest percentage of force from the circular platen. As shown in Figure 3.11, thin rectangular sections were excised from the upper region of the coronal sections, which were expected to encompass the impact site and were distinguishable by sulci and gyri.

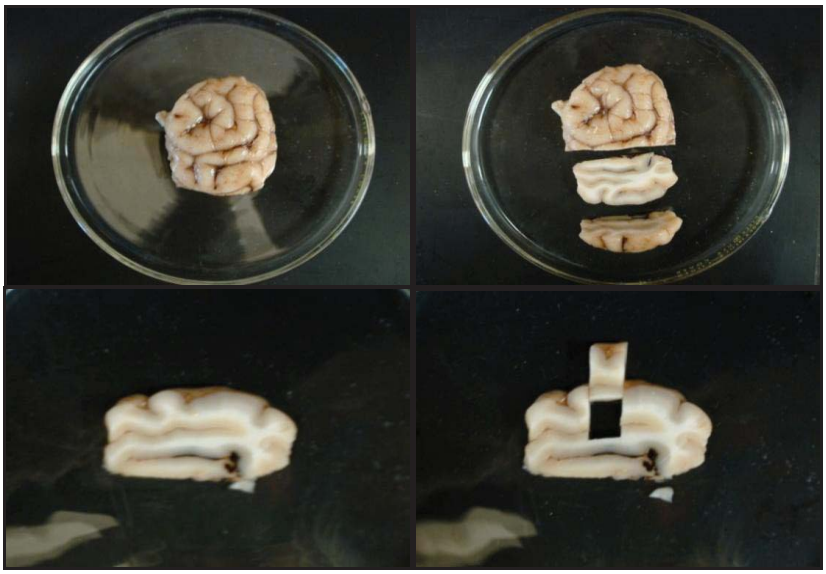

Figure 3.11 (TOP-LEFT), (TOP-RIGHT) Overhead view of fixed test specimen with sustained cylindrical configuration despite immersion in 10% NBF after completion of compression experiments. (BOTTOM-LEFT) Sagittal view of a coronal section excised from central portion of fixed test specimen with the upper surface distinguished by the sulci and gyri. (BOTTOM-RIGHT) Rectangular section excised from the upper region of the coronal section.

All porcine sections were eventually subjected to histological processing prior to fluorescent staining (Electron Microscopy Center, Mississippi State University). After being rinsed in distilled water and dehydrated in a graded ethanol series, sections were infiltrated and embedded in Paraplast Plus (Oxford Labware, St. Louis, MO) using CitriSolve (Fisher Scientific, Houston, TX) as a transitional fluid. Multiple 5 µm sections were cut using an American Optical 820 rotary microtome (Fisher Scientific, Houston, TX) and mounted onto microscope slides for future staining and imaging.

Fluorescent Staining and Confocal Microscopy

Slides were deparaffinized using CitriSolve and a graded ethanol series before fluorescent staining could be performed. The two selected fluorescent stains were then individually applied according to their corresponding biological components. The Fluoromyelin™ Fluorescent Myelin Stain targeted the myelinated region throughout the neural matrix while the NeuroTrace™ Fluorescent Nissl Stain (Invitrogen Corporation, CA) targeted neuron cell bodies. The different channels of the ZEISS LSM 510 confocal laser scanning microscope (Carl Zeiss Microimaging, NY) were used to visualize the disruption within the myelin fiber network and dispersion of neuron cell bodies at 20x magnification, as seen in Figure 3.12.

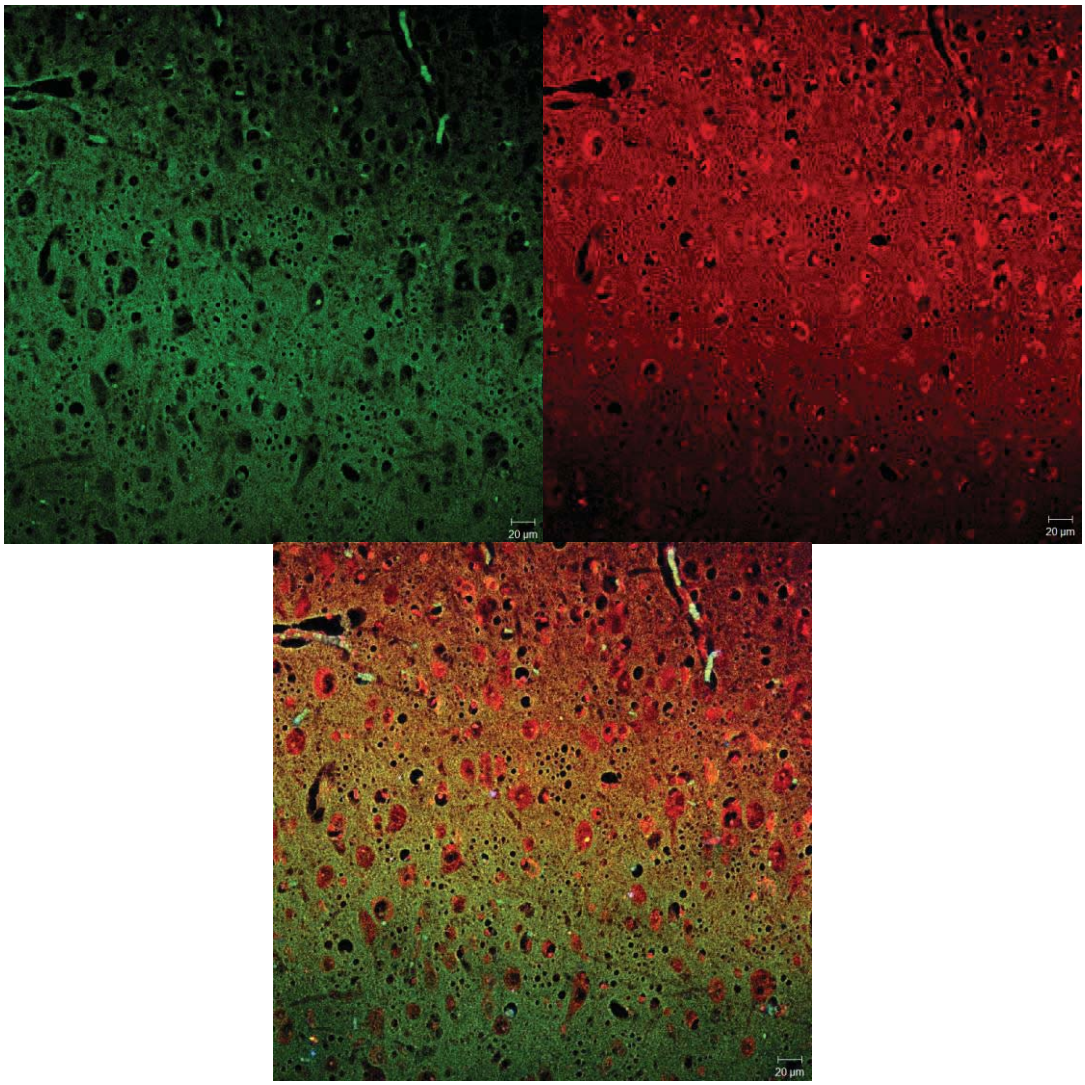

Figure 3.12 (TOP-LEFT) Image of Fluoromyelin™ Fluorescent Myelin Stain fluorescing green at 20x magnification. (TOP-RIGHT) Image of NeuroTrace™ Fluorescent Nissl Stain fluorescing red at 20x magnification. (BOTTOM) Image of both stains fluorescing simultaneously at 20x magnification.

Microstructural Analysis

ImageJ (National Institute of Health, MD) was the preliminary analysis software utilized for quantifying the microstructural damage that occurred at different strain rates and percentage strain levels. Each confocal image was isolated to either the

NeuroTrace™ channel or the Fluoromyelin™ channel before being converted to an 8-bit binary file, which is shown in Figure 3.13.

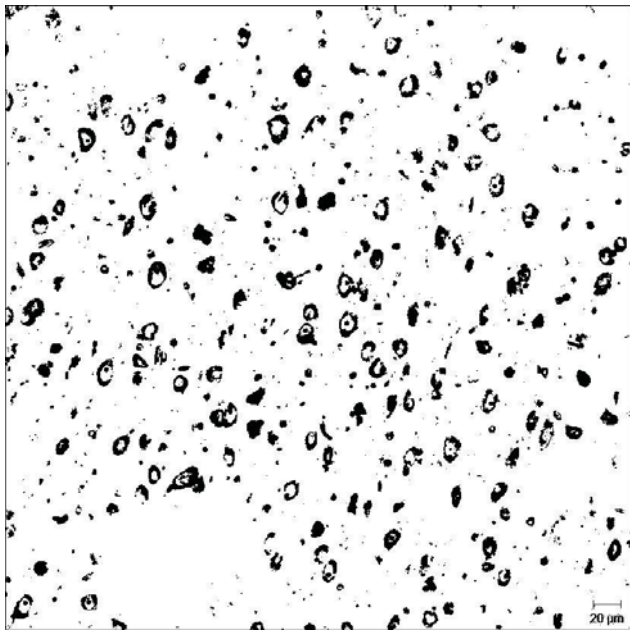

Figure 3.13 Binary image created after an original image into an 8-bit file and using both the THRESHOLD and REMOVE OUTLIERS commands to reduce noise.

After the THRESHOLD and REMOVE OUTLIERS commands were used to eliminate visual noise, the ANALYZE PARTICLES command was utilized for outputting results and summary files that compiled a listing of visual parameters useful for quantifying the progressive microstructural damage, which can be seen in Figure 3.14. The parameters provided by a typical analysis were COUNT, TOTAL AREA, and AVERAGE SIZE, which were all utilized to determine the AREA FRACTION corresponding to the dispersal of neuron cell bodies.

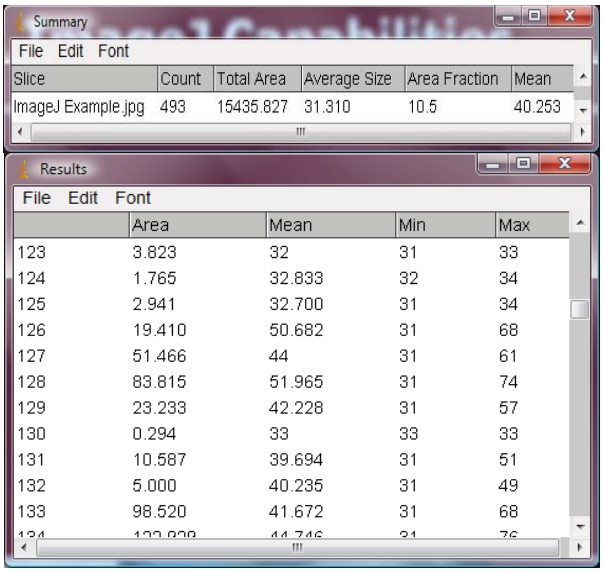

Figure 3.14 Summary and results windows for displaying various parameters.

Image Analyzer v.2.2-0 (Center for Advanced Vehicular Systems, Mississippi State University) was eventually utilized to conduct further microstructural analysis since the outputted parameters were more capable of being integrated into potential modeling applications. The parameters provided by this analysis software included AREA, OBJECT COUNT, NUMBER DENSITY, AREA FRACTION, MEAN AREA, and MEAN NND (nearest neighbor distance). NUMBER DENSITY was equal to the OBJECT COUNT divided by the AREA while MEAN AREA represented the average area of each element recognized and highlighted by the software. In addition, MEAN NND corresponded to average distance between neighboring elements within an analyzed image.

Confocal images uploaded into Image Analyzer v.2.2-0 were initially assigned with the RGB component configuration, which was switched to red, green, or grayscale depending on the resolution. Before the microstructural analysis could proceed, the

number of microns and pixels were identified for the scale bar parameters. In addition, the minimum object area and threshold range were specified, and the resulting window displayed both the original and analyzed images along with the associated visual parameters, as shown in Figure 3.15.

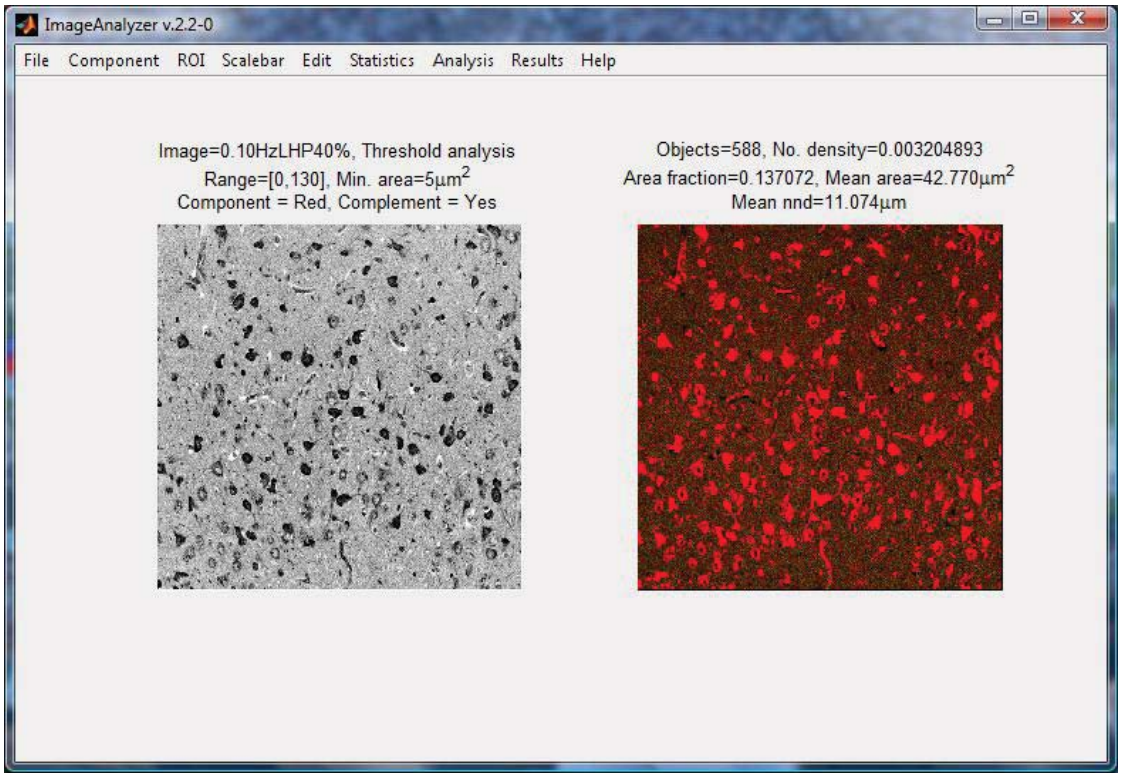

Figure 3.15 Double window displaying the original and analyzed image along with the corresponding microstructural analysis parameters.

CHAPTER IV

RESULTS

Data Processing

Mach-1™ data initially consisted of text files with values for time (s), vertical position (μm), and load (g) but were eventually converted to values for stress (Pa) and strain (μm/ μm). While the procedure was similar for both unconfined compression and uniaxial tension data, the fixed-end shear data was modified using the following equations for Von Mises stress (4-1) and Von Mises strain (4-2):

$$\sigma_e = \frac{1}{\sqrt{2}}\left[(\sigma_x - \sigma_y)^2 + (\sigma_y - \sigma_z)^2 + (\sigma_z - \sigma_x)^2 + 6\left(\tau_{xy}^{\,2} + \tau_{yz}^{\,2} + \tau_{zx}^{\,2}\right)\right]^{\frac{1}{2}} \tag{4-1}$$

$$d\varepsilon_p = \frac{\sqrt{2}}{3}\left[\begin{array}{l}\left(d\varepsilon_x^{\,p} - d\varepsilon_y^{\,p}\right)^2 + \left(d\varepsilon_y^{\,p} - d\varepsilon_z^{\,p}\right)^2 + \left(d\varepsilon_z^{\,p} - d\varepsilon_x^{\,p}\right)^2 + 6\left(d\varepsilon_{xy}^{\,p}\right)^2 \ldots \\ + 6\left(d\varepsilon_{yz}^{\,p}\right)^2 + 6\left(d\varepsilon_{zx}^{\,p}\right)^2\end{array}\right]^{\frac{1}{2}} \tag{4-2}$$

In general, structure-property relationships were formed by merging experimental data with microstructural analysis in order to provide a more comprehensive depiction of porcine tissue behavior under varying testing conditions. While the mechanical data primarily consisted of stress-strain plots, the microstructural damage assessment included representative confocal images at progressive strain levels

and tabulated parameters obtained from Image Analyzer v2.2-0, a graphical user interface (GUI).

The numbers obtained from the GUI were utilized for measuring the dispersal of biological constituents such as neurons and glial cells, which were identified as red particles within the converted grayscale images. The analyzed parameters were the area (μm^2), object count, number density (cells/mm^2), area fraction (%) (total cell area/total image area), mean area of each cell (μm^2), and mean nearest neighbor distance (µm). In summary, the total area incorporated into all GUI calculations was 183469 μm^2 and based on the specifications for both the minimum object area and threshold range. The object count indicated the amount of particles recognized by the GUI while the number density was equal to the object count divided by the total area. In addition, the area fraction specified the percentage distribution of detected particles while the mean nearest neighbor distance (NND) corresponded to the average distance between neighboring particles.

Microstructural Analysis from Strain Rate Dependency Protocol

Overall, test specimens selected for confocal imaging were extracted from the posterior section of the left hemisphere to reduce the influence of regional variability. Figure 4.1 shows a confocal image of undamaged tissue stained with Fluoromyelin™ Fluorescent Myelin Stain and NeuroTrace™ Fluorescent Nissl Stain (Invitrogen Corporation, CA). The neuron cell bodies and glial cells are depicted as spherical or elliptical red structures that are distributed throughout the neural tissue matrix, which

appears light green. In addition, black voids are present within the network and can be attributed to the inhomogenous composition of the tissue.

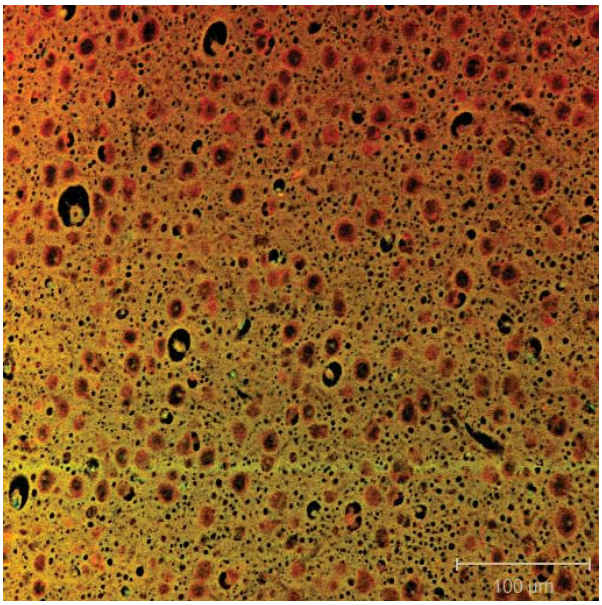

Testing Conditions	Object Count	Number Density (cells/mm^2)	Area Fraction (%)	Mean Area (µm^2)	Mean NND (µm)
Control	188 ± 51	1027 ± 281	5.09697 ± 0.0578	51.62205 ± 14.6988	18.3938 ± 2.5570

Figure 4.1 (TOP) Confocal image at 20x magnification that exhibit the initial distribution of biological constituents for the undamaged state. (BOTTOM) Tabulated analysis parameters for characterizing the dispersion of neurons and glial cells.

Figures 4.2, 4.3, and 4.4 show structure-property relationships in which stress-strain data obtained from the strain rate dependency protocol were supplemented with confocal images captured at strain levels of 15%, 30%, and 40%. GUI analysis parameters are also shown for quantifying the damage evolution at advancing strain levels.

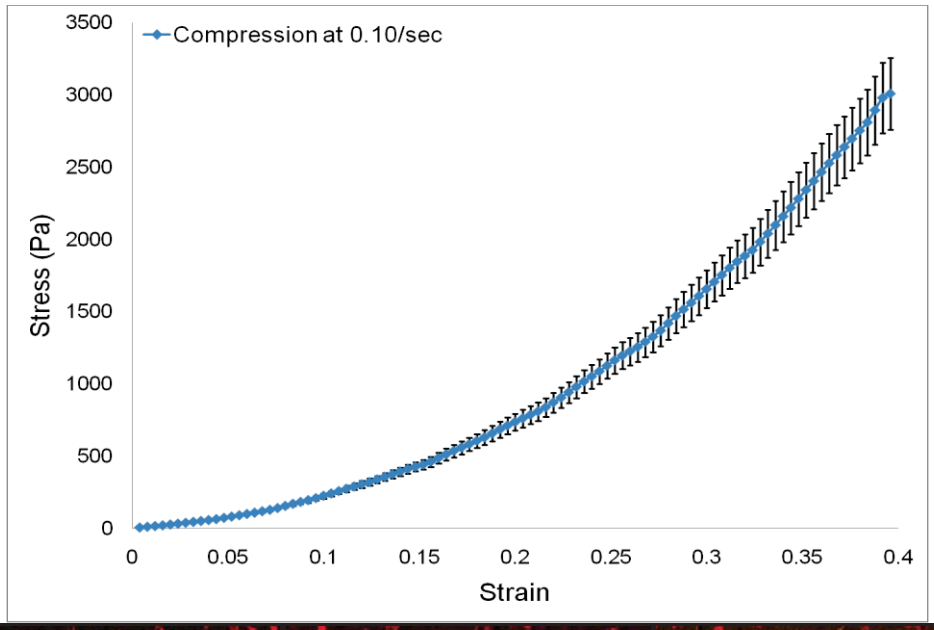

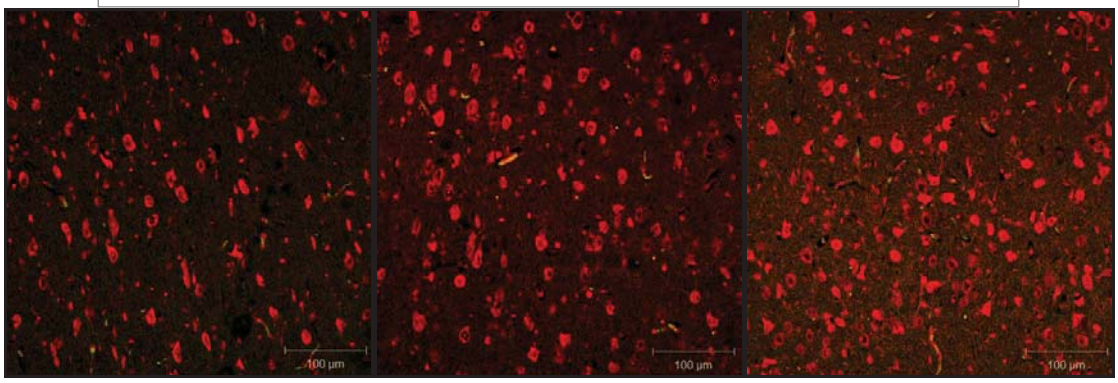

15% strain **30% strain** **40% strain**

Testing Conditions	Object Count	Number Density (cells/mm^2)	Area Fraction (%)	Mean Area (μm^2)	Mean NND (μm)
Compression (0.10/sec, 15%)	406 ± 35	2212 ± 192	8.98322 ± 0.2576	41.0583 ± 5.0823	12.65845 ± 0.9964
Compression (0.10/sec, 30%)	508 ± 17	2771 ± 96	10.3668 ± 0.5030	37.69055 ± 3.4457	10.84965 ± 0.6128
Compression (0.10/sec, 40%)	902 ± 43	4916 ± 238	17.3084 ± 0.2516	35.25955 ± 2.2252	8.69233 ± 0.0047

Figure 4.2 Structure-property relationship for porcine brain tissue under unconfined compression at 0.10 s^{-1}. (TOP) Stress-strain data with error bars representing standard deviations. (MIDDLE) Confocal images at 20x magnification that exhibit neuron and glial cell dispersal for strain levels of 15%, 30%, and 40%. (BOTTOM) Tabulated analysis parameters for quantifying the damage progression at 0.10 s^{-1}.

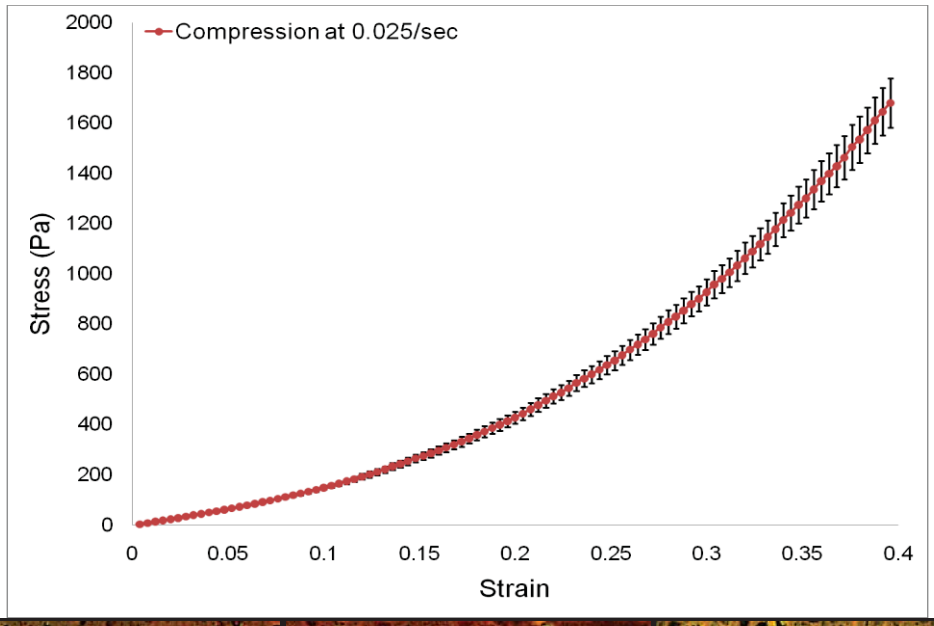

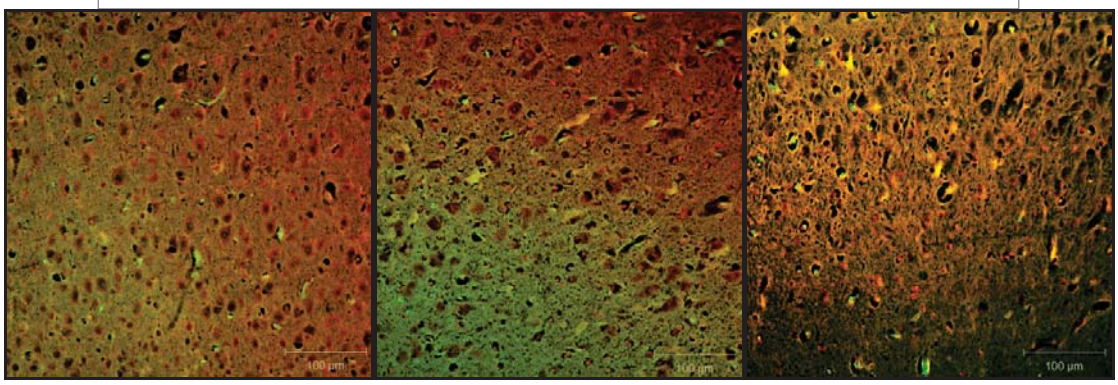

15% strain **30% strain** **40% strain**

Testing Conditions	Object Count	Number Density (cells/mm^2)	Area Fraction (%)	Mean Area (μm^2)	Mean NND (μm)
Compression (0.025/sec, 15%)	348 ± 13	1899 ± 192	5.52955 ± 1.1635	47.628 ± 19.1626	16.0678 ± 4.2896
Compression (0.025/sec, 30%)	360 ± 22	1964 ± 38	6.69697 ± 0.7589	58.5281 ± 30.7802	14.7362 ± 1.8283
Compression (0.025/sec, 40%)	529 ± 72	2883 ± 393	7.8845 ± 0.7224	52.612 ± 9.9589	14.4705 ± 2.4063

Figure 4.3 Structure-property relationship for porcine brain tissue under unconfined compression at 0.025 s^{-1}. (TOP) Stress-strain data with error bars representing standard deviations. (MIDDLE) Confocal images at 20x magnification that exhibit neuron and glial cell dispersal for strain levels of 15%, 30%, and 40%. (BOTTOM) Tabulated analysis parameters for quantifying the damage progression at 0.025 s^{-1}.

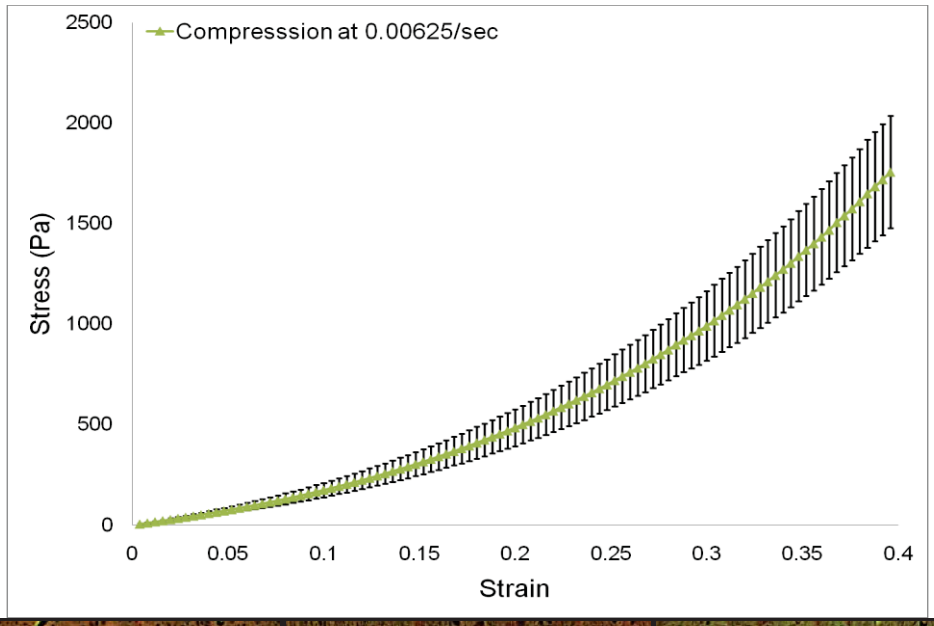

15% strain **30% strain** **40% strain**

Testing Conditions	Object Count	Number Density (cells/mm^2)	Area Fraction (%)	Mean Area (μm^2)	Mean NND (μm)
Compression (0.00625/sec, 15%)	201 ± 26	1095 ± 146	4.825725 ± 1.5623	69.57265 ± 13.8442	22.158 ± 3.9428
Compression (0.00625/sec, 30%)	241 ± 38	1313 ± 208	5.487215 ± 1.4565	66.9563 ± 15.6733	19.70575 ± 3.9884
Compression (0.00625/sec, 40%)	310 ± 34	1692 ± 188	6.867765 ± 1.0035	67.43235 ± 26.6207	18.03585 ± 4.2146

Figure 4.4 Structure-property relationship for porcine brain tissue under unconfined compression at 0.00625 s^{-1}. (TOP) Stress-strain data with error bars representing standard deviations. (MIDDLE) Confocal images at 20x magnification that exhibit neuron and glial cell dispersal for strain levels of 15%, 30%, and 40%. (BOTTOM) Tabulated analysis parameters for quantifying the damage progression at 0.00625 s^{-1}.

In the stress-strain data of Figures 4.2, 4.3, and 4.4, viscoelastic behavior is evident with the distinctive upward concavity typical of biological tissues undergoing compression. In addition, GUI parameters such as the object count, number density, and area fraction exhibit increasing trends with rising strain level while the mean nearest neighbor distance (NND) demonstrates a decreasing trend with advancing strain level. The GUI parameters shown in Figure 4.4, for example, illustrate object counts of 201 ± 26, 241 ± 38, and 310 ± 34 that correspond to progressive strain levels of 15%, 30%, and 40%, respectively. The object count represents the total number of cells detected by the software and can be attributed to the incremental compaction of the biological constituents within the neural tissue matrix. In addition, the area fraction (%) quantifies the distribution of neurons and glial cells and reveals an increasing trend with values of 4.83 ± 1.56, 5.49 ± 1.46, and 6.87 ± 1.00 for advancing strain levels of 15%, 30%, and 40%, respectively. As for the mean NND (μm), corresponding to the distance between adjacent particles, a decreasing relation is observed with values of 22.16 ± 3.94, 19.7 ± 3.99, and 18.04 ± 4.21 for respective strain levels of 15%, 30%, and 40%.

Based on the data compiled from Figures 4.2, 4.3, and 4.4, an overall structure-property relationship was generated for investigating strain rate dependence, as shown in Figure 4.5, which demonstrates similar trends in the GUI parameters for a strain level of 40% despite varying strain rates. For instance, the area fraction (%) steadily progresses with values of 6.87 ± 1.00, 7.88 ± 0.72, and 17.31 ± 0.25 as the strain rate rises. As for the mean NND, a descending relation is revealed with values of 18.04 ± 4.21, 14.47 ± 2.41, and 8.69 ± 0.01 as the strain rate increases.

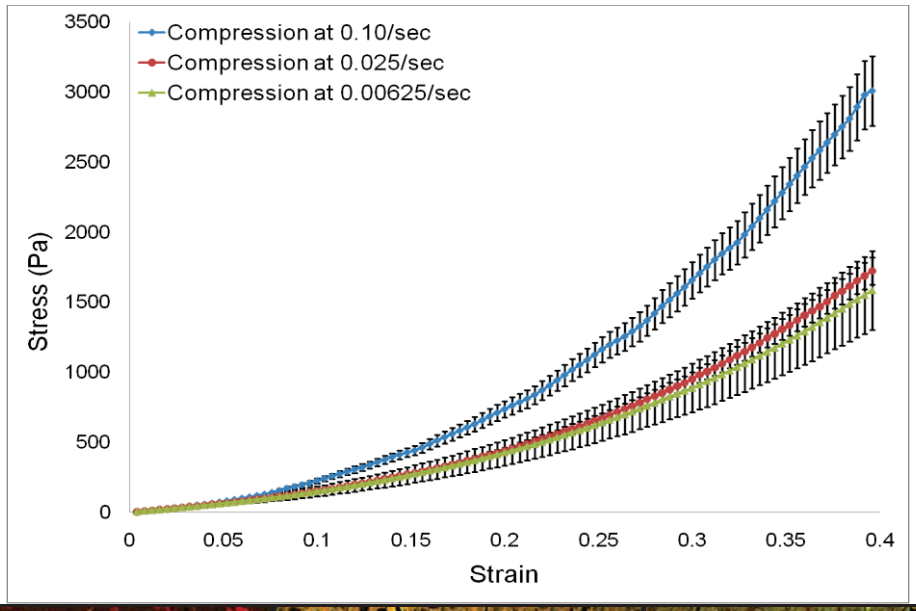

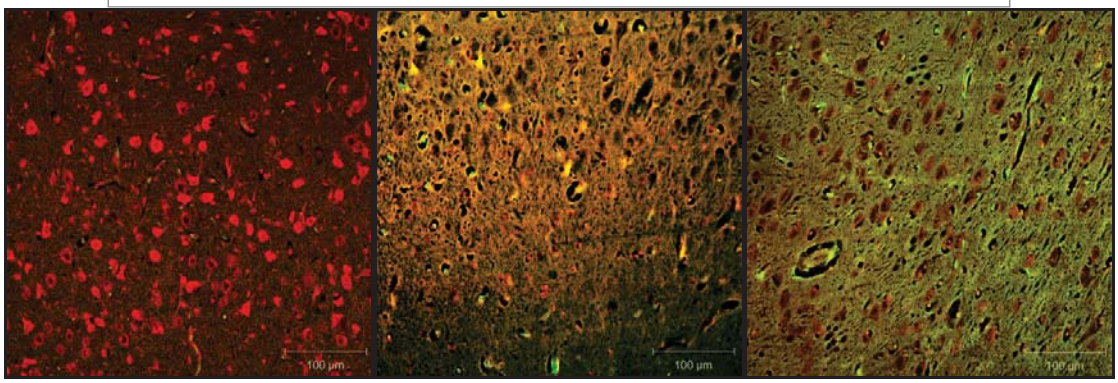

0.10 s^{-1}, 40% **0.025 s^{-1}, 40%** **0.00625 s^{-1}, 40%**

Testing Conditions	Object Count	Number Density (cells/mm^2)	Area Fraction (%)	Mean Area (µm^2)	Mean NND (µm)
Compression (0.10/sec, 40%)	902 ± 43	4916 ± 238	17.3084 ± 0.2516	35.25955 ± 2.2252	8.69233 ± 0.0047
Compression (0.025/sec, 40%)	529 ± 72	2883 ± 393	7.8845 ± 0.7224	52.612 ± 9.9589	14.4705 ± 2.4063
Compression (0.00625/sec, 40%)	310 ± 34	1692 ± 188	6.867765 ± 1.0035	67.43235 ± 26.6207	18.03585 ± 4.2146

Figure 4.5 Structure-property relationship depicting the strain rate dependence of porcine brain tissue. (TOP) Stress-strain data with error bars representing standard deviations. (MIDDLE) Confocal images at 20x magnification that exhibit neuron and glial cell dispersal for strain rates of 0.10 s^{-1}, 0.025 s^{-1}, and 0.00625 s^{-1} at a strain level of 40%. (BOTTOM) Tabulated analysis parameters for comparing the degree of microstructural damage among the different strain rates at 40% strain.

Microstructural Analysis from Stress-State Dependency Protocol

Additional structure-property relationships were produced from the stress-state dependency protocol by integrating stress-strain data, confocal images, and GUI parameters from various testing modes on 61 total test specimens. 16 unconfined compression tests were completed at a strain rate of 0.10 s^{-1} and strain level of 40%, as shown in Figure 4.2. Meanwhile, Figure 4.6 exhibits the structure-property relationship formed by combining mechanical data from 20 uniaxial tension experiments with corresponding confocal images and GUI parameters. In addition, Figure 4.7 illustrates the structure-property relationship derived by incorporating stress-strain data from 25 fixed-end shear experiments with a similar microstructural damage assessment.

The tensile behavior shown in Figure 4.6 is comparable to prior tension testing on porcine brain tissue seen in literature, where the resulting stress-strain data illustrated distinctive downward concavity (Miller, 2002). In the confocal analysis, the distribution of neurons and glial cells revealed signs of directional orientation in which the biological constituents were moderately aligned in sections of the neural tissue matrix. This configuration of biological constituents varies substantially from the more compact arrangement seen in porcine test specimens under compression. However, the microstructural organization of the tensile samples coincides with the confocal images in Figure 4.7 since the neuron and glial cell distribution also demonstrates minimal directional orientation. This general behavior could be attributed to the nature of the applied stresses since the tensile and shear forces inevitably extends the tissue matrix causing its constituents to gradually align with the tightly stretched regions.

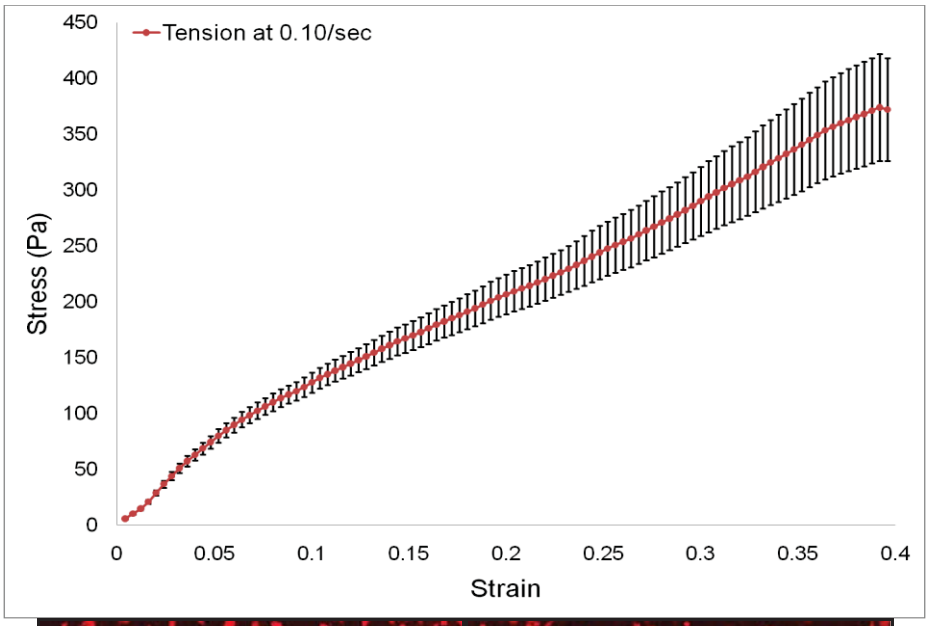

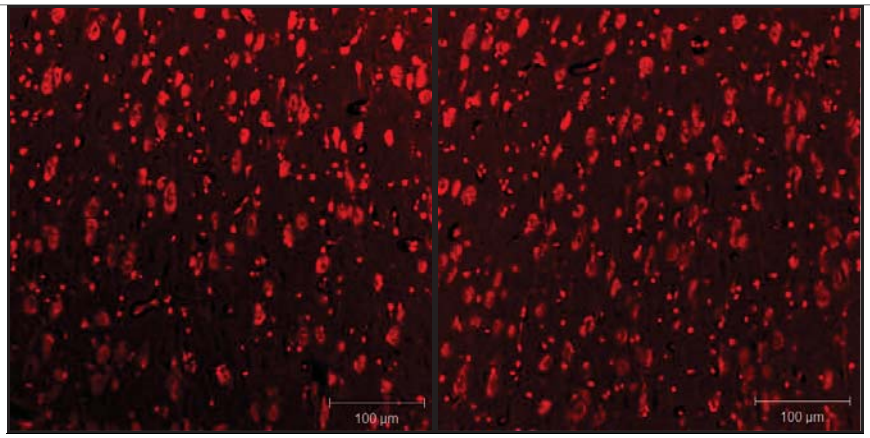

Testing Conditions	Object Count	Number Density (cells/mm^2)	Area Fraction (%)	Mean Area (µm^2)	Mean NND (µm)
Tension (0.10/sec, 40%)	408 ± 31	2226 ± 173	10.64835 ± 0.0511	47.97935 ± 3.9669	12.904 ± 0.5713

Figure 4.6 Structure-property relationship depicting the tensile behavior of porcine brain tissue. (TOP) Stress-strain data with error bars representing standard deviations. (MIDDLE) Confocal images at 20x magnification that exhibit neuron and glial cell dispersal for uniaxial tension at a strain rate and strain level of 0.10 s^{-1} and 40%, respectively. (BOTTOM) Tabulated analysis parameters for assessing the microstructural damage occurring at 40% strain.

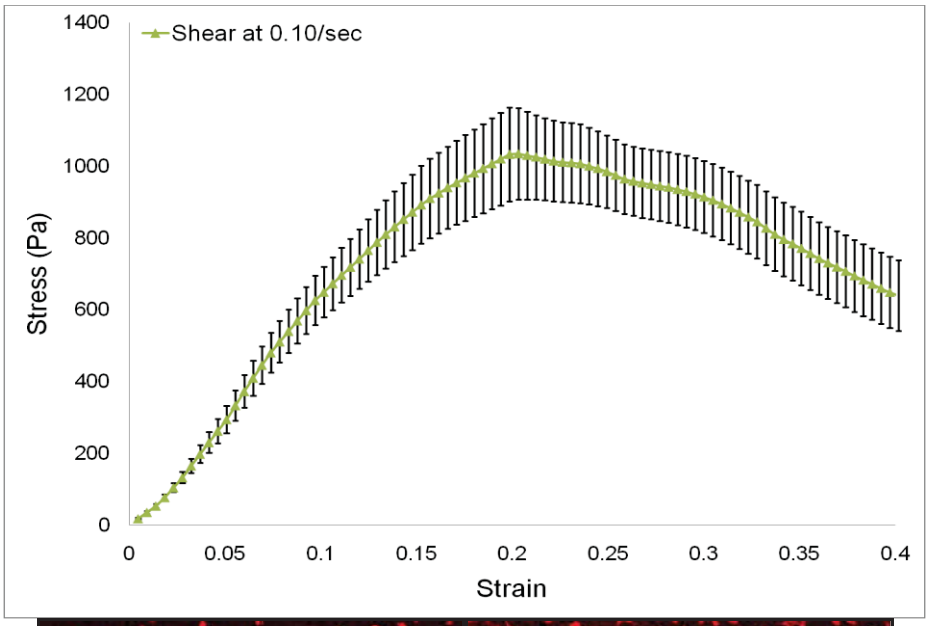

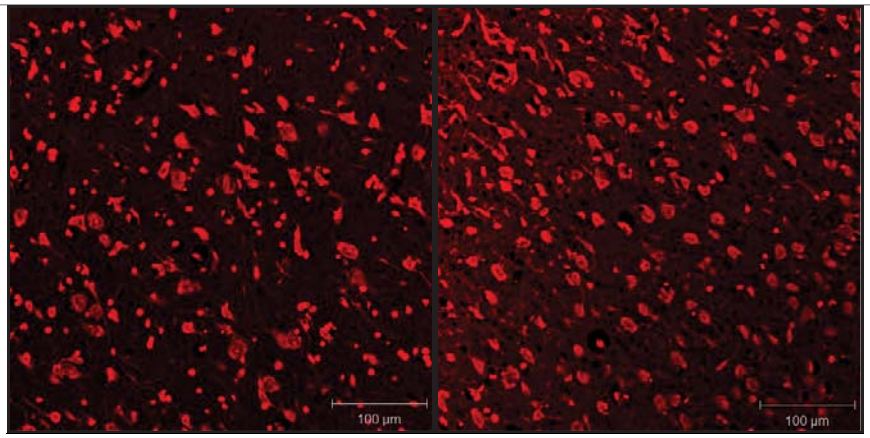

Testing Conditions	Object Count	Number Density (cells/mm^2)	Area Fraction (%)	Mean Area (µm^2)	Mean NND (µm)
Shear (0.10/sec, 40%)	399 ± 25	2174 ± 138	11.1947 ± 0.2372	51.61575 ± 4.3834	12.9778 ± 0.4712

Figure 4.7 Structure-property relationship depicting the shear behavior of porcine brain tissue. (TOP) Stress-strain data with error bars representing standard deviations. (MIDDLE) Confocal images at 20x magnification that exhibit neuron and glial cell dispersal for fixed-end shear at a strain rate and strain level of 0.10 s^{-1} and 40%, respectively. (BOTTOM) Tabulated analysis parameters for assessing the microstructural damage occurring at 40% strain.

As with the strain rate dependency data in Figure 4.5, an overall structure-property relationship was produced for investigating stress-state dependence by compiling data from unconfined compression, uniaxial tension, and fixed-end shear experiments. Figure 4.8 exhibits this structure-property relationship with stress-strain plots depicting the compressive, tensile, and shear behavior of porcine brain tissue for a designated strain rate of 0.10 s^{-1}. A microstructural damage assessment was also performed using confocal and GUI analysis at 40% strain for determining the extent of inelastic behavior with respect to different testing modes. In general, the microstructural damage assessment revealed noticeable changes in compressive GUI parameters when compared to the both tensile and shear GUI parameters. For example, the compressive object count was 902 ± 43 while the tensile and shear object counts were 408 ± 31 and 399 ± 25, respectively. In addition, the compressive area fraction (%) was 17.31 ± 0.25 while the respective tensile and shear area fractions (%) were 10.65 ± 0.05 and 11.19 ± 0.24. While the mean NND (µm) for compression was 8.69 ± 0.01, the mean NND (µm) for tension and shear were 12.90 ± 0.57 and 12.98 ± 0.47, respectively.

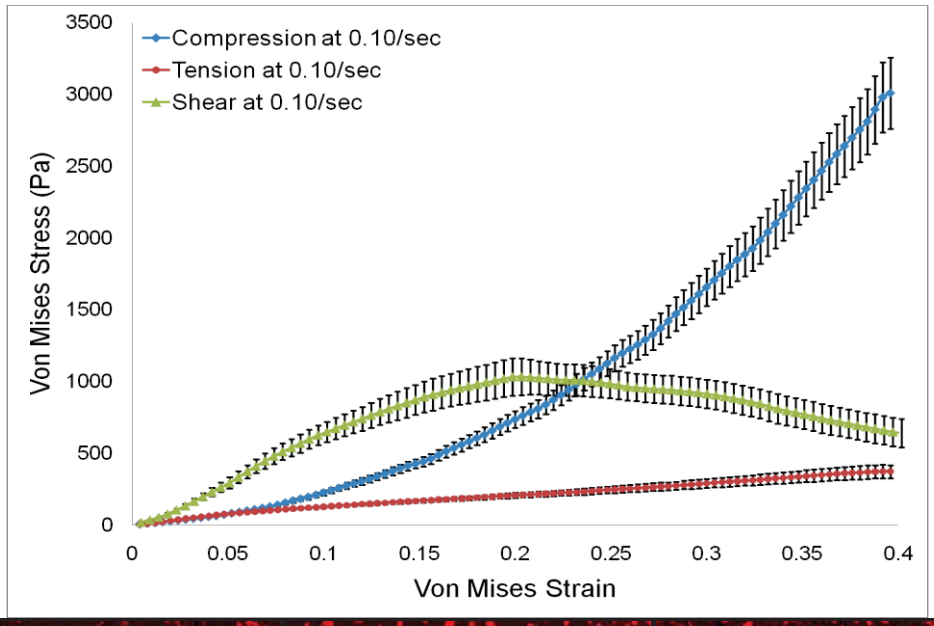

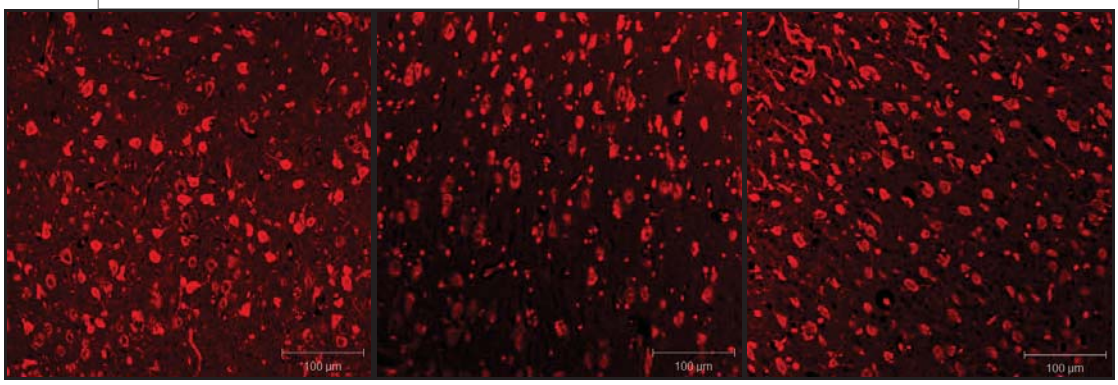

Compression, 40% **Tension, 40%** **Shear, 40%**

Testing Conditions	Object Count	Number Density	Area Fraction	Mean Area (μm^2)	Mean NND (μm)
Compression (0.10/sec, 40%)	902 ± 43	4916 ± 238	17.3084 ± 0.2516	35.25955 ± 2.2252	8.69233 ± 0.0047
Tension (0.10/sec, 40%)	408 ± 31	2226 ± 173	10.64835 ± 0.0511	47.97935 ± 3.9669	12.904 ± 0.5713
Shear (0.10/sec, 40%)	399 ± 25	2174 ± 138	11.1947 ± 0.2372	51.61575 ± 4.3834	12.9778 ± 0.4712

Figure 4.8 Structure-property relationship depicting the stress-state dependence of porcine brain in compression, tension and shear at 0.10 s^{-1} to 40% strain. (TOP) Stress-strain data with error bars representing standard deviations. (MIDDLE) Confocal images at 20x magnification that exhibit neuron and glial cell dispersal for various testing conditions. (BOTTOM) Tabulated analysis parameters for tracking the microstructural damage.

Microstructural Analysis with H&E Stained Images

While the confocal microscope proved to be a vital tool for visualizing the microstructural damage resulting from the fluctuating distribution of biological constituents such as neurons and glial cells, a standard light microscope was also utilized to further investigate the specified testing conditions and to confirm if similar results would be produced. At the College of Veterinary Medicine, slides of porcine tissue sections were obtained from both the strain rate and stress-state dependency protocols and stained with H&E (hematoxylin and eosin). In addition to strain rate, strain level, and testing mode, classifications were also made for white matter or gray matter in the corresponding images, which were examined using Image Analyzer v2.2-0. This microstructural analysis procedure was used to observe the relative influence of white matter versus gray matter since the test specimens procured in all experimental protocols consisted of a heterogeneous mixture of both.

In conjunction with the structure-property relationships previously seen in Figures 4.2, 4.3, and 4.4, the standard light microscope images and associated GUI parameters for each strain rate at progressive strain levels of 15%, 30%, and 40% are displayed in Figures 4.9 through 4.14. The microstructural damage assessments are shown for gray matter in Figures 4.9, 4.10, and 4.11 and for white matter in Figures 4.12, 4.13, and 4.14. The total area for images at 40x magnification is 61224 μm^2while the total area for images at 10x magnification is 3918367 μm^2. As evidenced in the confocal microscopy results, analysis parameters such as object count, number density, and area fraction (%) illustrate an increasing trend with rising strain level while the

mean NND (μm) exhibits a decreasing relation with respect to advancing strain level. Furthermore, these correlations are discernible in gray matter as well as white matter and are also apparent for all three strain rates. For example, at respective strain levels of 15%, 30%, and 40% for a strain rate of 0.10 s^{-1} in gray matter, the values for area fraction (%) are 6.41, 7.22, and 8.40 whereas the values for mean NND (μm) are 10.66, 9.53, and 8.01. Similarly, at an identical strain rate and progressive strain levels in white matter, the values for area fraction (%) are 3.55, 4.12, and 4.56 while the values for mean NND (μm) are 8.81, 8.55, and 7.37.

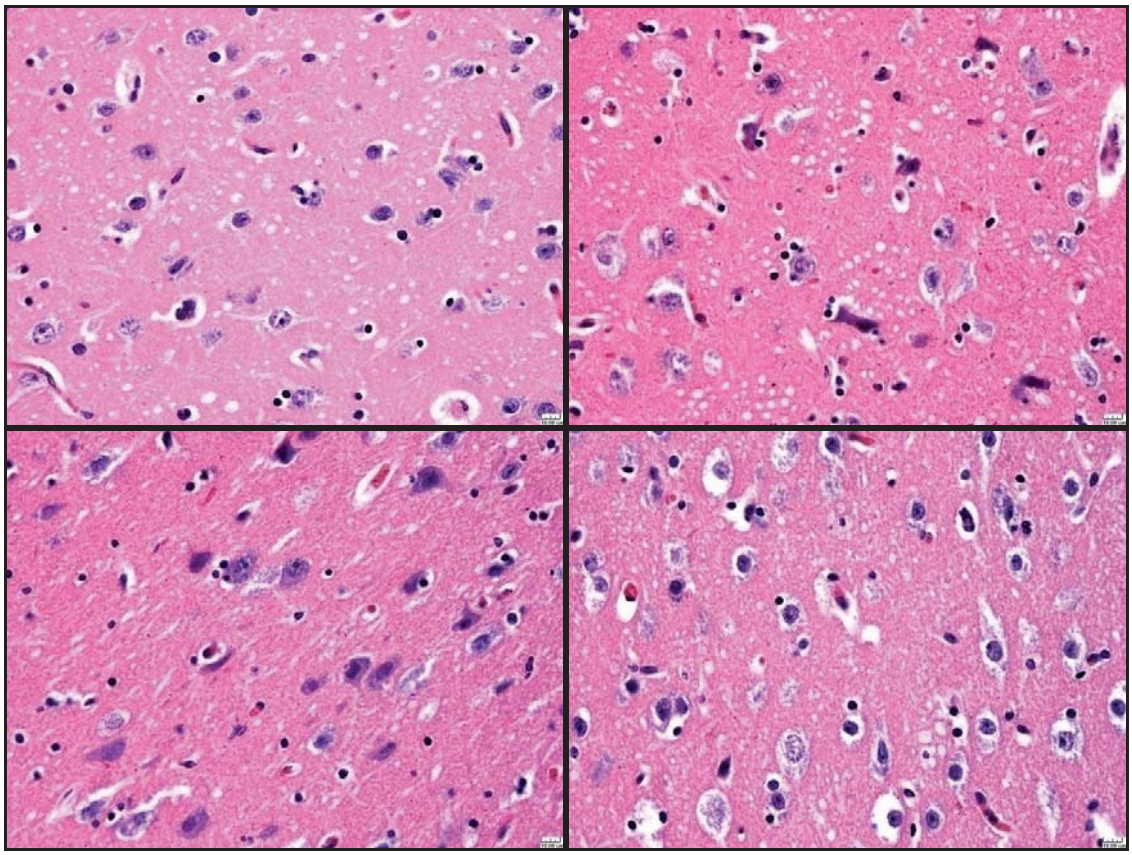

GM Testing Conditions	Object Count	Number Density (cells/mm^2)	Area Fraction (%)	Mean Area (μm^2)	Mean NND (μm)
Compression (0.10/sec, 15%)	149	2433	6.41427	26.3564	10.663
Compression (0.10/sec, 30%)	184	3005	7.21589	24.0103	9.5283
Compression (0.10/sec, 40%)	222	3626	8.40302	23.1744	8.01256

Figure 4.9 Standard light microscope images of H&E stained porcine sections at 40x magnification for unconfined compression at 0.10 s^{-1}. (TOP-LEFT) Undamaged gray matter. (TOP-RIGHT) Gray matter compressed to 15% strain. (BOTTOM-LEFT) Gray matter compressed to 30% strain. (BOTTOM-RIGHT) Gray matter compressed to 40% strain. (BOTTOM) Tabulated analysis parameters for depicting the distribution of various biological constituents.

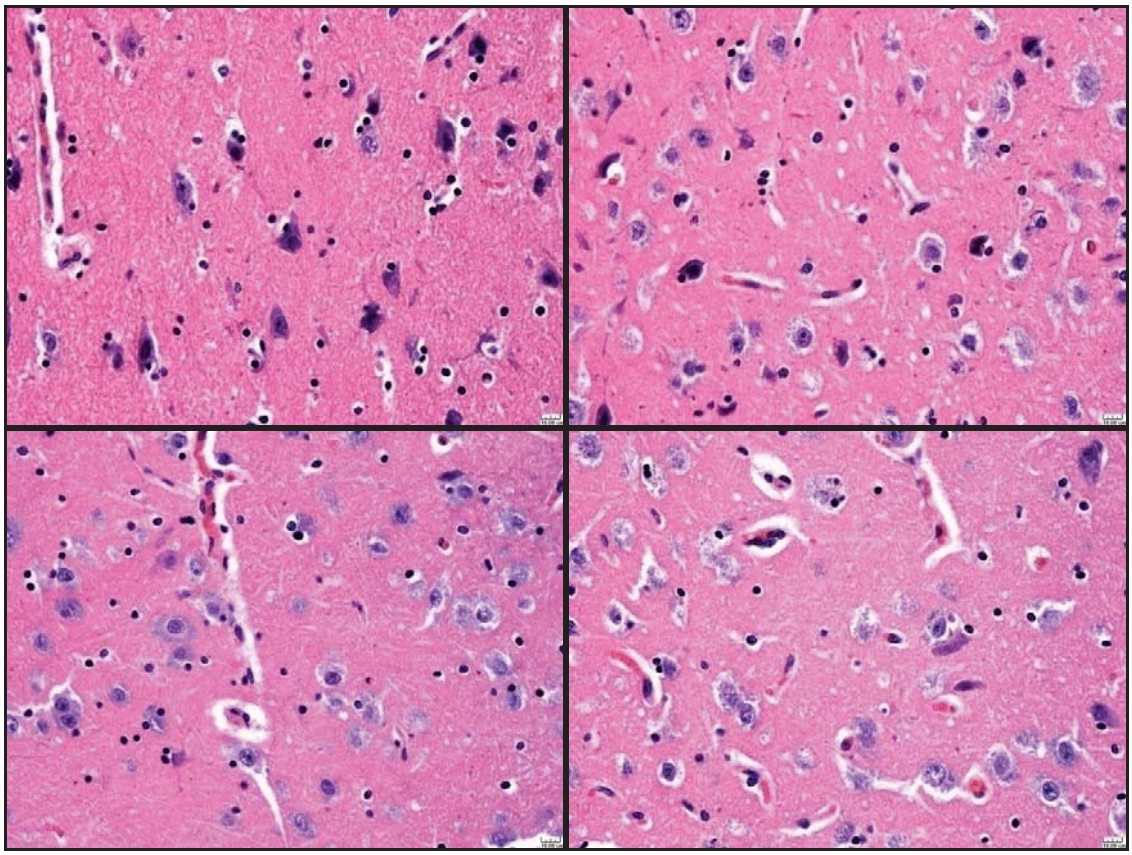

GM Testing Conditions	Object Count	Number Density (cells/mm^2)	Area Fraction (%)	Mean Area (µm^2)	Mean NND (µm)
Compression (0.025/sec, 15%)	122	1992	5.92177	29.7178	12.6363
Compression (0.025/sec, 30%)	154	2515	6.67286	26.5287	11.2778
Compression (0.025/sec, 40%)	157	2564	7.32562	28.5674	11.0042

Figure 4.10 Standard light microscope images of H&E stained porcine sections at 40x magnification for unconfined compression at 0.025 s^{-1}. (TOP-LEFT) Undamaged gray matter. (TOP-RIGHT) Gray matter compressed to 15% strain. (BOTTOM-LEFT) Gray matter compressed to 30% strain. (BOTTOM-RIGHT) Gray matter compressed to 40% strain. (BOTTOM) Tabulated analysis parameters for depicting the distribution of various biological constituents.

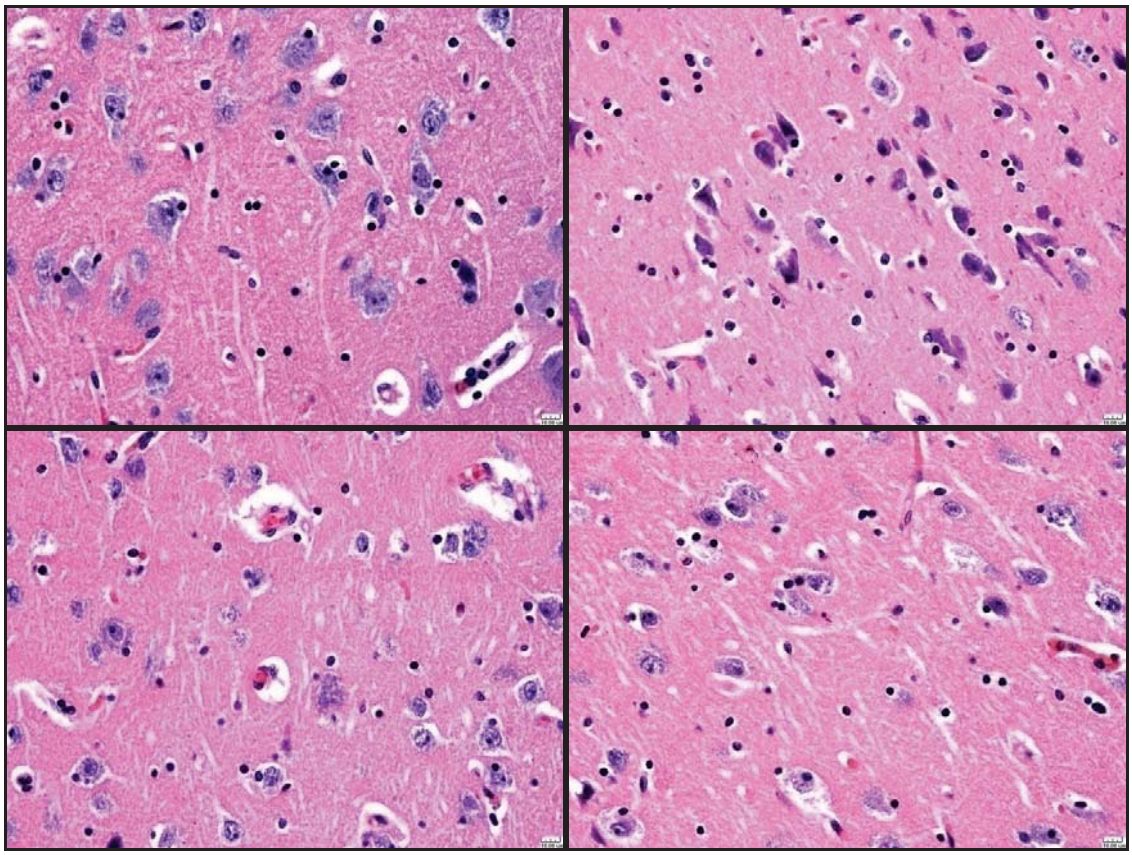

GM Testing Conditions	Object Count	Number Density (cells/mm^2)	Area Fraction (%)	Mean Area (μm^2)	Mean NND (μm)
Compression (0.00625/sec, 15%)	133	2172	5.73786	26.4134	11.929
Compression (0.00625/sec, 30%)	127	2074	6.41771	30.9387	11.3687
Compression (0.00625/sec, 40%)	135	2205	6.96026	31.5658	11.3356

Figure 4.11 Standard light microscope images of H&E stained porcine sections at 40x magnification for unconfined compression at 0.00625 s^{-1}. (TOP-LEFT) Undamaged gray matter. (TOP-RIGHT) Gray matter compressed to 15% strain. (BOTTOM-LEFT) Gray matter compressed to 30% strain. (BOTTOM-RIGHT) Gray matter compressed to 40% strain. (BOTTOM) Tabulated analysis parameters for depicting the distribution of various biological constituents.

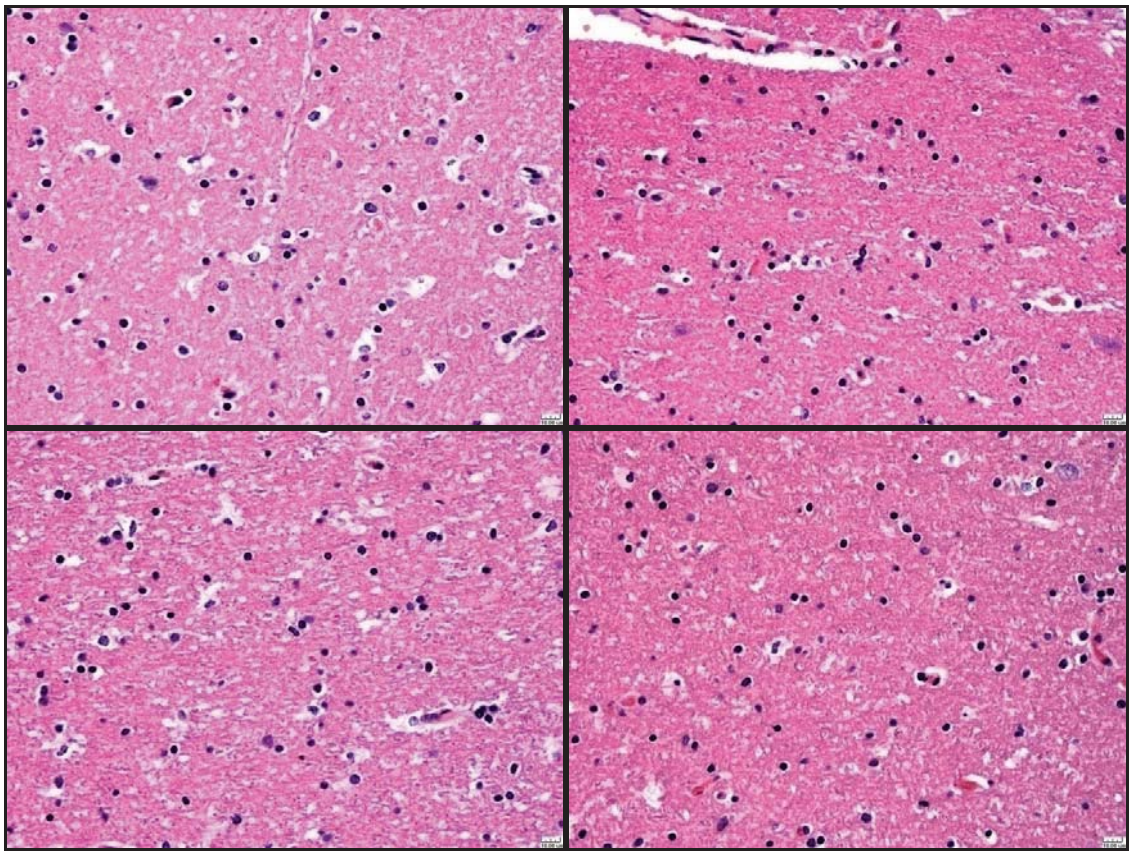

WM Testing Conditions	Object Count	Number Density (cells/mm^2)	Area Fraction (%)	Mean Area (μm^2)	Mean NND (μm)
Compression (0.10/sec, 15%)	208	3397	3.55417	10.4616	8.81089
Compression (0.10/sec, 30%)	247	4034	4.11922	10.2104	8.55098
Compression (0.10/sec, 40%)	315	5145	4.55781	8.85872	7.36645

Figure 4.12 Standard light microscope images of H&E stained porcine sections at 40x magnification for unconfined compression at 0.10 s^{-1}. (TOP-LEFT) Undamaged white matter. (TOP-RIGHT) White matter compressed to 15% strain. (BOTTOM-LEFT) White matter compressed to 30% strain. (BOTTOM-RIGHT) White matter compressed to 40% strain. (BOTTOM) Tabulated analysis parameters for depicting the distribution of various biological constituents.

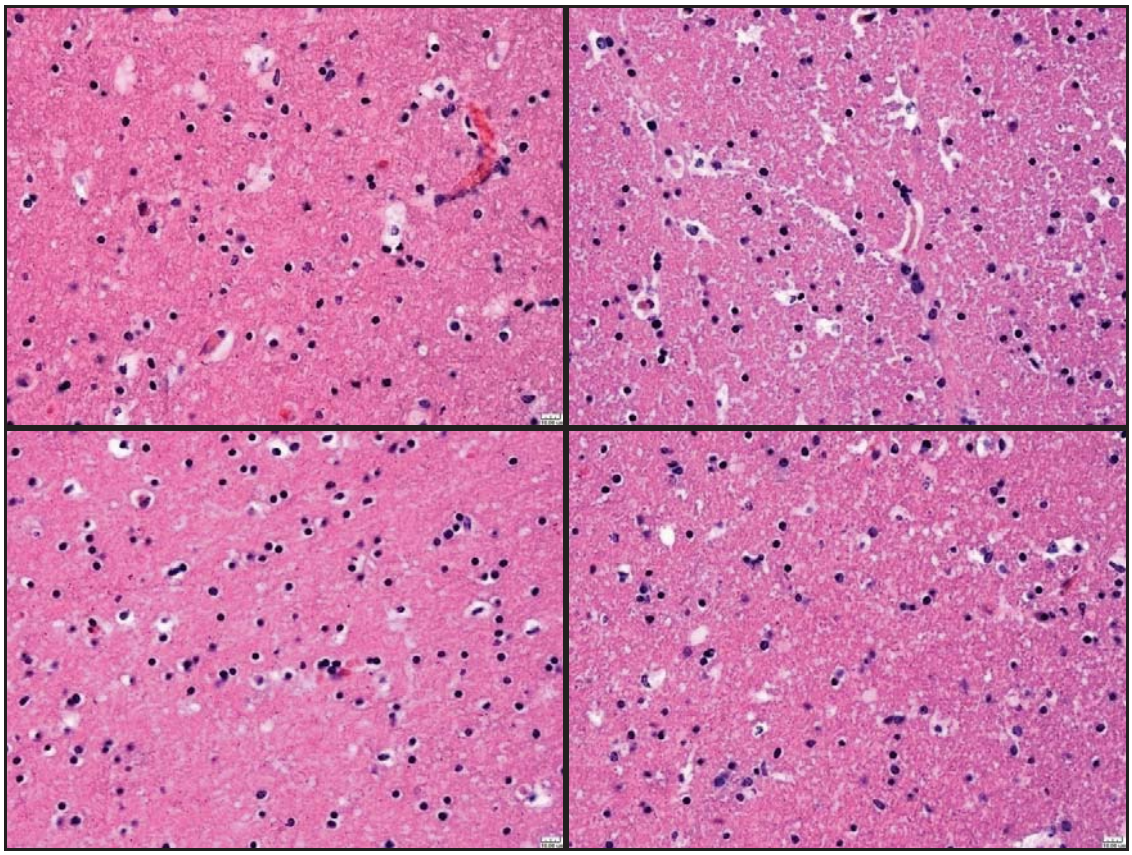

WM Testing Conditions	Object Count	Number Density (cells/mm^2)	Area Fraction (%)	Mean Area (μm^2)	Mean NND (μm)
Compression (0.025/sec, 15%)	163	2662	2.81135	10.5597	10.7502
Compression (0.025/sec, 30%)	180	2940	3.11135	10.5828	10.1122
Compression (0.025/sec, 40%)	197	3217	3.46932	10.7821	9.52263

Figure 4.13 Standard light microscope images of H&E stained porcine sections at 40x magnification for unconfined compression at 0.025 s^{-1}. (TOP-LEFT) Undamaged white matter. (TOP-RIGHT) White matter compressed to 15% strain. (BOTTOM-LEFT) White matter compressed to 30% strain. (BOTTOM-RIGHT) White matter compressed to 40% strain. (BOTTOM) Tabulated analysis parameters for depicting the distribution of various biological constituents.

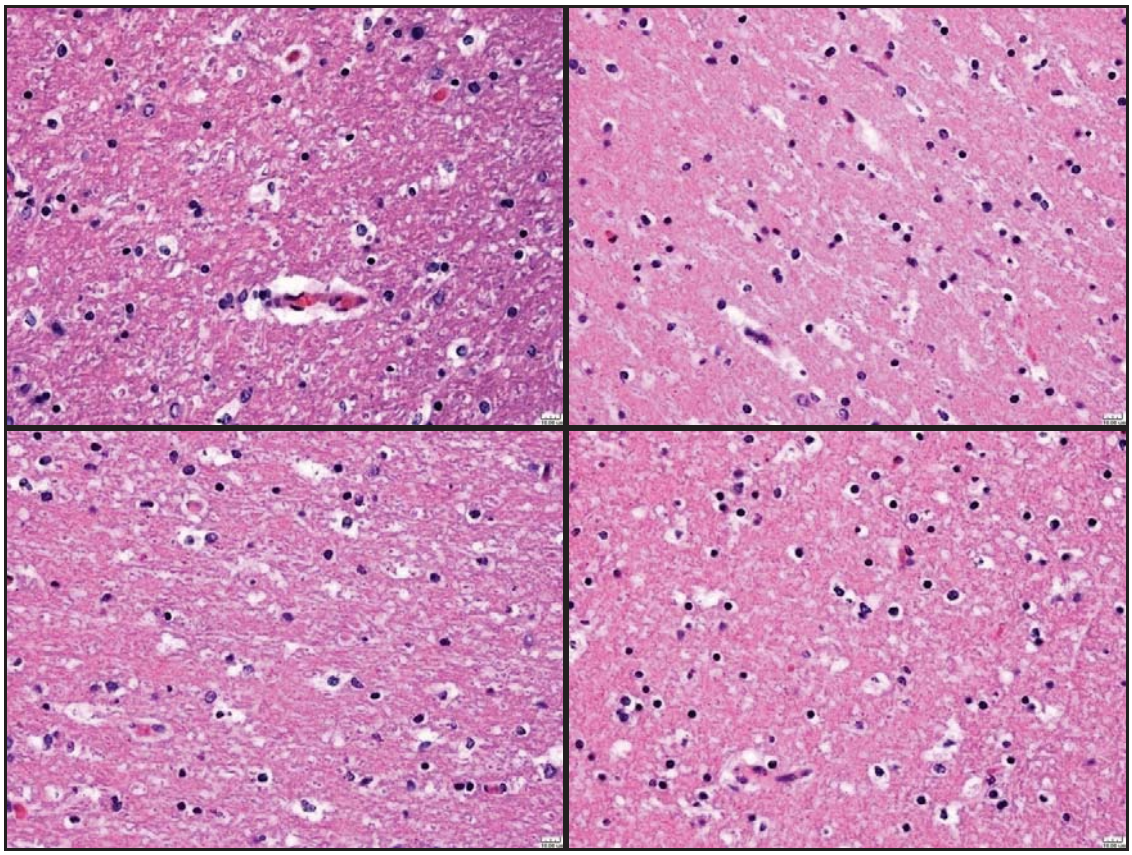

WM Testing Conditions	Object Count	Number Density (cells/mm^2)	Area Fraction (%)	Mean Area (μm^2)	Mean NND (μm)
Compression (0.00625/sec, 15%)	148	2417	2.53948	10.5053	10.6902
Compression (0.00625/sec, 30%)	145	2368	2.71417	11.4602	10.5928
Compression (0.00625/sec, 40%)	160	2613	3.16266	12.102	10.3819

Figure 4.14 Standard light microscope images of H&E stained porcine sections at 40x magnification for unconfined compression at 0.00625 s^{-1}. (TOP-LEFT) Undamaged white matter. (TOP-RIGHT) White matter compressed to 15% strain. (BOTTOM-LEFT) White matter compressed to 30% strain. (BOTTOM-RIGHT) White matter compressed to 40% strain. (BOTTOM) Tabulated analysis parameters for depicting the distribution of various biological constituents.

In addition to strain rate sensitivity, the stress-state dependency of standard light microscope images was determined by utilizing Image Analyzer v2.2-0. Figures 5.12 and 5.13 illustrate the GUI parameters for gray matter and white matter, respectively, which reveal a substantial fluctuation in compressive object count, number density, area fraction (%), and mean NND (µm) when compared to the tensile and shear GUI parameters. For example, the values for the compressive area fraction (%) and mean NND (µm) are 7.49 and 13.51, respectively, while the corresponding values are 6.14% and 22.23 µm for tension 5.55% and 22.93 µm for shear. These trends could be attributed to the distinct failure mechanisms for the compressive testing mode, where compressive forces are more likely to produce a densely packed network of neurons and glial cells within the neural tissue matrix, thus promoting microstructural damage. On the other hand, the tensile and shear testing modes are more susceptible to producing directional or regional concentrations of neurons and glial cells due to the stretching of the tissue matrix under those testing modes. Since visual confirmation of these cellular alterations can still be prone to error, the GUI was utilized as a supplementary tool for measuring the extent of neural damage.

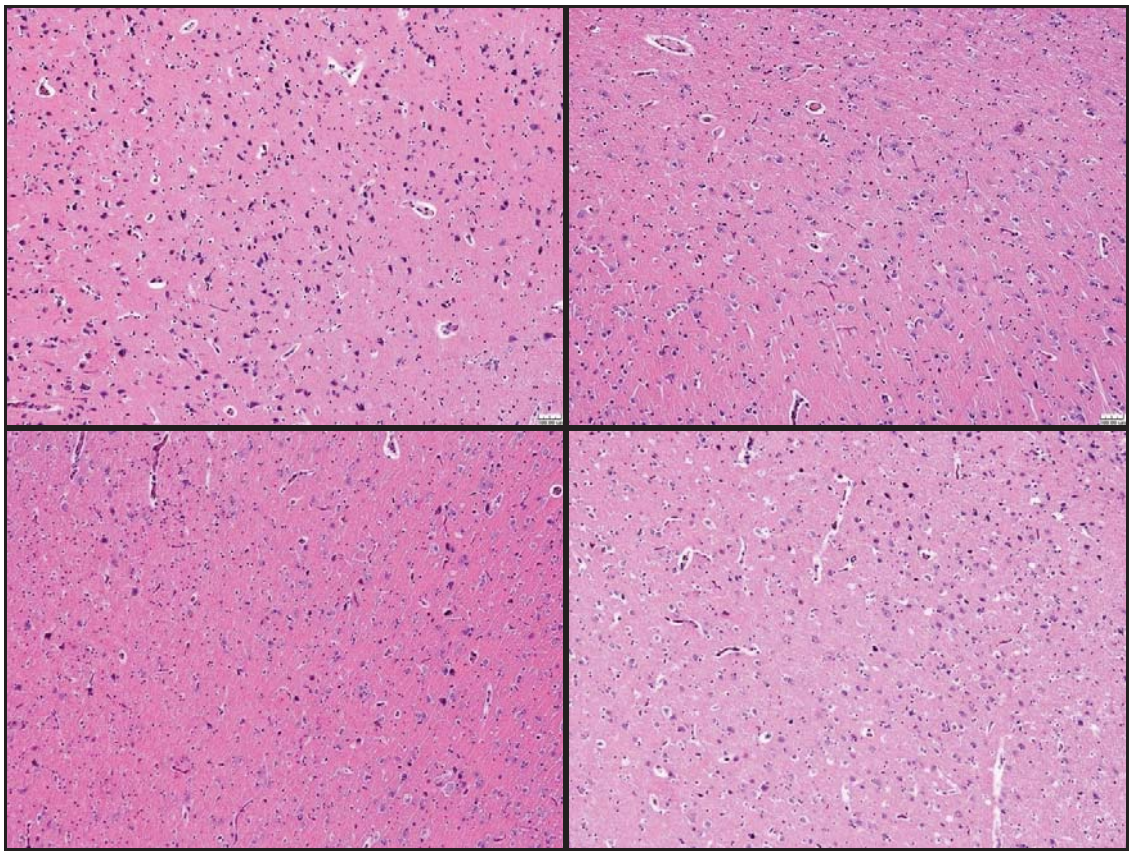

GM Testing Conditions	Object Count	Number Density (cells/mm^2)	Area Fraction (%)	Mean Area (μm^2)	Mean NND (μm)
Control	1773	452	4.7615	105.229	25.648
Compression (0.10/sec, 40%)	5797	1479	7.4911	50.635	13.506
Tension (0.10/sec, 40%)	2352	600	6.141	102.308	22.23
Shear (0.10/sec, 40%)	2102	536	5.5523	103.501	22.933

Figure 4.15 Standard light microscope images of H&E stained porcine sections at 10x magnification for multiple testing modes at 0.10 s^{-1}. (TOP-LEFT) Undamaged gray matter. (TOP-RIGHT) Gray matter compression tested to 40% strain. (BOTTOM-LEFT) Gray matter tension tested to 40% strain. (BOTTOM-RIGHT) Gray matter shear tested to 40% strain. (BOTTOM) Tabulated analysis parameters for depicting the distribution of biological constituents under various loading conditions.

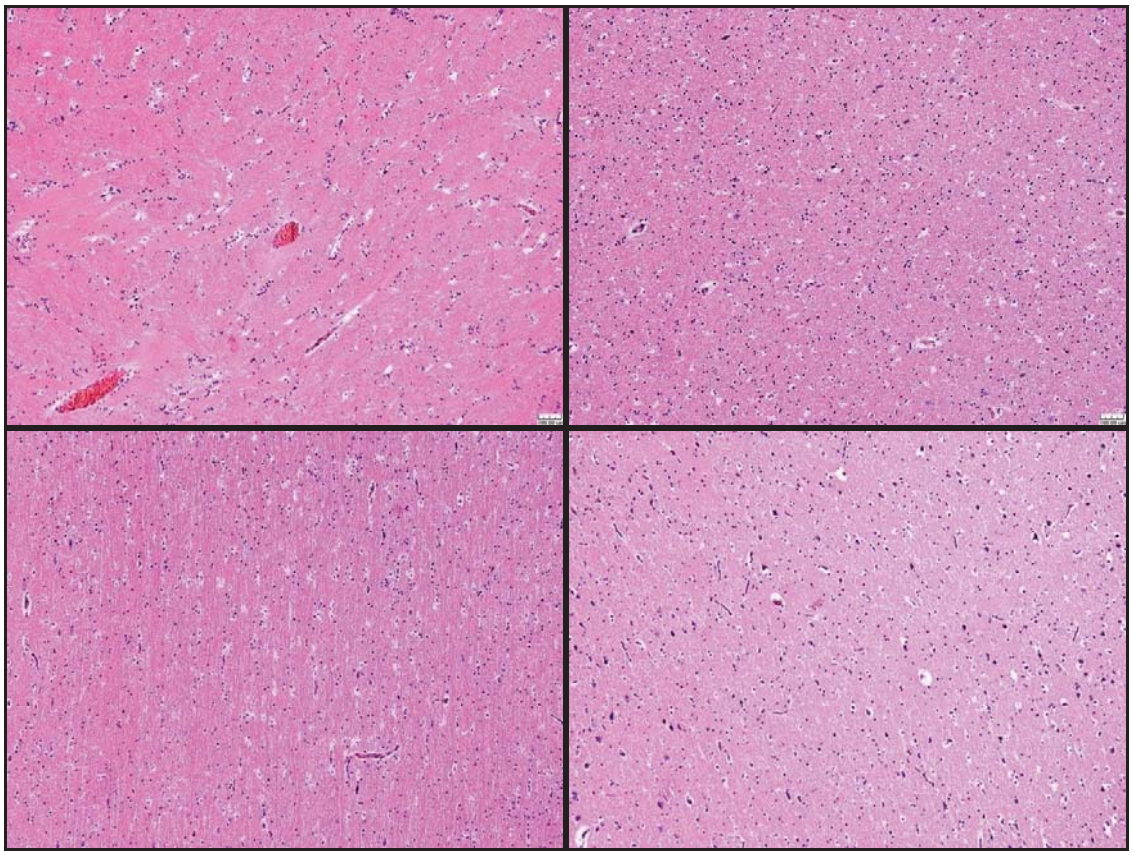

WM Testing Conditions	Object Count	Number Density (cells/mm^2)	Area Fraction (%)	Mean Area (μm^2)	Mean NND (μm)
Control	1745	445	2.4034	53.968	20.861
Compression (0.10/sec, 40%)	6215	1586	5.0497	31.837	13.452
Tension (0.10/sec, 40%)	2330	594	3.9204	65.929	22.205
Shear (0.10/sec, 40%)	2074	529	4.6672	88.176	24.634

Figure 4.16 Standard light microscope images of H&E stained porcine sections at 10x magnification for multiple testing modes at 0.10 s^{-1}. (TOP-LEFT) Undamaged white matter. (TOP-RIGHT) White matter compression tested to 40% strain. (BOTTOM-LEFT) White matter tension tested to 40% strain. (BOTTOM-RIGHT) White matter shear tested to 40% strain. (BOTTOM) Tabulated analysis parameters for depicting the distribution of biological constituents under various loading conditions.

Compressive Moduli Calculations

Although the structure-property relation in Figure 4.5 exhibited strain rate dependence in porcine brain tissue undergoing quasi-static compressive rates, further analysis was applied to the approximately linear regions of the plots to provide another method for determining the strain rate sensitivity. As seen in Table 4.1, the compressive moduli were calculated for strain intervals of 1% to 5%, 6% to 10%, 11% to 15%, and 16% to 20%. Based on the tabulated values, strain rate sensitivity is evident in porcine brain tissue since the compressive moduli steadily rise with increasing strain rate. At the strain interval between 16% and 20%, for example, the compressive moduli are 3240.62 Pa, 3386.99 Pa, and 6245.99 Pa for strain rates of 0.00625 s^{-1}, 0.0025 s^{-1}, and 0.10 s^{-1}, respectively. It is also important to note that compressive moduli for the lower two strain rates were within a relatively narrow range of one another, which also coincides with the similar inelastic behavior shown in the stress-strain plots of Figure 4.5.

Table 4.1 Overview of compressive moduli calculated within the approximately linear regions of the strain rate dependency plots previously shown in Figure 4.5.

Strain Rate	Strain Intervals			
	1% - 5%	6% - 10%	11% - 15%	16% - 20%
0.10/sec	1646.72	3072.81	4158.57	6245.99
0.025/sec	1367.59	1794.73	2550.68	3386.99
0.00625/sec	1305.77	1769.42	2453.31	3240.62

Statistical Analysis of Strain Rate Dependency Results

The statistical analysis tool used was SigmaStat (Systat Software, San Jose, CA), which utilized Sidak-Holms t-tests for multiple comparisons of the GUI parameters and the strain levels for different pairings of strain rates. As seen in Table 4.2, the analysis parameters of object count, area fraction, and mean NND are compared among the respective strain rate pairings. These parameters were selected since they indicated consistent trends in their associated structure-property relationships.

Table 4.2 Statistical comparisons of specific analysis parameters for strain rate pairings at different strain levels for an alpha-value of 0.05.

GUI Analysis Parameter	Strain Level	Strain Rate Pairings	p-value	Significant Difference
Object Count	15%	0.10/sec and 0.025/sec	0.049	YES
		0.025/sec and 0.00625/sec	0.016	YES
		0.00625/sec and 0.10/sec	0.023	YES
GUI Parameter	**Strain Level**	**Strain Rate Pairings**	**p-value**	**Significant Difference**
Object Count	40%	0.10/sec and 0.025/sec	0.025	YES
		0.025/sec and 0.00625/sec	0.061	NO
		0.00625/sec and 0.10/sec	0.004	YES

Table 4.2 (continued)

GUI Analysis Parameter	Strain Level	Strain Rate Pairings	p-value	Significant Difference
Area Fraction	15%	0.10/sec and 0.025/sec	0.055	NO
		0.025/sec and 0.00625/sec	0.66	NO
		0.00625/sec and 0.10/sec	0.065	NO
GUI Parameter	**Strain Level**	**Strain Rate Pairings**	**p-value**	**Significant Difference**
Area Fraction	40%	0.10/sec and 0.025/sec	0.003	YES
		0.025/sec and 0.00625/sec	0.365	NO
		0.00625/sec and 0.10/sec	0.005	YES

GUI Analysis Parameter	Strain Level	Strain Rate Pairings	p-value	Significant Difference
Mean NND	15%	0.10/sec and 0.025/sec	0.388	NO
		0.025/sec and 0.00625/sec	0.277	NO
		0.00625/sec and 0.10/sec	0.081	NO
GUI Parameter	**Strain Level**	**Strain Rate Pairings**	**p-value**	**Significant Difference**
Mean NND	40%	0.10/sec and 0.025/sec	0.077	NO
		0.025/sec and 0.00625/sec	0.408	NO
		0.00625/sec and 0.10/sec	0.088	NO

Although there was no significant difference for any of the strain rate pairings with respect to the mean NND at 15% and 40% strain, there was a significant difference in the area fraction at 40% strain for strain rate pairings between 0.10 s^{-1} and 0.025 s^{-1} and between 0.10 s^{-1} and 0.00625 s^{-1}. Moreover, significant differences were observed

in the object count for all strain rate pairings with the exception of 0.025 s^{-1} and 0.00625 s^{-1} at 40% strain.

Aside from the analysis parameters generated by the GUI, Sidak-Holms t-tests were also utilized for comparing the stresses recorded at each of the strain levels targeted for confocal imaging, which is shown in Table 4.3. In general, significant differences were seen in strain rate pairings between 0.10 s^{-1} and 0.025 s^{-1} and between 0.10 s^{-1} and 0.00625 s^{-1} for the stresses measured at strain levels of 15%, 30%, and 40%. However, at each of the designated strain levels, there was no significant difference in the recorded stresses for the strain rate pairing between 0.025 s^{-1} and 0.00625 s^{-1}.

Table 4.3 Statistical comparisons of the measured stresses for strain rate pairings at different strain levels for an alpha-value of 0.05.

Strain Level	Strain Rate Pairings	p-value	Significant Difference
15%	0.10/sec and 0.025/sec	< 0.001	YES
	0.025/sec and 0.00625/sec	0.447	NO
	0.00625/sec and 0.10/sec	< 0.001	YES
Strain Level	**Strain Rate Pairings**	**p-value**	**Significant Difference**
30%	0.10/sec and 0.025/sec	< 0.001	YES
	0.025/sec and 0.00625/sec	0.601	NO
	0.00625/sec and 0.10/sec	< 0.001	YES
Strain Level	**Strain Rate Pairings**	**p-value**	**Significant Difference**
40%	0.10/sec and 0.025/sec	< 0.001	YES
	0.025/sec and 0.00625/sec	0.244	NO
	0.00625/sec and 0.10/sec	< 0.001	YES

Statistical Analysis of Stress-State Dependency Results

In addition to the statistical analysis on strain rate pairings for GUI parameters and stresses measured at the strain levels selected for confocal imaging, statistical comparisons were also determined for stress-state pairings. As seen in Table 4.4, Sidak-Holms t-tests were utilized for determining if there were significant differences in the object count, area fraction, and mean NND between compression and tension, between tension and shear, and between shear and compression, respectively.

Overall, there were significant differences in the object count, area fraction, and mean NND for stress-state pairings between compression and tension and between compression and shear. However, there were no significant differences in the previous analysis parameters for the stress-state pairing between tension and shear.

Table 4.4 Statistical comparisons of analysis parameters for stress-state pairings for an alpha-value of 0.05.

GUI Analysis Parameter	Stress-State Pairings	p-value	Significant Difference
Object Count	Compression and Tension	0.006	YES
	Tension and Shear	0.773	NO
	Shear and Compression	0.005	YES
GUI Analysis Parameter	**Stress-State Pairings**	**p-value**	**Significant Difference**
Area Fraction	Compression and Tension	0.001	YES
	Tension and Shear	0.086	NO
	Shear and Compression	0.002	YES
GUI Analysis Parameter	**Stress-State Pairings**	**p-value**	**Significant Difference**
Mean NND	Compression and Tension	0.009	YES
	Tension and Shear	0.901	NO
	Shear and Compression	0.006	YES

CHAPTER V

DISCUSSION

Interpretation of Analysis Parameters

Based on the confocal analysis, the distribution of neurons and glial cells in compressive test specimens exhibited a tightly packed configuration due to the compaction of the neural tissue. As a result of this tissue behavior, analysis parameters such as the object count, number density, and area fraction steadily increased with rising strain rate and strain level. On the other hand, the mean NND gradually decreased with progressive strain rate and strain level since the denser neural tissue matrix contained neurons and glial cells that were in closer proximity to one another. As for the tensile test specimens, the biological constituents throughout numerous tissue regions exhibited a linear arrangement. This dispersal pattern varied considerably from the more compact network of biological constituents detected in the compressive test specimens. However, the microstructural organization of the tensile test specimens coincided with the shear test specimens since the neuron and glial cell distribution also demonstrated directional orientation throughout the neural tissue. Comparison of the compressive, tensile, and shear analysis parameters revealed that the object count, number density, and area fraction for compression were substantially higher than those for both tension and shear. Meanwhile, the mean NND was significantly lower for

compression in contrast to both tension and shear. The correlations observed in the analysis parameters reflected the varying tissue behavior under the applied stresses of the different testing modes. While compressive forces condensed the neural tissue matrix and its constituents, tensile and shear forces extended the neural tissue matrix causing the neurons and glial cells to gradually align within the tightly stretched regions.

As evidenced with the confocal images, a microstructural damage assessment on H&E stained images revealed similar trends in the resulting analysis parameters. Strain rate dependency was apparent since the object count, number density, and area fraction steadily increased with advancing strain rate and strain level while the mean NND gradually decreased with rising strain rate and strain level. Furthermore, these relations were observed in porcine sections primarily comprised of gray matter as well as porcine sections mainly composed of white matter.

Aside from the analysis parameters obtained for progressive stages of testing in the strain rate dependency protocol, the compressive moduli were also calculated within the approximately linear regions of the respective plots. Despite similar viscoelastic behavior observed at earlier strain levels in the experimental data, strain rate sensitivity was evident with the compressive moduli steadily increasing as the strain level progressed. This behavior is indicative of most biological materials and can be attributed to the inherent viscoelastic properties, where the combined fluid and solid material characteristics of the brain tissue cause the stresses to not only be a function of strain but also a function of strain rate (Ozkaya, 1999).

In addition to strain rate sensitivity, the stress-state dependency of standard light microscope images was determined by utilizing Image Analyzer v2.2-0. The analysis parameters associated with both gray matter and white matter exhibited a considerable difference between the object count, number density, area fraction, and mean NND of compressive test specimens to those obtained from tensile and shear test specimens. The disparities in the analysis parameters could be attributed to the distinct failure mechanism in the compressive testing mode, where compressive forces were capable of generating microstructural damage by condensing the neural tissue and potentially localizing deformations in the neurons and glial cells. While many studies in literature have focused on the biomechanical behavior of brain tissue, few have specifically targeted the mechanical properties of neural cells. In one study assessing the viscoelastic properties of neural cells in the rat CNS, it was determined that CNS cells behaved as elastic solids and that glial cells were twice as compliant as neurons. Furthermore, researchers discovered that for a frequency range between 30 and 200 Hz, neurons had elastic moduli ranging from 480 to 980 Pa while glial cells had elastic moduli ranging from 300 to 520 Pa (Lu, 2006). As for the tension and shear testing modes, the microstructural damage could be generated by tensile and shear forces that stretched the neural tissue, creating linearly concentrated regions of neurons and glial cells. Although visual confirmation of the localized deformations was not achieved, the GUI was sufficiently utilized for determining the extent of neural damage by analyzing the distribution of neurons and glial cells.

Clinical Implications

Despite TBI being more probable in situations involving significantly higher strain rates, Miller and Chinzei investigated the biomechanical behavior of the brain under quasi-static conditions. The rationale for this research centered on various medical applications such as the development of automated surgical systems to provide an additional tool for surgeon training. However, safe and precise operation of these medical systems would require more accurate depictions of the mechanical properties of brain tissue, which would necessitate constitutive modeling with data obtained from experiments conducted at lower strain rates under 1 s^{-1} (Miller, 2000). In general, comparisons of prior work by Miller and Chinzei with the compressive and tensile data from this study revealed many similarities. However, the supplementary data from the corresponding image analysis in this study provides a more comprehensive depiction of the strain rate dependence as well as stress-state dependence in porcine brain. While analysis parameters such as area fraction and mean NND offer a quantitative assessment of the progressive tissue damage under varying testing conditions, these parameters could also be utilized in finite element applications.

In addition to the compressive and tensile behavior, the mechanical properties of the brain undergoing shear is vital for understanding the mechanisms of tissue damage such as diffuse axonal injury (DAI). Clinical findings have associated DAI with specific damage to the cerebral white matter that typically produces lesions in both the brainstem and corpus callosum. According to prior work in literature, DAI has been correlated with tissue deformations that were reliant on the loading direction and

attributed to rotational inertial loads. In a study conducted Arbogast and Margulies, it was determined that the brainstem and corpus callosum were more vulnerable to shear deformations due to the following: the CNS geometry, the regional differences in material properties, and the anisotropy of the selected brain regions. In order to examine the vulnerability of the brainstem and corpus callosum to DAI, researchers subjected skulls filled with a homogenous viscoelastic material to rotational loads sufficient for recreating DAI. Based on the distribution of deformation observed through a high speed camera, it was determined that both brain regions were more prone to higher strains under rotational loading than the cerebrum, thus making these two regions more susceptible to DAI than cerebral tissue. Moreover, the observed anisotropy in the selected brain regions was the result of the primarily longitudinal axonal fiber arrangement (Arbogast, 1998), which contrasted with findings by Shuck and Advani who revealed in their study that the cerebrum primarily demonstrated isotropic behavior due to the inherently random distribution of axonal fibers (Shuck, 1972). However, the data obtained from that study only achieved strain levels of 0.013, which are substantially lower than the strains generally associated with TBI (Prange, 1998). On the other hand, the experimental shear data obtained from the stress-state dependency testing protocol exhibited tissue failure that appeared to initiate at an estimated strain level of 20% since the stresses declined significantly. This observation coincides with prior work in literature suggesting that injury thresholds from rotational loads and consequently DAI occurred at 20% strain (Prange, 2002). In addition to the comparable experimental results, this study also provides supplementary image analysis data that

could lead to further characterization of the tissue failure mechanism for the shear testing mode. For instance, a more detailed microstructural damage assessment at strain intervals preceding 20% could offer insight regarding the damage progression potentially caused by DAI, and analysis parameters such as the area fraction and mean NND would provide a quantitative comparison against undamaged tissue. These findings could then be correlated with rotational loads to more accurately determine the minimum extent of TBI.

Aside from the complications associated with primary injury in TBI scenarios, such as tearing, shearing, or hemorrhaging of neural tissue, secondary injury involves cascades of biological reactions that can exacerbate the initial trauma. A primary complication seen in focal and diffuse brain damage is traumatic axonal injury (TAI), which serves as the predominant failure mechanism in white matter tracts. TAI is a delayed degenerative process that occurs as a result of the axon detachment, or secondary axotomy, which can be attributed to improper cytoskeleton alignment, denser compaction of neurofilaments, and deterioration of microtubules (Kelley, 2006). Abnormal calcium homeostasis is another pathway leading to the progression of secondary injury in both gray matter and white matter since it promotes further damage to neural constituents. High calcium concentrations can result in mitochondrial swelling that causes the release of chemical agents associated with programmed cell death in neurons. In addition, elevated calcium levels can produce axonal injury by initiating a series of protein degradation cascades that generate disconnections in axonal fibers. These detachments occur when axonal membranes deteriorate and facilitate excessive

calcium penetration, which causes enzymes to degrade proteins responsible for maintaining normal axonal structure. Figure 5.1 exhibits the numerous biological pathways that can potentially contribute to the overall progression of secondary injury (Park, 2008).

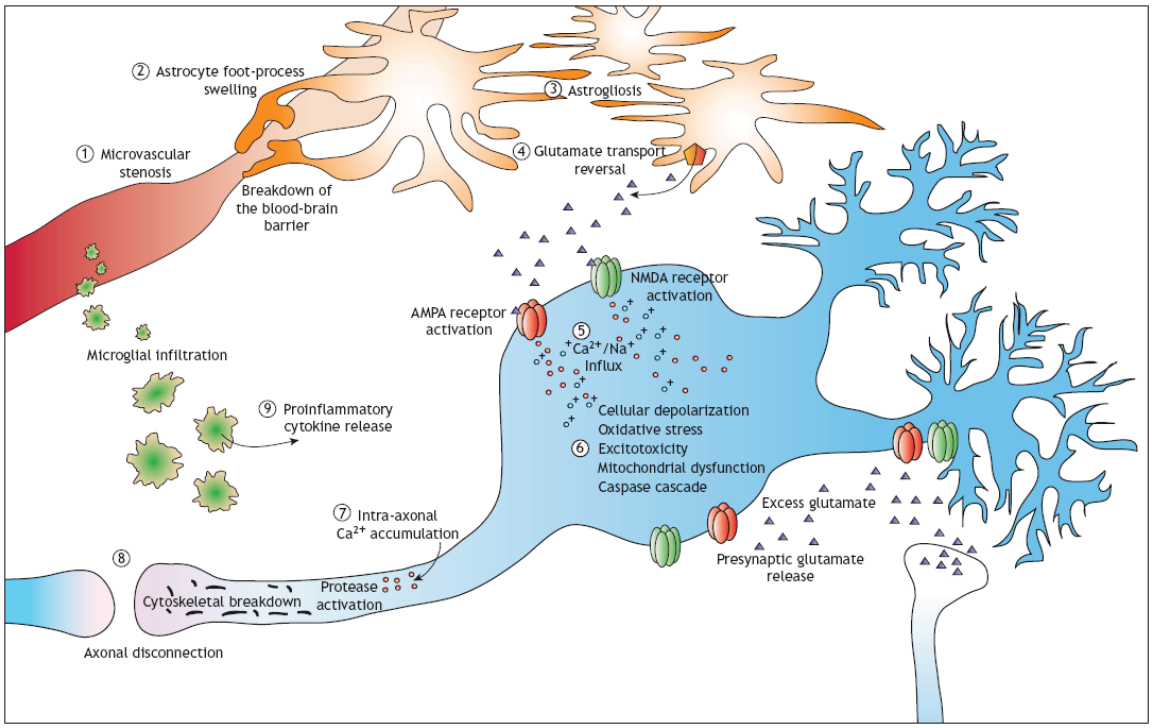

Figure 5.1 Pathways associated with the progression of secondary injury following a traumatic brain injury (adapted from Park, 2008).

Successful treatment in TBI cases depends on the ability of medical facilities to effectively manage the secondary injury mechanisms that result from the initial physical trauma. Therefore, more accurately depicting the mechanical properties of neural constituents such as neurons and axons is vital for fully understanding their minimum threshold of damage due to their sensitive structural nature. A significant feature of this

study involves the analysis of confocal images and H&E images with the aid of a graphical user interface. This GUI can be helpful in quantifying specific tissue characteristics under various testing conditions, which includes the overall distribution pattern of neurons and glial cells in damaged tissue versus a control. These analysis parameters could eventually prove useful for indicating the lower thresholds of injury. For example, the area fraction and mean NND for both undamaged and deformed tissue could provide a quantitative basis for determining the minimum potential level of injury.

Comparisons with Prior Results in Literature

With results obtained from the structure-property relation in Figure 4.5, the compressive stress-strain data for a strain rate of 0.006 s^{-1} to 40% strain was compared to prior work with quasi-static compression on porcine brain tissue (Miller, 2000; Miller, 2005). Figure 5.2 illustrates the similar inelastic behavior observed between the experimental stress-strain data and the Miller stress-strain data to nearly 15% strain, where the estimated stresses are 315.85 Pa and 329.26 Pa, respectively. As the strain level progresses from 15%, however, the compressive moduli from the Miller stress-strain data increase more abruptly than the compressive moduli from the experimental stress-strain data, which can be attributed to variations in the testing protocols. The cross-sectional area of the circular platen utilized is one factor that could lead to the slight deviations between the tissue responses of the Miller results and experimental results because the compressive forces applied could potentially be inconsistent. Another testing feature could also be the loading velocities employed, which could

slightly deviate as a result of minimal variations in the initial height and diameter of cylindrical test specimens.

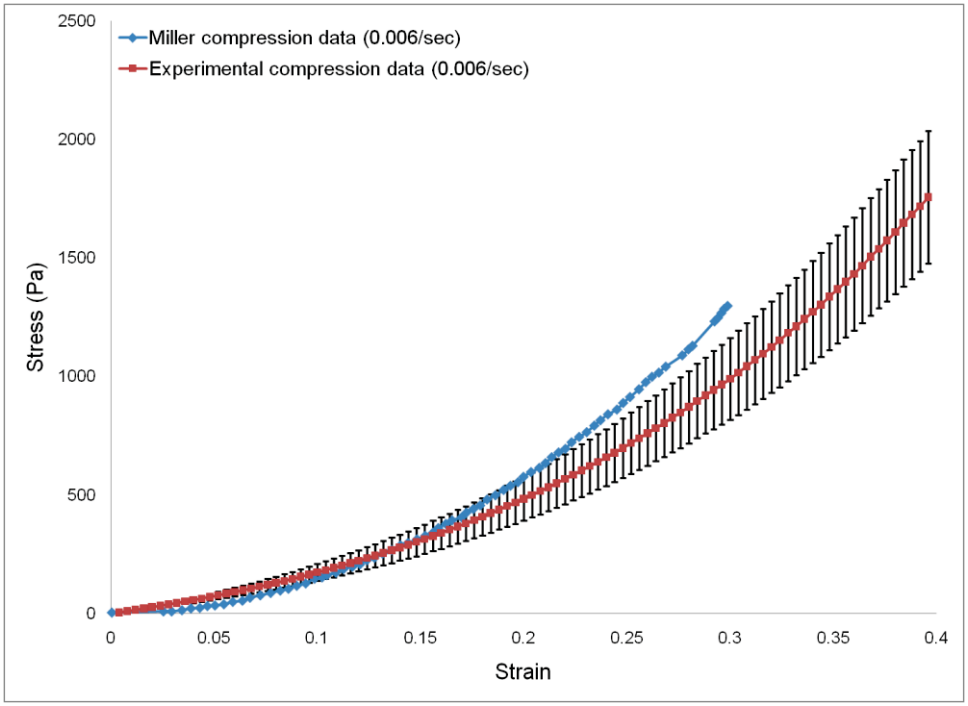

Figure 5.2 Comparison of quasi-static compressive data with previous work in literature (adapted from Miller, 2000; Miller, 2005).

In addition to the comparative evaluation of the compressive data, similarities were assessed for the tensile data at a strain rate of 0.006 s^{-1} to 40% strain. As shown in Figure 5.3, Miller tension testing results are compared with the current experimental results to evaluate the tissue responses based on the different testing protocols (Miller, 2002). Similar inelastic behavior is evident with the characteristic downward concavity associated with tension plots, and the stresses for the Miller and experimental data at 3.5% strain are 48.93 Pa and 57.31 Pa, respectively. As the strain level advances past 3.5%, however, the tensile moduli from the experimental data are stiffer when

compared to the Miller data and could be attributed to variations in experimental parameters. In addition to differences in the cross-sectional areas of the circular platens utilized, the stress deviations could also be the result of inconsistencies in the geometry of test specimens, which can slightly alter the loading velocities applied. The adhesive strength of the cyanoacrylate used is another potential factor since the subtle detachment of test specimens would lead to insufficient load readings.

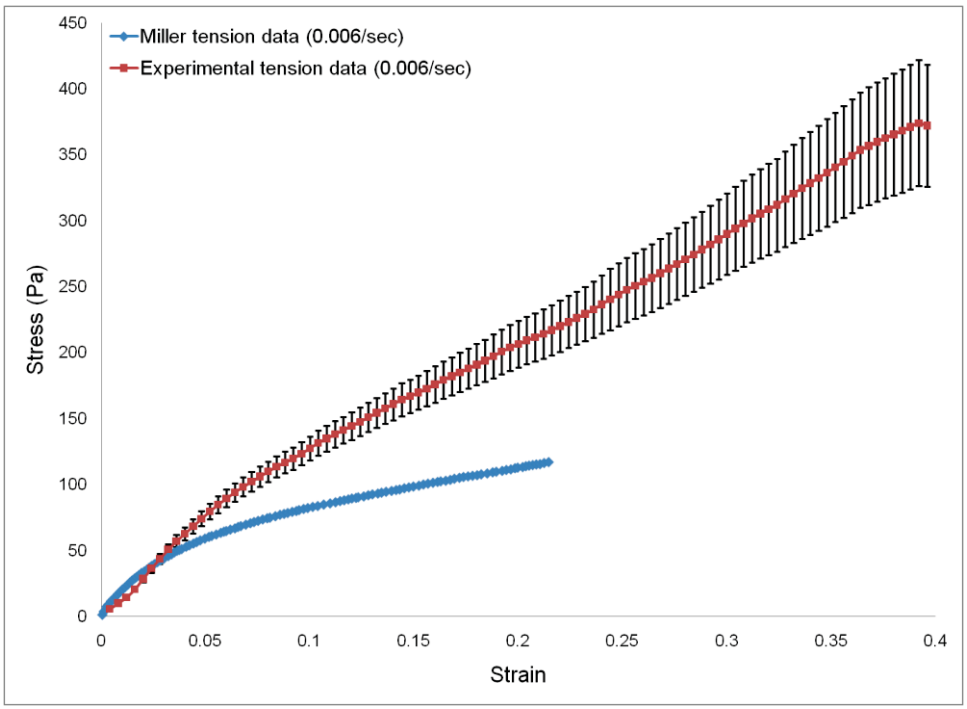

Figure 5.3 Comparison of tensile data with previous work in literature (adapted from Miller, 2002).

As with the previous testing modes of compression and tension, comparisons were also generated between shear data from the current experiments and shear data in literature (Donnelly, 1997). Figure 5.4 reveals a significant disparity in the Donnelly stress-strain data and the actual stress-strain data due to multiple factors. The use of

different neural specimens for shear testing is one notable aspect because the experiments by Donnelly were performed on human brains acquired from autopsy while this series of experiments were conducted on porcine brains collected immediately after sacrifice. Another influential experimental feature is the testing device utilized. While Donnelly used a custom-designed parallel-plate apparatus with an impact cart, the current experiments incorporated a fixed-end shear testing system, which could explain the distinctive nonlinear behavior observed. Furthermore, variations in the sample configurations, corresponding loading velocities, and adhesive reliability could substantially alter the shear stress readings. Comparisons between the Donnelly shear data and the experimental shear data in Figure 5.4 show that the estimated peak stresses for the Donnelly results and the experimental results are 1168.40 Pa and 1034.91, respectively. In addition, the Donnelly shear plot exhibits erratic behavior with a steadily rising trend. As for the experimental plot, a gradual decline in shear stresses is noticeable after nearly 20% strain, which could be attributed to the failure of the neural tissue or weakening of the adhesive.

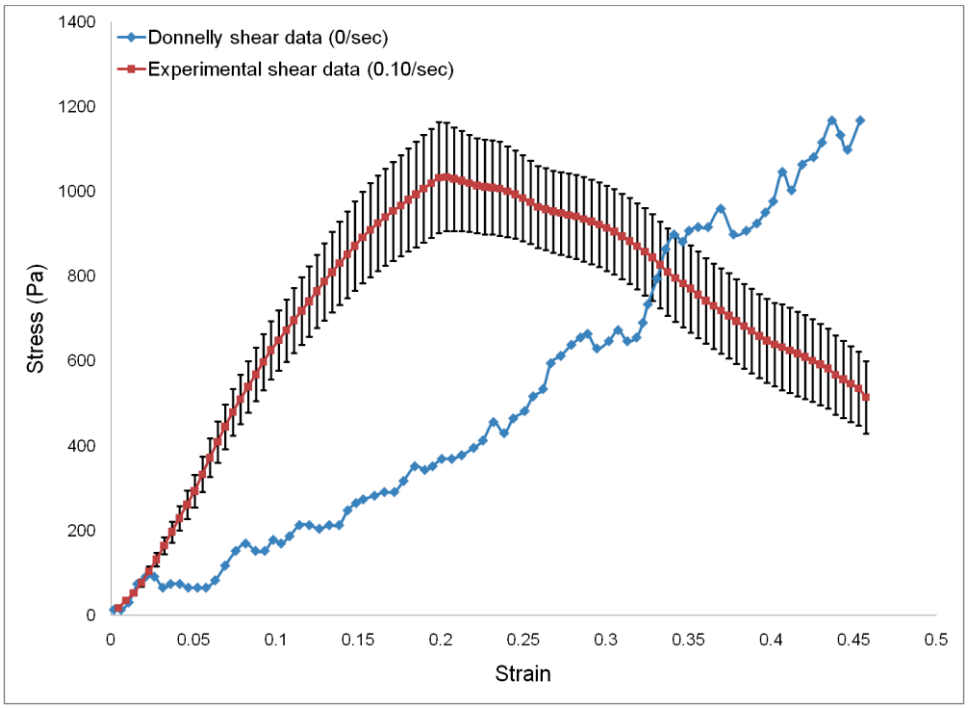

Figure 5.4 Comparison of shear data with previous work in literature (adapted from Donnelly, 1997).

Experimental Limitations

Despite the meticulous nature of the experiments conducted, limitations were still encountered. The range of strain rates used in this study was restricted by the Mach-1^{TM} programming since data points for the vertical position (μm) and load (g) could only be recorded at time increments of 0.1 s. As shown in Table 5.1, strain rates higher than 0.10 s^{-1} would reduce the collection of data points and the precision of the derived stress-strain plots.

Table 5.1 Overview of the data points available based on strain rate.

Strain Rate (1/s)	Loading Velocity (μm/s)	Test Time (s)	Number of Data Points
0.00625	93.75	64.00	640
0.025	375	16.00	160
0.1	1500	4.00	40
0.2	3000	2.00	20
0.3	4500	1.33	13
0.4	6000	1.00	10
0.5	7500	0.80	8
0.6	9000	0.67	7
0.7	10500	0.57	6
0.8	12000	0.50	5
0.9	13500	0.44	4
1	15000	0.40	4

In order to achieve sufficient sample sizes for different experimental protocols, additional test specimens were extracted from anatomical sites other than the posterior region of the left hemisphere. Despite the potentially varying contributions of white and gray matter, additional test specimens were procured from the anterior and posterior regions of the right hemisphere in addition to the anterior section of the left hemisphere. Since all test specimens were obtained from healthy male pigs of the same age, biological variability was presumed to be mainly relative to extraction locations. As shown in Figure 5.5, a series of unconfined compression experiments were performed at a designated strain rate of 0.025 s^{-1} to a specified strain level of 40% to measure the influence of varying excision sites.

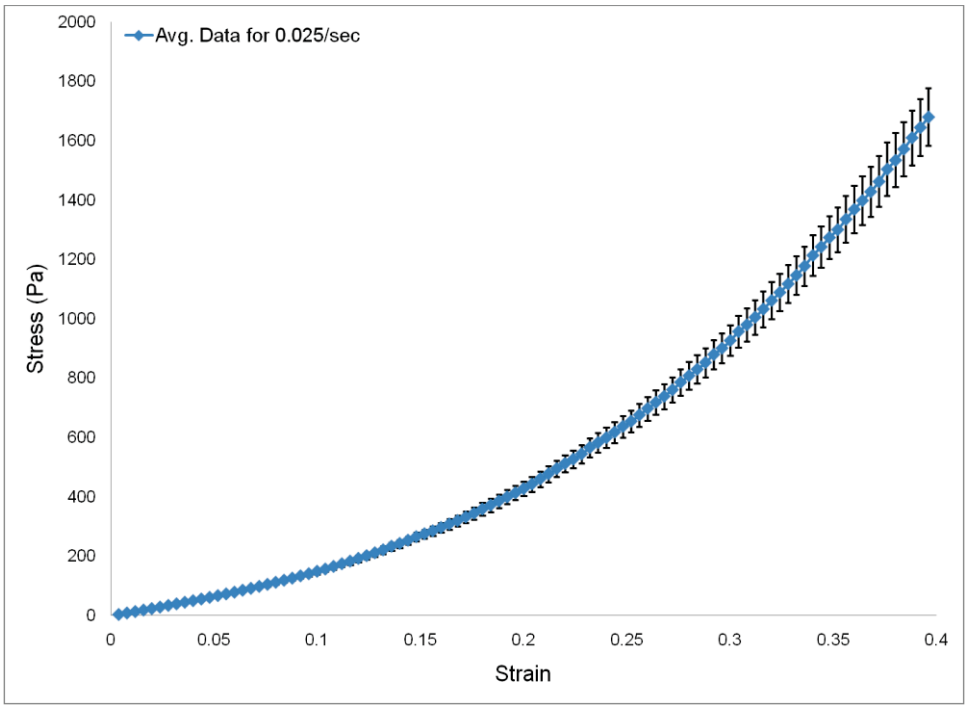

Figure 5.5 Stress-strain data depicting the comparable viscoelastic behavior of porcine brain tissue despite variations in resection locations with error bars representing standard deviations.

In spite of variations in resection locations, Figure 5.5 illustrates steady viscoelastic behavior with stress-strain data incorporated from unconfined compression experiments conducted on two separate porcine brains. More specifically, four test specimens were collected from the left hemisphere while three were retrieved from the right hemisphere. At strain levels of 15%, 30%, and 40%, which were continually utilized for confocal analysis, the average stresses and standard deviations were the following: 275.26 ± 15.25 Pa, 927.14 ± 51.59 Pa, and 1680.72 ± 97.52 Pa. Figure 5.5 confirms that regardless of the strain level targeted for a single compression test, the resulting stress-strain plots exhibit similar inelastic behavior.

Within the strain rate dependency protocol, 10% NBF was utilized for fixing test specimens at varying strain levels and strain rates prior to confocal imaging. However, each strain level had to be achieved in separate tests to facilitate confocal analysis at each condition. In Figure 5.6, consistent viscoelastic behavior can be observed after superimposing the stress-strain plots from compression experiments run at an identical strain rate of 0.025 s^{-1} but to progressive strain levels of 15%, 30%, and 40%. In particular, similar stresses and standard deviations of 229.84 ± 5.96, 265.41 ± 32.38, and 275.26 ± 15.25 Pa were evident at a common strain level of 15% for compression tests run to 15%, 30%, and 40% strain, respectively. Based on the similar viscoelastic behavior exhibited by the compiled experimental data, there is an inherent uniformity existing between test specimens despite attaining different strain levels at an identical strain rate, which validates the confocal imaging of test specimens at the intermediate target strain levels of 15% and 30%.

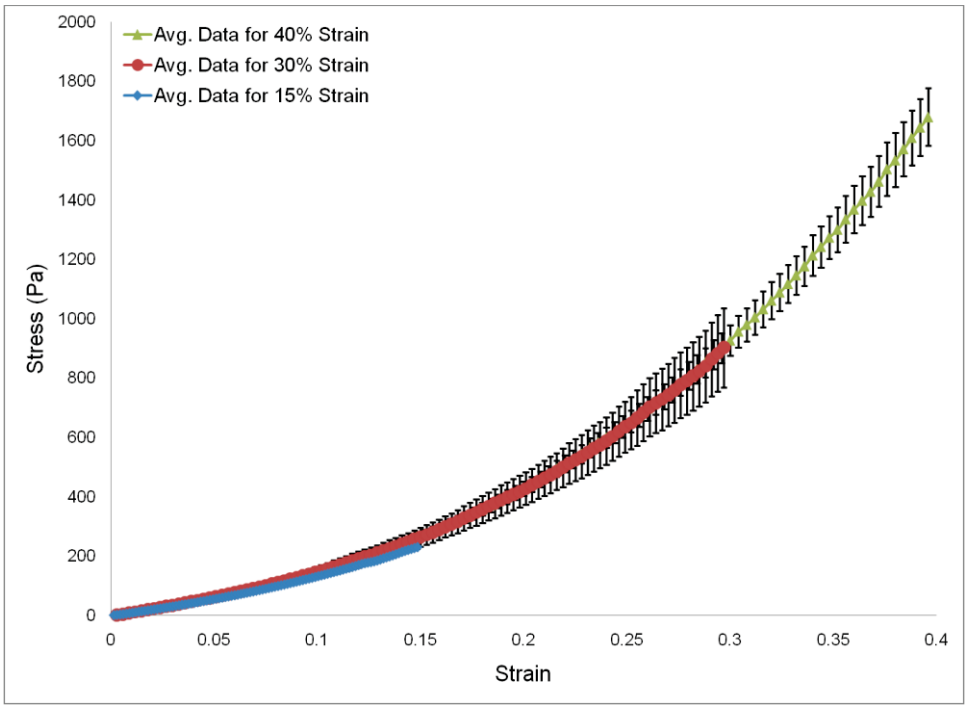

Figure 5.6 Stress-strain data obtained from separate compression tests run to 15%, 30%, and 40% strain illustrating consistent viscoelastic behavior. Error bars represent standard deviations.

Summary

Despite thorough implementation of multiple experimental protocols, an additional limitation of this study pertained to the microstructural damage assessment and the GUI parameters calculated by Image Analyzer v2.2-0. Although consistent cylindrical geometries were maintained for each test sample, subtle variations in the resection locations could not be completely circumvented. In conjunction with the inherent biological variability already existing between different porcine brain specimens, this incidence could potentially introduce additional deviations to the GUI parameters.

On the other hand, assumptions regarding specific features of the strain rate dependency protocol were verified. For example, the confocal imaging at intermediate strain levels of 15% and 30% were validated because consistent viscoelastic behavior was observed in the compressive stress-strain data for a constant strain rate and regardless of the strain level designated. In addition, the deviations in the viscoelasticity of the tissue response were considered to be minimal even with variation in the anatomical excision sites.

The structure-property relation produced in Figure 4.5 depicts strain rate dependence because varying degrees of inelastic behavior are evident for all three strain rates, where relatively minimal deviations are shown at lower strain levels and slightly higher deviations are observed as the strain level progresses. Furthermore, the structure-property relation generated for Figure 4.8 reveals exceedingly distinct nonlinear stress-strain behavior for each testing mode, suggesting that constitutive models must incorporate variables exclusively to each experimental condition. Based on the values shown in Table 4.1, the compressive moduli steadily rise with increasing strain rate and strain level, further confirming strain rate sensitivity for porcine brain tissue. This phenomenon can be attributed to microstructural deformations that initially propagate throughout the neural tissue matrix as the biological constituents progressively become more densely packed, which explains the correlation between the modulus and strain rate. GUI parameters such as object count, number density (μm), area fraction (%), and mean NND (μm) are also correlated with rising strain rate and

strain level, and these values further signify the neural tissue deformations that occur due to the redistribution of neurons and glial cells.

In general, these experimental plots illustrate that minimal fluctuations in quasi-static strain rate can produce detectable changes in tissue deformations, but whether or not these loading parameters could lead to extensive neurological deficits within a living specimen still requires further investigation. However, this study still maintains that the quasi-static loads applied can be influential with regard to analyzing microstructural damage evolution at the lower thresholds of traumatic brain injury. The clinical implications of minimal neuronal deformations that occur under these loading conditions must also be considered. Immediately following the physical trauma of a TBI, secondary biological pathways can develop to contribute to the overall injury mechanism, which can potentially initiate from abnormal changes within the neuron and glial cell density. For instance, excitotoxic mechanisms involving calcium influx can propagate throughout the neural tissue and ultimately lead to both apoptosis and axonal degeneration (Park, 2008). For clinical scenarios, these findings can offer further insight regarding the mechanisms of microstructural damage within brain tissue. With image analysis supplementing the mechanical data, a more comprehensive characterization of the internal behavior of porcine brain tissue also becomes possible. This could be beneficial for the development of constitutive models based on internal state variable theory and their implementation into a finite element environment.

REFERENCES

Abel, J.M., Gennarelli, T.A., Segawa, H. (1978). "Incidence and Severity of Cerebral Concussion in the Rhesus Monkey Following Sagittal Plane Angular Acceleration." *22nd Stapp Car Crash Conference Proceedings*, SAE 780886, 35-53.

Advani, S.H., Powell, W.R., Huston, J., Ojala, S.J. (1975). "Human Head Impact Response: Experimental Data and Analytical Simulations." *1975 International Conference on the Biomechanics of Serious Trauma*, 153-163.

Alberts, B., Johnson, A., Lewis, J., Martin, R., Roberts, K., Walter, P. "The Complex Morphological Specialization of Neurons Depends on the Cytoskeleton," in *Molecular Biology of the Cell*, *Fifth Edition*, 2008. Garland Science: New York, 1047-1050.

Arbogast, K.B., Margulies, S.S. (1998). "Material Characterization of the Brainstem from Oscillatory Shear Tests." *Journal of Biomechanics* **31**: 801-807.

Arbogast, K.B., Margulies. S.S. (1997). "Regional Differences in Mechanical Properties of the Porcine Central Nervous System." *41st Stapp Car Crash Conference Proceedings*, SAE 973336.

Cheng, S., Bilston, L.E. (2007). "Unconfined Compression of White Matter." *Journal of Biomechanics* **40**: 117-124.

Clarke, T.D., Gragg, C.D., Sprouffske, J.F., Trout, E.M. (1971). "Human Head Linear and Angular Accelerations During Impact." *15th Stapp Car Crash Conference Proceedings*, SAE 710857, 269-286.

Dickerson, J.W.T., Dobbing, J. (1966). "Prenatal and Postnatal Growth and Development of the Central Nervous System of the Pig." *Proceedings of the Royal Society of London, Series B.* **166**: 384-395.

Donnelly, B.R., Medige, J. (1997). "Shear Properties of Human Brain Tissue." *Journal of Biomechanical Engineering* **119**: 423-432.

Douglass, J.M., Nahum, A.M., Roberts, S.B. (1968). "Applications of Experimental Head Injury Research." *15th Stapp Car Crash Conference Proceedings*, SAE 680796, 317-337.

Ewing, C.L., Thomas, D.J., Beeler, G.W., Patrick, L.M., Gillis, D.B. (1968). "Dynamic Response of Head and Neck of Living Humans to Gravity Impact Acceleration." *12th Stapp Car Crash Conference Proceedings*, SAE 680792, 424-439.

Ewing, C.L., Thomas, D.J., Lustick, L., Muzzy, W.H. III, Willems, G., Majewski, P.L. (1976). "The Effect of Duration Rate of Onset and Peak Sled Acceleration on the Dynamic Response of the Human Head and Neck." *20th Stapp Car Crash Conference Proceedings*, SAE 760800, 3-41.

Franceschini, G., Bigoni, D., Regitnig, P., Holzapfel, G.A. (2006). "Brain Tissue Deforms Similarly to Filled Elastomers and Follows Consolidation Theory." *Journal of the Mechanics and Physics of Solids* **54**: 2592-2620.

Gennarelli, T., Thibault, L., Tomei, G., Wiser, R., Graham, D., Adams, J. (1987). "Directional Dependence of Axonal Brain Injury Due to Centroidal and Non-Centroidal Acceleration." *31st Stapp Car Crash Conference Proceedings*, SAE 872197, 49-53.

Gennarelli, T.A., Thibault, L.E., Adams, J.H., Graham, D.I., Thompson, C.J., Marcincin, R.P. (1982). "Diffuse Axonal Injury and Traumatic Coma in the Primate." *Annals of Neurology* **12**: 564-574.

Gennarelli, T.A., Thibault, L.E., Ommaya, A.K. (1972). "Pathophysiologic Responses to Rotational and Translational Accelerations of the Head." *16th Stapp Car Crash Conference Proceedings*, SAE 720970, 411-423.

Goldsmith, W. (2001). "The State of Head Injury Biomechanics: Past, Present, and Future: Part 1." *Critical Reviews in Biomedical Engineering* **29**(5-6): 441-600.

Got, C., Patel, A., Fayon, A., Tarriere, C., Walfisch, G. (1978). "Results of Experimental Head Impacts on Cadavers: The Various Data Obtained and their Relations to some Measured Physical Parameters." *22nd Stapp Car Crash Conference Proceedings*, SAE 780887, 55-99.

Gurdjian, E.S., Thomas, L.M., Hodgson, V.R. (1965). "Comparison of Species Response to Concussion." *9th Stapp Car Crash Conference Proceedings*, SAE 650971.

Gurdjian, E.S., Webster, J.E., Lissner, H.R. (1949). "Studies on Skull Fracture with Particular Reference to Engineering Factors." *American Journal of Surgery* **78**: 736-742.

Hirsch, A.E., Ommaya, A.K. (1970). "Protection from Brain Injury: The Relative Significance of Translational and Rotational Motions of the Head After Impact." *14th Stapp Car Crash Conference Proceedings*, SAE 700899, 144-151.

Hirsch, A.E., Ommaya, A.K., Mahone, R.H. "Tolerance of Subhuman Primate Brain to Cerebral Concussion," in *Impact Injury and Crash Protection*, 1970. Springfield, IL, 352-371.

Hodgson, V.R., Thomas, L.M. (1971). "Comparison of Head Acceleration Injury Indices in Cadaver Skull Fracture." *15th Stapp Car Crash Conference Proceedings*, SAE 710584, 190-206.

Hodgson, V.R., Thomas, L.M. (1972). "Effect of Long-Duration Impact on Head." *16th Stapp Car Crash Conference Proceedings*, SAE 710584, 335-338.

Hodgson, V.R., Thomas, L.M., Gurdjian, E.S., Fernando, O.U., Greenberg, S.W., Chason, J.L. (1969). "Advances in Understanding of Experimental Concussion Mechanisms." *13th Stapp Car Crash Conference Proceedings*, SAE 690796, 18-37.

Hodgson, V.R., Thomas, L.M., Khalil, T.B. (1983). "The Role of Impact Location in Reversible Cerebral Concussion." *27th Stapp Car Crash Conference Proceedings*, SAE 831618, 225-240.

Holbourn, A.H.S. (1945). "Mechanics of Brain Injuries." *British Medical Bulletin* **3**: 147-149.

Hrapko, M., van Dommelen, J.A.W., Peters, G.W.M., Wismans, J.S.H.M. (2008). "The Influence of Test Conditions on Characterization of the Mechanical Properties of Brain Tissue." *Journal of Biomechanical Engineering* **130**.

Kelley, B.J., Farkas, O., Lifshitz, J., Povlishock, J.T. (2006). "Traumatic Axonal Injury in the Perisomatic Domain Triggers Ultrarapid Secondary Axotomy and Wallerian Degeneration." *Experimental Neurology* **198**: 350-360.

Lind, N.M., Moustgaard, A., Jelsing, J., Vajta, G., Cumming, P., Hansen, A.K. (2007). "The Use of Pigs in Neuroscience: Modeling Brain Disorders." *Neuroscience and Biobehaviorial Reviews* **31**.

Lu, Y.B., Franze, K., Seifert, G., Steinhauser, C., Kirchhoff, F., Wolburg, H., Guck, J., Janmey, P., Wei, E., Kas, J., Reichenbach, A. (2006). "Viscoelastic Properties of Individual Glial Cells and Neurons in the CNS." *Proceedings of the National Academy of Sciences* **103**(47): 17759-17764.

McCracken, T.O., Kainer, R.A., Spurgeon, T.L. "The Swine," in *Spurgeon's Color Atlas of Large Animal Anatomy: The Essentials*, 1999. Lippincott Williams and Wilkins: Philadelphia.

McElhaney, J.H., Stalnaker, R.L., Roberts, V.L. "Biomechanical Aspects of Head Injury," in *Human Impact Response - Measurement and Simulation*, 1973. Plenum Press: New York, 85-111.

McElhaney, J.H., Stalnaker, R.L., Roberts, V.L., Snyder, R.G. (1971). "Door Crashworthiness Criteria." *15th Stapp Car Crash Conference Proceedings*, SAE 710864, 489-517.

Miller, K. (2000). "Biomechanics of Soft Tissues." *Medical Science Monitor* **6**(1): 158-167.

Miller, K., Chinzei, K. (2002). "Mechanical Properties of Brain Tissue in Tension." *Journal of Biomechanics* **35**: 482-490.

Miller, K. (2005). "Method of Testing Very Soft Biological Tissues in Compression." *Journal of Biomechanics* **38**: 153-158.

Miller, K., Taylor, Z., Wittek, A., "Mathematical Models of Brain Deformation Behavior for Computer-Integrated Neurosurgery," 2006. University of Western Australia.

Nahum, A.M., Smith, R.W. (1976). "An Experimental Model for Closed Head Impact Injury." *20th Stapp Car Crash Conference Proceedings*, SAE 760825, 785-814.

Nahum, A.M., Ward, C., Rasch, E., Adams, S., Schneider, D. (1980). "Experimental Studies of Side Impact to the Human Head." *24th Stapp Car Crash Conference Proceedings*, SAE 801301, 43-62.

Nusholtz, G.S., Lux, P., Kaiker, P., Janicki, M.A. (1984). "Head Impact Response - Skull Deformation and Angular Accelerations." *28th Stapp Car Crash Conference*, SAE 841657, 41-74.

Ommaya, A.K., Grubb, R.L., Naumann, R.A. (1971). "Coup and Contre-Coup Injury: Observations on the Mechanics of Visible Brain Injuries in the Rhesus Monkey." *Journal of Neurosurgery* **35**: 503-516.

Ommaya, A.K., Hirsch, A.E. (1966). "The Role of "Whiplash" in Cerebral Concussion." *10th Stapp Car Crash Conference Proceedings*, SAE 660804, 197-203.

Ommaya, A.K., Hirsch, A.E. (1971). "Tolerance of Cerebral Concussion from Head Impact and Whiplash in Primates." *Journal of Biomechanics* **4**: 13-22.

Ommaya, A.K., Rockoff, S.D., Baldwin, M. (1964). "Experimental Concussion: A First Report." *Journal of Neurosurgery* **21**: 249-267.

Ono, K., Kikuchi, A., Nakamura, M., Kobayashi, H., Nakamura, N. (1980). "Human Head Tolerance to Sagittal Impact Reliable Estimation Deduced from Experimental Head Injury Using Subhuman Primates and Human Cadaver Skulls." *24th Stapp Car Crash Conference Proceedings*, SAE 801303, 101-160.

Ono, K., Kikuchi, A., Nakamura, N. (1982). "Human Head Tolerance to Lateral Impact Deduced from Experimental Head Injuries Using Primates." *Proceedings from the 9th International Technical Donference on Experimental Safety Vehicles*, 361-371.

Ozkaya, N., Nordin, M. "Mechanical Properties of Biological Tissues," in *Fundamentals of Biomechanics: Equilibrium, Motion, and Deformation*, *Second Edition*, 1999. Springer: New York, 197-216.

Park, E., Bell, J.D., Baker, A.J. (2008). "Traumatic Brain Injury: Can the Consequences Be Stopped?" *Canadian Medical Association Journal* **178**(9): 1163-1170.

Prange, M.T., Margulies, S.S. (2002). "Regional, Directional, and Age-Dependent Properties of the Brain Undergoing Large Deformation." *Journal of Biomechanical Engineering* **124**: 244-252.

Prange, M.T., Meaney, D.F., Margulies, S.S. (1998). "Directional Properties of Gray and White Brain Tissue Undergoing Large Deformation." *Advances in Bioengineering* **39**: 151-152.

Raven, P.H., Johnson, G.B. "Neuron Organization," in *Biology*, *Sixth Edition*, 2002. McGraw-Hill: New York, 1074-1075.

Shatsky, S.A., Alter, W.A., Evans, D.E., Armbrustmacher, V.W., Clark, G., Earle, K.M. (1974). "Traumatic Distortions of the Primate Head and Chest: Correlation of Biomechanical Radiological and Pathological Data." *18th Stapp Car Crash Conference Proceedings*, SAE 741186, 351-381.

Stalnaker, R.L., Roberts, V.L., McElhaney, J.H. (1973). "Side Impact Tolerance to Blunt Trauma." *17th Stapp Car Crash Conference Proceedings*, SAE 730979, 377-408.

Shuck, L., Advani, S. (1972). "Rheological Response of Human Brain Tissue in Shear." *Journal of Basic Engineering*: 905-911.

Stapp, J.P. "Biodynamics of Deceleration Impact and Blast," in *Aerospace Medicine*, 1971. Williams and Wilkins: Baltimore, 118-166.

Stapp, J.P. "Impact Injury of the Head and Spine," in *Historical Review of Impact Injury and Protection Research*, 1983. CC Thomas: Springfield, IL, 5-40.

Tamura, A., Hayashi, S., Watanabe, I., Nagayama, K., Matsumoto, T. (2007). "Mechanical Characterization of Brain Tissue in High-Rate Compression." *Journal of Biomechanical Science and Engineering* **2**(3): 115-126.

Thibault, L.E., Gennarelli, T.A. (1990). "Brain Injury: An Analysis of Neural and Neurovascular Trauma in the Non-Human Primate." *Association for the Advancement of Automotive Medicine Conference Proceedings*, SAE 1990=12-0020, 337-351.

Thibault, K.L., Margulies, S.S. (1998). "Age-Dependent Material Properties of the Porcine Cerebrum: Effect on Pediatric Inertial Head Injury Criteria." *Journal of Biomechanics* **31**: 1119-1126.

Widmaier, E.P., Raff, H., Strang, K.T. "Structure of the Nervous System," in *Vander's Human Physiology: The Mechanisms of Body Function*, *Tenth edition*, 2006. McGraw-Hill: Columbus, OH, 191-205, 332-334.